LUND UNIVERSITY

Surface modification of III-V nanostructures studied by low-temperature scanning tunneling microscopy

Liu, Yi

2022

Document Version:
Publisher's PDF, also known as Version of record

Link to publication

Citation for published version (APA):
Liu, Y. (2022). *Surface modification of III-V nanostructures studied by low-temperature scanning tunneling microscopy*. Media-Tryck, Lund University, Sweden.

Total number of authors:
1

General rights
Unless other specific re-use rights are stated the following general rights apply:
Copyright and moral rights for the publications made accessible in the public portal are retained by the authors and/or other copyright owners and it is a condition of accessing publications that users recognise and abide by the legal requirements associated with these rights.
• Users may download and print one copy of any publication from the public portal for the purpose of private study or research.
• You may not further distribute the material or use it for any profit-making activity or commercial gain
• You may freely distribute the URL identifying the publication in the public portal

Read more about Creative commons licenses: https://creativecommons.org/licenses/

Take down policy
If you believe that this document breaches copyright please contact us providing details, and we will remove access to the work immediately and investigate your claim.

LUND UNIVERSITY

PO Box 117
221 00 Lund
+46 46-222 00 00

Surface modification of III-V nanostructures studied by low-temperature scanning tunneling microscopy

YI LIU
DEPARTMENT OF PHYSICS | FACULTY OF SCIENCE | LUND UNIVERSITY

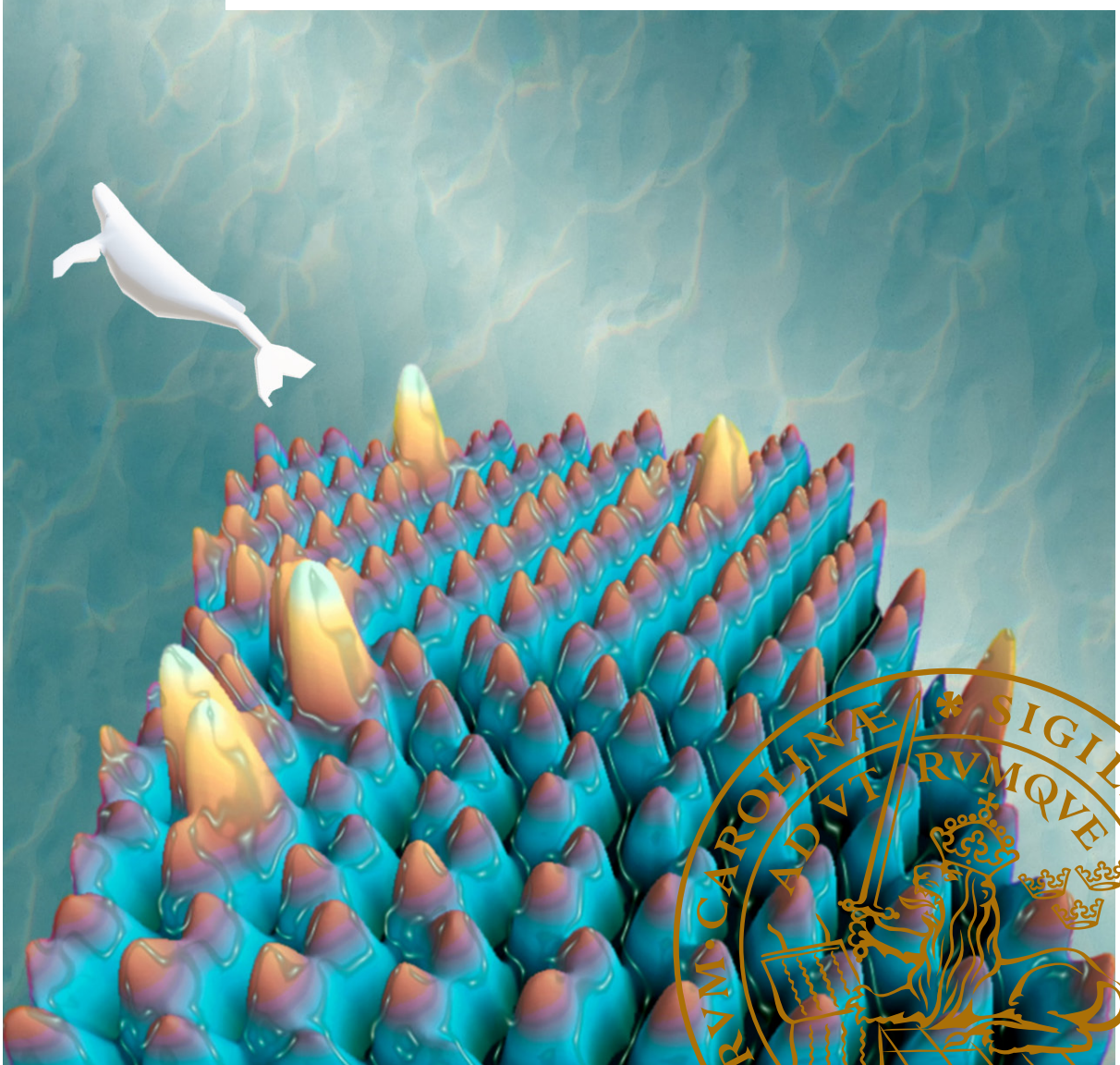

Printed by Media-Tryck, Lund 2022 NORDIC SWAN ECOLABEL 3041 0903

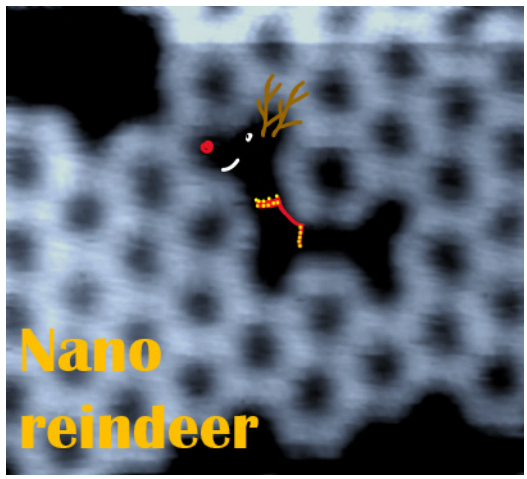

ISBN 978-91-8039-291-4

Division of Synchrotron Radiation Research
Department of Physics
Faculty of Science
Lund University

Surface modification of III-V nanostructures studied by low-temperature scanning tunneling microscopy

Yi Liu

LUND
UNIVERSITY

DOCTORAL DISSERTATION

by due permission of the Faculty of Science, Lund University, Sweden.
To be defended at the Rydberg lecture hall at the Department of Physics
17th June, 2022, at 13:15.

Faculty opponent
Prof. Rachel S. Goldman
University of Michigan, USA

Organization	Document name
LUND UNIVERSITY Division of Synchrotron Radiation Research Department of Physics, Box 118, 22100 Lund	DOCTORAL THESIS **Date of issue** 20 May 2022
Author: **Yi Liu**	Sponsoring organization

Title and subtitle

Surface modification of III-V nanostructures studied by low-temperature scanning tunneling microscopy

Abstract

In the past decade, driven by the demand for materials with high performance for next-generation semiconductor devices (e.g., for quantum computing), the exploration of III-V semiconductor materials and the design of improved devices based on these materials has extended to the nanometer scale, with several highlights in the studies of quantum wells, quantum dots, and nanowires (NW) in recent years. On the path of seeking smaller scale devices, the lateral scale is usually limited by the spatial resolution of the lithographic processes. Now, the challenge lies in the combination of semiconductor nanoscale structure with the desired electronic properties. Scaling down material synthesis to crystalline structures of only few atoms in size and precisely positioned in device configuration has not been realized so far. Moreover, the compatibility for large-scale industrial device processing is also challenging.

In this dissertation, I present the surface characterization and studies of the modification of nanostructures on III-V semiconductor surfaces, with the techniques of low temperature scanning tunneling microscopy/spectroscopy (LT-STM/S) and X-ray photoelectron spectroscopy (XPS). Two main topics are Bi incorporation in GaAs (and InAs) surfaces and self-driven formation of nanostructures with atomic-scale precision. Different zinc blende and wurtzite crystal planes have been investigated, including the {11-20}- type facet which for GaAs and InAs uniquely exists on the side walls of NWs and nanoplatelets. The utilization of the tailored facets of NWs as templates for Bi-induced nanostructure formation has been explored as well.

Bi-introduced low-dimensional nanostructures and exotic electronic states in III-V semiconductor systems have been investigated. The covalent bonds of Bi atoms in the self-formed Bi nanostructures on III-V substrates can vary depending on the substrate template and preparation condition, such as the Ga-Bi bonds in the 1D chain and 2D island nanostructures on Wz{11-20}-type facets on GaAs NWs. The possibility of tuning the self-formed III-V:Bi nanostructures in a more controllable way has been explored in this thesis. A significant high coverage of Bi on III-V semiconductor surface has been achieved. The observed variable bandgap and Bi-induced surface states are promising for applications in surface bandgap engineering and quantum technology components.

Key words

STM, XPS, semiconductor surface, III-V, nanostructure modification, nanowires, self-selective formation, atomic scale imaging, Bi incorporation

Classification system and/or index terms (if any)		
Supplementary bibliographical information		**Language** English
ISSN and key title		**ISBN 978-91-8039-291-4** **978-91-8039-292-1**
Recipient's notes	**Number of pages** 108	Price
	Security classification	

I, the undersigned, being the copyright owner of the abstract of the above-mentioned dissertation, hereby grant to all reference sources permission to publish and disseminate the abstract of the above-mentioned dissertation.

Signature 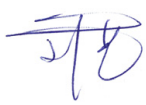 Date 2022-05-04

Surface modification of III-V nanostructures studied by low-temperature scanning tunneling microscopy

Yi Liu

LUND
UNIVERSITY

Front cover: **From gigantic to tiny.**
3D image of a GaAs nanowire surface with incorporated Bi atoms. Each protrusion presents an As atom, while the higher protrusions in yellow color indicate the incorporated Bi atoms.

Back cover: **Nano Reindeer.**
The unclosed honeycomb structure of Bi on a GaAs substrate. Each honeycomb structure consists of six Bi atoms.

Copyright Page i-x, 1-88, front and back covers: © Yi Liu
Paper 1 © by the authors (published by Springer Nature under a CC BY license)
Paper 2 © by the authors (manuscript unpublished).
Paper 3 © by the authors (manuscript unpublished).
Paper 4 © by the authors (published by AIP Publishing under a CC BY license)

Division of Synchrotron Radiation Research
Department of Physics, Faculty of Science
Lund University
SE-221 00, Lund
Sweden

ISBN 978-91-8039-291-4 (print)
978-91-8039-292-1 (electronic)

Printed in Sweden by Media-Tryck, Lund University
Lund 2022

Media-Tryck is a Nordic Swan Ecolabel certified provider of printed material. Read more about our environmental work at www.mediatryck.lu.se
MADE IN SWEDEN

Time is "a number of change with respect to the before and after"

- Aristotle

Acknowledgements

When I write this paragraph, it is the last weekend in April - the Valborg day in Lund. Now this thesis is close to be finished, and I feel a little bit released and finally a little bit proud of myself.

It has been a rather memorable period during my Ph.D studies. I've met a lot of good and amazing people; I have been involved in a lot of interesting work; I have travelled to many places for beamtimes and conferences (although the pandemic has put things on hold for a long time). During my Ph.D studies, there were some ups and downs, well, sometimes quite unexpected! But ultimately, I could (and should) overcome these obstacles and welcome the next change.

I couldn't have gotten this far without the help of many people. First of all, I would thank my supervisor Rainer for his tremendous help and support. You has always been kind, patient and thoughtful, and I have always been impressed with your ability to communicate, to do multiple tasks at the same time, to notice so many details, and your ability to write! Thank you for allowing me a lot of freedom to explore my own ideas. You showed me what a decent, good and super qualified supervisor should look like. I thank my supervisor Anders for being so friendly and witty, and you always support us with your solid and wide-ranging knowledge. Even the discussion with my supervisors has been always nice, I learned a lot from your open-minded and optimistic thinking, especially when dealing with the unexpected little frustrations. No matter how difficult the situation seems, we can always find solutions in the end. Otherwise, we accept it! For example, in Anders's way, "hmm, what can you do?".

I am grateful to the people who helped me a lot in the division. Thanks Anne and Patrik for helping with paperwork and administration. Patrick's loud laughter in the hallway will be a fond memory, along with the often-occupied corner of the dining room table - "Det är min plats!". Thank you Edvin for always bringing the cakes, you are the most humorous professor I have ever met!

I thank all my collaborators for the excellent work we have done. Especially thanks Chris for welcoming me to your lab and conducting the experiments, and many thanks to the UCSB group for your help. Sincere thanks to Sebastian, a reliable man who grows exquisite NWs with his magical hands. Thank you Olle and Chin Shen in

Uppsala University, it is a nice experience working with you. I am looking forward to more great results!

A big thank you to my dear colleagues, it is so delightful to have you around. Sandra has always been a nice beamtime teammate, and thanks Rohit for being a nice dining-mate. And I will remember the nice conversations with many of you, Ahmed and Alfred (thanks for the Chinese New Year dinner!), Emma, Lingjia, Virginia, Susanna ….Thank you Estephania for always being there with your kind support and your happy laughter.

Thanks to my officemate Giulio for your encouragement, I don't think I could have finished this thesis without your kind and warm daily reminders.

It is great to have Lukas and we can talk about our gardening hobby! I am amazed how many “gröna fingrar” you have. Thank you Lucas for watering my plants while I was away, even if it was for a few weeks! You are such a nice neighbor.

I thank Zhaojun, Huaiyu, Yuhe, Foqia, Smita, Fatemeh and Yen-Po, for all the activities we did together, big and small. I am glad to have you all in my memories of my Ph.D life.

I am also grateful to those of you who have graduated and are pursuing your careers, Andrea, Sofie, Chuchu, Lert….. You have been an important part of this pleasant atmosphere.

I would like to thank my wonderful parents for your unconditional love. I will thank and hug Nik for your understanding and precious love. Thank you, Nik's family, for your care and support.

同时也感谢我身在国内的家人和朋友们，以及现在身处世界各地的朋友们。是你们拓展了我视野的维度，让我生活中的充满了小确幸，小感动。

海内存知己，天涯若比邻。愿世界和平，美好。

愿我们都能一如既往地热爱生活，探索新的惊喜！

Now I have again learned the lesson that the future is unpredictable, both in a hopeful way and sometimes in a chaotic way. Just like Aristotle’s understanding of time, there is change and there is time.

So, let’s embrace the future, and be a part of the change!

Contents

Abstract

In the past decade, driven by the demand for materials with high performance for next-generation semiconductor devices (e.g., for quantum computing), the exploration of III-V semiconductor materials and the design of improved devices based on these materials has extended to the nanometer scale, with several highlights in the studies of quantum wells, quantum dots, and nanowires (NWs) in recent years. On the path of seeking smaller scale devices, the lateral scale is usually limited by the spatial resolution of the lithographic processes. Now, the challenge lies in the combination of semiconductor nanoscale structure with the desired electronic properties. Scaling down material synthesis to crystalline structures of only few atoms in size and precisely positioned in device configuration has not been realized so far. Moreover, the compatibility for large-scale industrial device processing is also challenging.

In this dissertation, I present the surface characterization and studies of the modification of nanostructures on III-V semiconductor surfaces, with the techniques of low temperature scanning tunneling microscopy/spectroscopy (LT-STM/S) and X-ray photoelectron spectroscopy (XPS). Two main topics are Bi incorporation in GaAs (and InAs) surfaces and self-driven formation of nanostructures with atomic-scale precision. Different zinc blende and wurtzite crystal planes have been investigated, including the $\{11\bar{2}0\}$- type facet which for GaAs and InAs uniquely exists on the side walls of NWs and nanoplatelets. The utilization of the tailored facets of NWs as templates for Bi-induced nanostructure formation has been explored as well.

Bi-introduced low-dimensional nanostructures and exotic electronic states in III-V semiconductor systems have been investigated. The covalent bonds of Bi atoms in the self-formed Bi nanostructures on III-V substrates can vary depending on the substrate template and preparation condition, such as the Ga-Bi bonds in the 1D chain and 2D island nanostructures on Wz$\{11\bar{2}0\}$-type facets on GaAs NWs. The possibility of tuning the self-formed III-V:Bi nanostructures in a more controllable way has been explored in this thesis. A significant high coverage of Bi on III-V semiconductor surface has been achieved. The observed variable bandgap and Bi-induced surface states are promising for applications in surface bandgap engineering and quantum technology components.

Popular science

What were you thinking when you were playing with toy bricks in your childhood? Can I build something giant and dedicated, or something that is equipped with a special function, like a highway road or a mini bed for a cat? Nowadays, children have smaller bricks to represent their imagination, such as LEGO. These plastic bricks are designed to be connected with another piece by knobs on the surface, however, the way of combinations is infinite. We can easily replace the component, such as a lamp on the London bridge, or a helmet of Skywalker in Star Wars.

Well, people enjoy a lot when building up their world with small bricks and they can design it in their own way. But how about the real smallest "bricks" of matter in the real world - atoms?

In 2013, IBM published the world's smallest movie, called "A Boy and His Atom"[1], made on the atomic scale using scanning tunneling microscopy (STM) technology. The "bricks" in this movie are carbon monoxide molecules, which have the diameter of around 0.3 nm (1 nm = 0.000 001 mm, 0.3 nm is about 1/100 000 of the diameter of a human hair). The carbon monoxide molecules were manipulated by an STM probe and moved to the desired locations before an image was recorded. Would you wonder what the meaning of this movie is, except for entertaining purpose? Well, to me, the exciting message out of this video is that it shows how matter can be modified down to atomic scale, even possibly designed as people wish. How can we benefit from it? A souvenir with your name "written" by molecule "ink"? Sounds cool, but we can do much more than that.

In the past few decades, we can clearly notice the change in the sizes of electronic products. Telephones and computers are getting significantly smaller but on the same time much more powerful. A smartphone nowadays has a much more powerful processor and is almost a thousand times faster than a personal computer in the mid-'80s, where the development of microchips (or processors) - the basic building blocks of modern electronics - plays an important part.

A microchip contains many transistors which are semiconductor devices used to amplify or switch electrical signals and power. Nowadays, the complexity within an integrated circuit that has millions or even billions of transistors is incredibly high. The Moore's law, which describes that the number of transistors on microchips

doubles every two years, still roughly applies to the development of transistor techniques so far. Nowadays the microchips are manufactured by semiconductor industry in a top-down approach based on complex and very expensive lithography and etching steps. Recently in 2021, IBM announced the creation of the first 2 nm computer chip, which is similar to the size of human DNA. On the market, semiconductor industry offers chips of the so-called "5 nm node", where the highest precision of commercially available features is in the range of only several nanometers. Nevertheless, when approaching the size of atoms (several Å, 1 Å = 0.1 nm), there comes the fundamental physical limitation. On the other hand, scaling down material synthesis to semiconductor structures of only a few atoms in size is crucial for further electronic development, especially for new applications, such as quantum computing.

III-V semiconductors, such as gallium arsenide (GaAs) and indium arsenide (InAs), have superior properties than Si in many aspects, such as outstanding charge carrier mobility and direct bandgap. For semiconductor structures at nano scale (below called nanostructures), the high surface-to-bulk ratio makes their surface very important in achieving high-performance devices, such as the surface quality and composition.

A large part of this thesis focuses on the characterization and on studying the modification of the III-V semiconductor nanostructure surface with atomic-scale precision, and the mechanism of the self-formation process on the surface. The self-formation implies that the surface nanostructures can be constructed automatically under certain conditions. Basically, we are trying to create suitable conditions and "guide" the atoms to the desired locations on the surface. The self-driven formation is a big advantage when being standardized into industry manufacturing processes. There are three important elements in my research: **new element, templates,** and **chemical bonds**.

Adding a **new element** species is a very common approach when we want to improve the material's properties, such as the carrier mobility, or alter the bandgap. III-V semiconductors have a large flexibility in combining different materials, such as bismuth (Bi). For high Bi content, III-V:Bi material is predicted to form topological insulators. Thus, many conditions of depositing Bi atoms onto the surfaces of binary III–V compounds have been tried in my research.

The **templates** we use are III-V semiconductor crystalline plane surfaces. The atoms in bulk crystals are in a well-ordered fashion, so are the atoms on the exposed crystal surface. Depending on different crystalline structures and crystal plane orientation, several exposed surfaces can be obtained, such as Zinc blende (Zb) {110}- and {111}-type facets. Moreover, nanowire/nanoplatelet (crystalline rod or flat piece with diameter/thickness of around a few tens to hundreds of nanometers) heterostructures are utilized as templates as well. It is found out that the different

exposed crystal planes have big impact on the resulting nanostructures. For example, local 1D GaBi chains and 2D GaBi islands have been observed after Bi incorporation on the special wurzite (Wz) $\{11\bar{2}0\}$ facet of GaAs NWs. These small GaBi structures exist, including only a few tens of atoms, even though GaBi is an unstable material in bulk form! The secret why GaBi can be formed in such an ordered way is discovered to be that Bi atoms have preferred first incorporation sites (terrace edges facing $[000\bar{1}]$ directions), followed by the fact that they are relatively mobile along the $[000\bar{1}]$ orientation. On another surface which was studied extensively in my work, GaAs (111)B, which has an arsenic (As)-terminated surface top layer, a large-scale 2D Bi honeycomb structure has been imaged, and a decrease of surface bandgap has been observed.

To characterize the surface topography and electronic properties, low temperature scanning tunneling microscopy/spectroscopy (LT-STM/S) has been used to a large extent in this thesis. STM is a technique that can scan probe the crystalline surface down to sub-atomic resolution, while with STS, the local density of states (LDOS) is measured, and the width of the bandgap can therefore be obtained, for example.

We often use the term "chemical reaction" when describing invisible and special connections happening between two objects. Very true! Here, **chemical bonds** would be formed between two atoms if strong chemical reactions happen between them. Strong chemical bonds, such as covalent bonds, are very crucial for the stability of the material, and they largely influence the chemical properties. Chemical bonds can be characterized by a surface-sensitive technique called X-ray photoelectron spectroscopy (XPS), which captures the emitted photoelectron from the core level electrons of atoms illuminated by X-rays. For example, As-Bi bonds have been discovered in the 2D honeycomb structure on GaAs(111)B, revealing that Bi atoms are directly bonded to As atoms below.

To conclude, the self-formation process of Bi atoms on III-V surfaces is a result of the interplay between the atomic morphology and the surface energy. In this thesis, I aim to present the atomic world and to show you what is happening when the III-V semiconductor nanostructures are being modified down to atomic level, and how eventually these fancy nanostructures are built up with the atom bricks.

Preface & List of papers

In this thesis the following papers are included.

Paper I

Self-selective formation of ordered 1D and 2D GaBi structures on wurtzite GaAs nanowire surfaces

Yi Liu, Johan V. Knutsson, Nathaniel Wilson, Elliot Young, Sebastian Lehmann, Kimberly A. Dick, Chris J. Palmstrøm, Anders Mikkelsen, and Rainer Timm

Nature Communications, **12**(1): p. 5990. (2021)

In this paper we present the study on self-selective growth of 1D and 2D GaBi nanostructures using nanowire crystal phase heterostructures as templates, which allows versatile design with atomic-scale precision. We compare the Bi incorporation process on wurtzite and zinc blende facets of GaAs nanowires and establish models to explain them.

I took part in the STM experiments and data analyzing. I was the main responsible for writing the paper.

Paper II

A 2D bismuth-induced honeycomb surface structure on GaAs(111)

Yi Liu, Sandra Bender, Renan P. Maciel, Austin Irish, Linnéa Björk, Chin Shen Ong, Olle Eriksson, Anders Mikkelsen, and Rainer Timm

Submitted to ACS nano (2022)

In this paper we present the study of Bi incorporation on a GaAs(111)B substrate. A large-scale 2D bismuth-induced honeycomb structure is observed. The chemical bonding configurations and surface electronic properties are investigated.

I took part in the planning and conducting both STM and XPS experiments. I was the main responsible for analysing the data and for writing the paper.

Paper III

Bismuth surface alloying on 2D InAs nanoplatelets.

Sandra Benter, Yi Liu, Lassi Linnala, Chin Shen Ong, Dong Pan, Austin Irish, Yen-Po Liu, Renan Da Paixao Maciel, Jianhua Zhao, Hongqi Xu, Olle Eriksson, Rainer Timm, and Anders Mikkelsen

In manuscript

In this paper we investigated the incorporation mechanism of Bi adatoms into an InAs nanosheet with WZ{11$\bar{2}$0} lattice in comparison to a bulk ZB{110} crystal. A dependency for the formation of As-Bi and In-Bi bonds on sample temperature and crystal facet was found.

I took part in the XPS experiments and discussions for data analysis.

Paper IV

Low Temperature Scanning Tunneling Microscopy and Spectroscopy on Laterally Grown $In_xGa_{1-x}As$ Nanowire Devices

Yen-Po Liu, Lasse Södergren, S. Fatemeh Mousavi, Yi Liu, Fredrik Lindelöw, Erik Lind, Rainer Timm, and Anders Mikkelsen

Applied Physics Letters, 117(16): p. 163101. (2020)

In this paper we present the study of the geometric and electronic surface structures of $In_xGa_{1-x}As$ nanowires and contacts, which were grown directly in a planar configuration, using LT-STM/S.

I took part in the STM measurement on the lateral nanowires, as well as the discussions on manuscript writing.

The following papers are not included in this thesis

Paper V

Nanometric moiré stripes in topological insulator Bi_2Se_3 thin films and nanobelts

M. Salvato, M. De Crescenzi, M. Scagliotti, P. Castrucci, S. Boninelli, G.M. Caruso, Y. Liu, A. Mikkelsen, R. Timm, S. Nahas, A. M. Black-Schaffer, G. Kunakova, J. Andzane, D. Erts, T. Bauch and F. Lombardi

Submitted (2022)

In this paper we investigate the origin of the 1D moiré stripes on the surface of Bi_2Se_3 topological insulators thin films and nanobelts. The strongly changed density of surface states between the top and valley of the stripes are also studied.

I took part in the STM measurement of the moiré stripes on the surface of Bi2Se3 nanobelts, as well as the discussions on manuscript writing.

Paper VI

Tuning oxygen vacancies and resistive switching properties in ultra-thin HfO_2 RRAM via TiN bottom electrode and interface engineering

Zhihua Yong, Karl-Magnus Persson, Mamidala Saketh Ram, Giulio D'Acunto, Yi Liu, Sandra Benter, Jisheng Pan, Zheshen Li, Mattias Borg, Anders Mikkelsen, Lars-Erik Wernersson, Rainer Timm

Applied Surface Science, p. 149386. (2021)

In this paper we present the study of the concentration of oxygen vacancies in HfO_x layer in two types of resistive random access memory (RRAM) stacks, where the TiN bottom metal electrode were fabricated by physical vapor deposition (PVD) and atomic layer deposition (ALD), respectively.

I took part in the XPS measurement for the devices, as well as the discussions on manuscript writing.

Paper VII

Strain mapping inside an individual processed vertical nanowire transistor using scanning X-ray nanodiffraction

Dmitry Dzhigaev, Johannes Svensson, Abinaya Krishnaraja, Zhongyunshen Zhu, Zhe Ren, Yi Liu, Sebastian Kalbfleisch, Alexander Björling, Filip Lenrick, Zoltan Imre Balogh, Susanna Hammarberg, Jesper Wallentin, Rainer Timm, Lars-Erik Wernersson and Anders Mikkelsen

Nanoscale 12(27): p. 14487-14493. (2020)

In this paper we investigate the strain within nanowires by characterizing the crystal structure with synchrotron-based X-ray nanodiffraction technique.

I took part in the X-ray nanodiffraction measurement, as well as the discussions on manuscript writing.

1 Introduction

Semiconductor materials, that lay the foundation for electronic devices in modern society, play a vital role for the modern digitalized world. Many different semiconductor materials have seen major development in the past few decades, to allow more functionalities. Compared to the conventional semiconductor material Si, III–V semiconductors (*e.g.,* InAs and GaAs) show superior electronic properties, such as direct, tunable bandgaps and a higher charge carrier mobility. III–V materials are therefore optimal for high-performance electronics[2-7], photonics[8-11], and energy harvesting [11-13].

Conventionally, highly integrated and sophisticated chips are produced via a top-down approach based on complex and very expensive lithography and etching procedures. Current cutting-edge techniques offer a precision for semiconductor chips down to a few nanometer. Nevertheless, while the precision is approaching the size of single atoms (several Å, 1 Å = 0.1 nm), the room for improving the precision by complex processing steps is rather limited due to the spatial resolution of the lithographic processes.

Since semiconductor nanostructures are crucial for applications such as quantum computing which demands atomic scale precision[14], new breakthroughs are urgently needed. Generally, approaches either rely on scaling down material synthesis to crystalline structures of only a few atoms in size, or synthesizing new materials in a bottom-up approach with novel electronic properties, or both. In summary, the primary solution lies in modifying and designing semiconductor nanostructures at atomic scale.

For nanostructures, the surfaces play a significant role in defining their function due to the large surface-to-bulk ratio, and electronic surface effects and the enhanced interaction with the environment can determine the (opto)electronic behavior of the complete nanostructure devices. This is certainly true for nanowires (NW, crystalline rods with a diameter between typically 20 and 200 nm and a length of up to a few µm) which due to its geometry offer new avenues for surface-related growth phenomena compared to a flat 2D substrate. What is more, via so-called crystal phase engineering[15], NWs grown using a metal seed particle via Metal Organic Vapor Phase Epitaxy (MOVPE) can have tailored crystal structures with atomically sharp

transitions between cubic zincblende (Zb) and hexagonal wurtzite (Wz) segments, and tuneable length. Unique side wall facets are also observed, for example, the Wz{11$\bar{2}$0} facet, which exists as a stable phase for GaAs and InAs only in nanostructures[16]. Hence, the surface of NWs provides an ideal platform for controlling and designing the electronic landscape of semiconductor devices with novel functionality[17,18].

Previous STM studies have successfully resolved the atomic structure of various of these facets and the Wz/Zb interface on GaAs[19,20] and other III–V NWs[21-23]. NWs have demonstrated significant promise for application in (opto)electronics and now quantum computing[24-30]. In general, heterostructures with significant bandgap variation are needed for creating the relevant NW functionality, and it is important to achieve high-quality interfaces for realizing devices[30-33]. However, formation of precisely controlled material heterostructures inside nanostructures and on top of their surfaces remains a significant challenge.

Among the various possible material combinations of the III–V semiconductor family, alloys with a high bismuth content have gained attention, mainly due to the large spin-orbit coupling and band bowing of Bi-containing semiconductor alloys[34-36]. Particularly, the III-As:Bi material is promising for novel device applications within optoelectronics, quantum information technology, and bandgap engineering[35,37], due to its increased exciton recombination times and expected non-trivial topological behavior [38]. For high Bi content, band inversion with a sufficiently large bandgap for room temperature stability has been predicted [39,40].

So far, III–As alloying with a high Bi content (>20% of the group-V atoms) could not be realized[38,41], which is due to the high lattice mismatch between III-As and III-Bi materials. Thus, another alternative is adopted – depositing Bi on as -grown III-As crystal planes and letting Bi incorporate into the III-As surface. For now, Bi deposition has been studied on several III-As surfaces, such as GaAs(110)[42], (001), or {111}, and Bi-terminated surface reconstructions were observed. However, previous studies have not found any significant ordered incorporation in the atomic lattice[43]. With an unbroken substrate symmetry, III-As wafers with promising surface orientation have advantages on a desired large scale industrial manufacturing as well.

My work has been dedicated to exploring new possibilities in modifying and characterizing nanostructures at the atomic scale on surfaces of GaAs and InAs in different orientation, including both planar substrate and NW side facets, while also keeping an interest on studying single InGaAs NW devices for more practical purpose. To this end, I have studied Bi incorporation mechanisms on GaAs and InAs surfaces with atomic-scale precision and the electronic properties of novel Bi-induced III-As nanostructures. One of the mechanisms can be concluded to be a self-organized process including site-selected formation on the surface. Identifying the

chemical composition of the formed nanostructures (III-Bi, V-Bi, or metallic Bi-Bi) is another major topic in my research.

Scanning tunneling microscopy/spectroscopy (STM/S) and x-ray photoelectron spectroscopy (XPS) are the main two techniques utilized in my research, because of their highly surface sensitive properties. Consequently, in coherence with the surface sensitive theme, all techniques were operated in UHV atmosphere. The tomography and surface electronic properties are characterised with STM/S at the atomic scale, and the elements and chemical compounds of III-As:Bi nanostructures were studied with XPS.

This dissertation is built up as follows.

Chapter 2 gives a general introduction to III-V semiconductors and nanowires, with a focus on their surface planes from the perspective of surface science. The growth, crystal structure engineering, and exposed side wall facets of NWs are introduced.

Chapter 3 provides the background needed to understand scanning tunneling microscopy and how to interpretate STM images of semiconductor surfaces, including a discussion of tip-induced band bending. Atomic scale images of NWs of III–V materials are presented.

Chapter 4 gives an introduction to scanning tunneling spectroscopy (STS), which was used together with STM in several papers included in this dissertation. Different modes of operation as well as data treatment and interpretation are discussed.

Chapter 5 introduces the surface sensitive technique X-ray photoelectron spectroscopy (XPS), which is a complementary technique to STM/S, as it provides information about the chemical composition of a surface. Some XPS examples from III-V:Bi surfaces are presented.

Chapter 6 summarizes Bi-incorporation in III-As surfaces, with a highlight on both structural and electronic alternations.

Finally, in **Chapter 7**, I conclude my work and describe some possible routes for future studies.

The second part of the dissertation is constituted by papers **I** to **IV**.

2 III-V Semiconductor Nanowires

III-V semiconductors lay the foundation of my research in this thesis, while I mostly focus on the atomic and electronic structure of surfaces.
In this chapter the fundamental crystal and surface structures of III-V semiconductors will be presented, later the discussion goes all the way from bulk scale to nanoscale, including unique structures and topographies that are only stable at the nanoscale, with the example of nanowires. The concepts such as tailored phase growth will be introduced as well. I will quickly mention the lateral nanowire device that is used in our study. In the end, semiconducting properties, such as the concept of the band gap, will be introduced, so that readers can understand better about STM imaging on semiconductors later in Chapter 3.

2.1 Bulk crystal structures

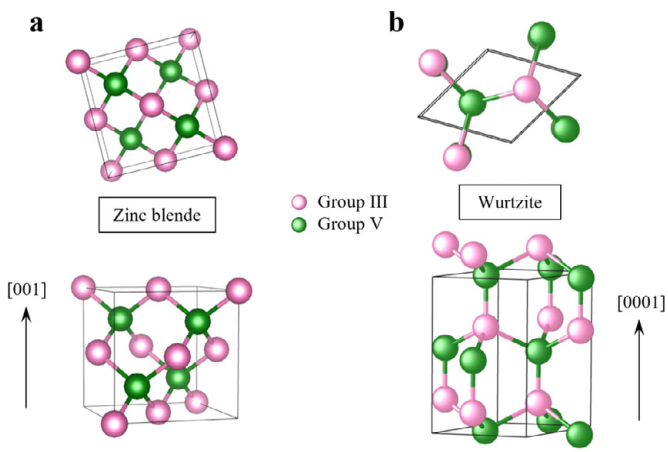

Figure 2.1 The 3D atomic model of zinc blende structure (a) and Wurtzite structure (b). The top models are from (001) and (0001) top view, respectively, and the bottom ones are from side view. The unit cells are indicated with the enclosed shape in black lines.

Among the big family of III-V semiconductors, for example InAs, GaAs, InP, etc., GaAs and InAs are the focus of my research study. The most common crystal structure for III-V materials in bulk is the cubic zinc blende (Zb) crystal structure, which is shown in Fig. 2.1a with the top and side view. The Zb structure can be considered as a basic face centred cubic (fcc) sublattice of one component, while the other component follows the same structure but with a shift of [$^1/_4$ $^1/_4$ $^1/_4$] base vector compared to the original unit. The Wurtzite (Wz) structure, as shown in Fig. 2.1b, on the other hand, can be seen as two interpenetrated hexagonal lattices. If viewing along the [111] direction (corresponding to the [0001] direction in the hexagonal lattice coordinates), Wz and Zb structures are morphologically similar and differ only in the stacking sequence and slightly in interatomic distances, which can refer to Fig. 2.6 in section 2.3.1. All atomic 3D models in this thesis are drawn with VESTA software[44].

Most III-V materials can only be stable in Zb structure in bulk form, while only some, such as GaN, crystallize in the Wz structure, because of their more ionic character of the atomic bonds. For GaAs and InAs, the Wz structure can only be formed in nanoscale structures under certain growth conditions[45,46], such as nanowires (NW).

The Zb structure, which is the structure of commercially available GaAs and InAs wafers, has also been investigated to a large extent in my study. Here, a main focus is on the (111) surface. For example, in Paper **II**, a large scale 2D bismuth-induced honeycomb surface structure is realized on a GaAs(111)B surface. Here, (111) indicates the atomic plane orientation, more specifically, atomic planes are defined by their Miller indices (hkl). B indicates the surface is terminated with As atoms. Vice versa, when the surface is terminated with Ga atoms, the plane is called GaAs(111)A.

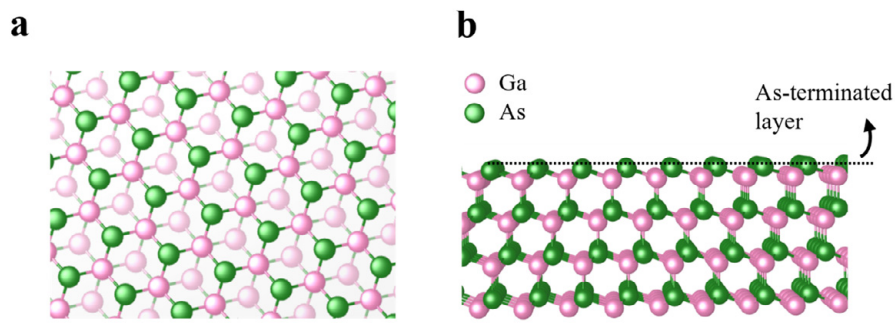

Figure 2.2 Top view (a) and side view (b) of the atomic model of GaAs(111)B surface. (a) Only the topmost 2 Ga-As bilayers are shown, the half transparent layer is the 2nd topmost layer. Each bilayer contains a single layer of Ga and As atoms. (b) shows that the surface is terminated with As atoms.

This type of surfaces, where the surface is either As-rich or Ga-rich, are polar surfaces. The top and side view of GaAs(111)B atomic structure is shown in Fig. 2.2a and b, respectively. In the side view, we can clearly see that As atoms are at the outmost layer while Ga atoms are more towards the bulk. More importantly, the As atoms have dangling bonds (as long as the surface is not reconstructed), while all bonds of the Ga atoms are saturated. On the nonpolar cleavage plane (110) is the energetically stable plane. The other planes, such as GaAs(111)A/B, there exist dangling bonds on the surfaces and the surface is likely to undergo surface reconstructions. Thus, for a long time, GaAs(111)A/B surfaces could only be realized by growth with molecular-beam-epitaxy (MBE) techniques[47-49]. Thanks to the improved wafer growth industrial techniques, high-quality GaAs(111)A/B wafers with atomic scale flatness can now be purchased. Nevertheless, these polar surfaces can easily undergo surface reconstructions to minimize the surface energy, such as 2×2 and $\sqrt{19}\times\sqrt{19}$, thus, the surface treatment needs extra care. Surface reconstruction indicates the rearrangement of the surface atoms positions, in order to reach the lowest surface energy. More about reconstruction will be explained later in section 6.2.

Among other crystal planes, the GaAs (100) plane, which is also a polar surface, is often used for in (opto)electronic components. However, I don't discuss much about it since it is not the main part of my research.

2.2 NW growth

A nanomaterial is defined as having one or more dimensions in the nm range. Their extremely high surface to volume ratio makes nanomaterials different to their bulk forms in many ways, for example, their density of states and charge transport properties [50]. NWs are rod-shaped crystalline nanostructures, which have a diameter between a few tens of nm to a few hundreds of nm, while the length can be up to a few μm.

Among all nanostructured materials, III-V nanowires can have a high charge carrier mobility, a direct band gap and other outstanding electronic properties. Semiconducting NWs were firstly reported in 1957[51]. From the beginning of the 21st century, the interests in NWs have exponentially increased since they offer great flexibility in heterostructure growth, combining different materials in each segment with a rather low number of strain-induced structural defects. What is more, III-V NWs have the potential to grow on Si surfaces and thus have a great advantage for being integrated into the present main electronics industry[52-54], as well as being implemented in electronic devices[55,56]. Now it is found that the properties of

nanomaterial-based devices have a large dependence on the quality of the structure and surface of the materials, thus, a well-controlled NW growth is important.

In my research, the NW growth is accomplished by the very closely collaborating MOVPE group at the Solid State Physics division, and the Nano Electronics group at the Department of Electrical and Information Technology. However, NW growth is an essential base in order to understand the following contents in this thesis, so I will give a quick introduction. NW growth is a broad topic, thus, here I only discuss the type of NWs that have been used in my research.

There are two general approaches in realizing single crystal semiconductors in nanoscale. One approach is called top-down, i.e., from bulk to nanostructure, mostly by sophisticated lithography steps, while the other is bottom-up approach, which includes different crystal growth techniques or self-assembly methods.

Among all the techniques, Metal-Organic Vapor Phase Epitaxy (MOVPE) is a highly precise epitaxial growth method which is often used to grow stacking-defect free crystal structure[45,57]. Nowadays, MOVPE has been widely adopted in industrial applications and manufactures. In my work, for example, a MOVPE approach using Au particles as catalysts contributed to the GaAs NW presented in Paper **I**, following the vapor-liquid-solid (VLS) growth mechanism[58], and the $In_xGa_{1-x}As$ NWs in Paper **IV** were selectively grown on an InP:Fe(001) substrate by MOVPE.

Since NWs can be very homogenous along their radial orientation, very often NWs can be considered as a 1D heterostructure material, which varies along the axial direction (the NW growth direction) with different stacking layers or gradients of material composition[30].

If a crystal segment of a NW is only of a small length and limited by the boundaries of the NW, we can call it a zero-dimensional (0D) nanostructure, the examples are a potential well or quantum well/dot. 2D nanostructures, on the other hand, refer to nanomaterials such as graphene and other thin films. An example is the Bi induced 2D honeycomb structure studied in Paper **II**.

2.2.1 Tailored Wz/Zb NW

As mentioned, to achieve the goal of nanomaterials with special electronic properties other than bulk, crystal structures of high quality with as few defects as possible need to be grown in a well-controlled way.

Particle assisted growth

The process of particle assisted MOVPE growth is shown in Fig. 2.3. The seed, which acts as a catalyst, is fundamental for VLS growth process[58]. Traditionally, seed

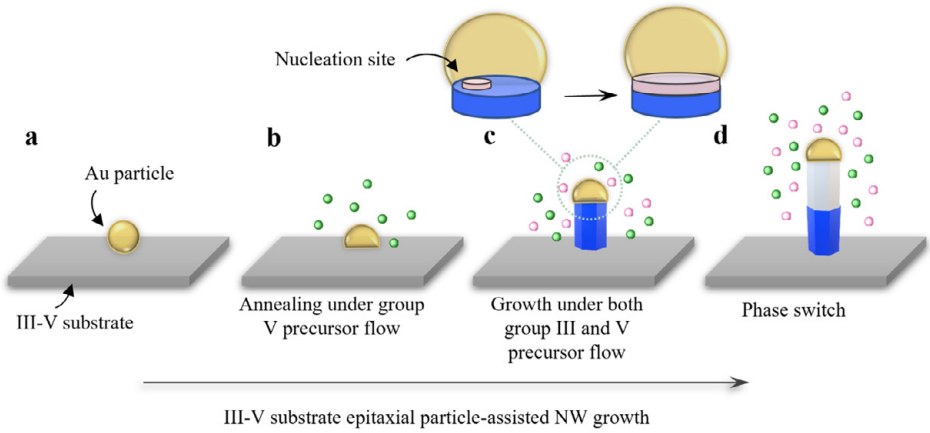

Figure 2.3 The diagram shows the process of nanowire growth with Au particle assisted MOVPE method. a) Au seed is deposited on the substrate; b) Temperature is increased and the group V precursor is flowing in the reactor. c) Introduction of group III and V precursors and growth of the NW. d) NW phase transition by changing the growth parameters.

particles - usually gold (Au) - are used for III-V NW growth. The process can be summarized as follows:

The seed particles are usually deposited using size-selecting aerosol techniques[59]. Since NWs are found to prefer growing in <$\bar{1}\bar{1}\bar{1}$> type directions, the substrate is commonly a (111)B III-V wafer of the intended NW material. The temperature control is rather crucial, typically it is in the range of 400-600°C. The substrate prepared with seed-particles is transferred into a MOVPE growth reactor (Fig. 2.3a). A group-V precursor is introduced while the substrate is annealed (Fig. 2.3b). Later, the growth begins with that precursors flow into the growth reactor (Fig. 2.3c), such as organometallics (e.g., trimethylindium) and hydrides (e.g., arsine). Group-III material (such as Ga or In) provided by the precursors alloys with the Au particle until the particle gets supersaturated – this is when growth starts. New crystalline layers predominately grow at the interface between the particle and the substrate (liquid-solid interface).

Note that the NW grows while nucleation happens underneath the seed particles[45] and that is usually at the VLS interface. A layer-by-layer growth is initiated under the seed particle, so that the seed particle is pushed upwards by the most recently formed monolayer[60]. Recently this growth mechanism including independent monitoring of nucleation and growth as well as different crystal phase formation has been studied by in-situ transmission electron microscopy during GaAs NW growth[60-62]. The interface between the seed particle and the solid semiconductor substantially provides an energetically favoured site for the nucleation of the new solid surface. In the end, a

freestanding NW with the seed particle on the very top is grown with desired length chosen by growth time.

Scanning electron microscopy (SEM) images of some GaAs NWs are shown in Fig. 2.4. One can notice how the diameter of the nanowires is related to the particle dimensions. We usually use a homogenous size of seed particles so that one NW is not that different to another one in the same patch.

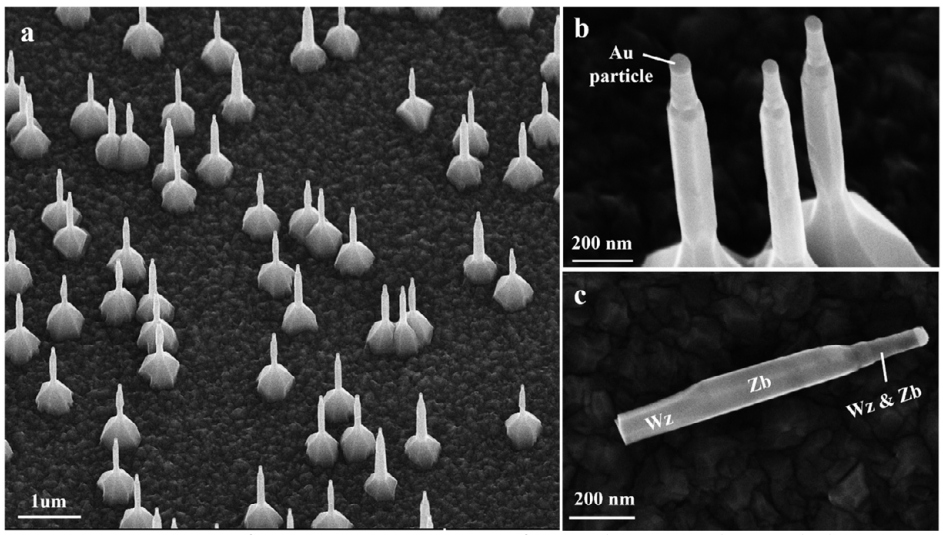

Figure 2.4 SEM images of GaAs NWs. (a) Overview of NWs. (b) Au particle is marked. Larger Au particle corresponds to larger diameter of NW. (c) Wz and Zb segments are marked. This can be judged by the shape of NW facets and the comparison of contrast between different segments. However, it is not always straightforward to see it. (a,b) are on the growth substrate, for (c) the NW has been broken and transferred. Images courtesy of Sebastian Lehmann.

During the growth of NWs, some factors are very critical in order to grow NWs with the desired crystal structures, such as the III-V precursor ratio[57,63], temperature, precursor flux, and so on. Essentially, kinetics plays a central role and therefore the growth is eventually controlled by processes whose rate is limited by temperature. By fine tuning these factors, a well-tailored NW with desired phase can be achieved, such as the Wz and Zb segments marked in Fig. 2.4. More detailed growth can be referred to reference[54,64,65]. Most commonly, NWs have a mixed crystal structure of both Wz and Zb since a Wz nanostructure gets less stable with longer size or length and Zb segments can act as a buffer zone between Wz segments and help to decrease the defect density as well. Nowadays, full control over the phase can be achieved, including pure crystal phase or heterostructures with tailored segment length and atomically sharp interfaces.

2.2.2 Other tailored NW growth

Quantum dot and quantum well

If we even restrict the size of materials down to nanometer scale in a 1D nanostructure of NW, i.e., this material is confined in a very short segment in a NW of a few nm in length, that is normally called a 0D nanomaterial. Thus, the charge carriers can be confined or trapped in specific dimensions down to 0D. Some examples are a quantum dot (QD), if it is a single segment in a NW and has nano-size in all dimensions, or a quantum well (QW) for the case that we need to consider the diameter of a NW for a nm-size sliced nanostructure. The more precise definition is linked to the de Broglie wavelength of the charge carrier: If the extension of the structure is shorter than the de Broglie wavelength in one dimension, the electrons (charge carriers) are confined in this dimension. For example in InAs, the de Broglie wavelength is about 40 nm[66]. The confined charge carriers feature can be interesting for quantum devices, in which a Wz quantum well can be for instance inserted between two Zb segments[64].

NW Radial overgrowth

Except for the ideal axial growth, i.e., the layer-by-layer growth directly under the seed-particle, a radial growth is often observed on NWs as well. The radial growth happens on all the sidewall facets of NWs during VLS growth, with different growth rate for different types of facets. Thus, the base of the NW is very often thicker than the top part around the seed particle because the base part has more radial growth (see examples in Fig. 2.4). Usually some radial growth (vapour-solid type) is inevitable whenever axially nanowire growth happens. The radial growth is generally less controlled, and it can lead to poor device performance[67]. However, uncontrolled radial growth can be suppressed by using in-situ etchants[68].

Nowadays, different methods have been developed for a more controlled radial growth, such as core-shell growth[17,18] even with different material or doping level. Homoepitaxial radial overgrowth can introduce more and different facet types on the sidewalls of NW, resulting in a mixture of facets coming from original axial growth and post radial growth. Thus, heteroepitaxial shell growth can be tuned in order to design radial heterostructures. The extra dimension introduces more possibilities on NW or nanomaterial growth, but nevertheless, controlled core-shell growth is more challenging to achieve.

Lateral NW growth

This method is actually not a specific growth method, but a result from a collection of some slightly different growth approaches, which may have different names but

with similar mechanism. For example, template-assisted selective epitaxy (TASE)[69,70], selective area growth (SAG)[71-73] or selected area epitaxy (SAE). This type of growth method has a feature of particle/seed-free growth, instead, with the aid of apposition of an inert mask.

These methods are especially promising for applications such as metal–oxide–semiconductor field-effect transistors (MOSFET) for radio frequency applications [71,74,75] and for quantum transport in lateral NWs for Majorana-based semiconductor/superconductor qubits[24-28]. In my work, the lateral NWs in Paper IV were grown with this type of method. For more details about this growth one can refer to references mentioned above.

2.2.3 Nanoplatelets

Nanoplatelets are similar to NWs regarding their crystalline structure, but with different heterostructures and sizes. Generally, nanoplatelets have wider facets but with smaller thickness, unlike the cylinder-like shape of NWs. An SEM image of some nanoplatelets is shown in Fig. 2.5, the width of their terraces can be up to 500 nm, with lengths of 1-2 μm. The InAs nanoplatelets with Wz$\{11\bar{2}0\}$ crystal structures in our experiments were provide by our collaborators from Beijing University in form of 20 nm thick Nanoflakes[76].

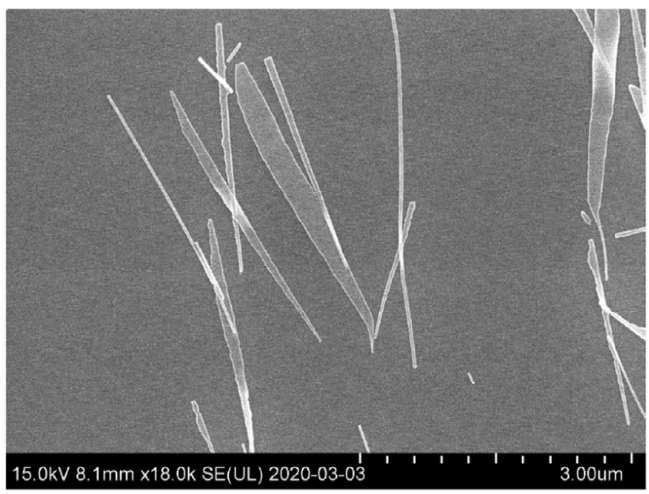

Figure 2.5 SEM images of InAs nanoplatelets. Image courtesy of Sandra Benter.

2.3 III-V Nanowire surfaces

Now we know how the appearance of a crystal facet is basically decided by the crystal structure and its crystal plane orientation. Technically, the surface layer is made up of atoms with a broken crystal symmetry, exposed to the external environment. From this point of view, NW surfaces have nothing different to bulk crystal surfaces. However, some specific crystal structure can only exist in nanowires (for example, Wz structure of GaAs) instead of bulk materials. Thus, the nanoscale materials adds a new dimension to the range of possible surfaces.

2.3.1 Nanowire surface morphology

Despite the fact that a III-V NW can consist of different crystal phases, all crystal segments are stacking on each other with the same growth direction: $[\bar{1}\bar{1}\bar{1}]$ for Zb and $[000\bar{1}]$ for Wz, and the transition can be controlled to single atomic layer precision by e.g. the MOVPE method[15,63,77] introduced in section 2.2.1. The side-wall facets will be different for the Zb and Wz structure, and they typically consist of low-index planes[78]. Usually, Zb segments are terminated with {110}-, {111}A/B- and {112}-type facets, while $\{11\bar{2}0\}$- and $\{10\bar{1}0\}$- type facets are found for Wz. Among them, {110}-, $\{11\bar{2}0\}$- and $\{10\bar{1}0\}$- type facets are non-polar surfaces which have equal amount of both group III and V atoms.

In the Zb segment, {110}- and {112}-type facets are parallel to, or in plane with the $[\bar{1}\bar{1}\bar{1}]$ NW growth direction and there is a 30° angle between these two types of planes. {111}A/B-type facets in Zb have a 19.5° angle to the NW growth direction, forming a zig-zag-like pattern of twin planes with opposite angle. In the Wz segment, both $\{11\bar{2}0\}$- and $\{10\bar{1}0\}$-type facets are parallel to the growth direction $[000\bar{1}]$, they have a 30° angle between them.

The 3D atomic models of Wz and Zb structures are shown in Fig. 2.6, here I will focus on the planes that I studied most on NW facets,{110}-, $\{11\bar{2}0\}$- and $\{10\bar{1}0\}$-type planes. From the top view Fig. 2.6a and b, we see that there is an angle of 60° between adjacent {110}-type facets in a Zb segment; and for a Wz segment, $\{11\bar{2}0\}$- and $\{10\bar{1}0\}$-type planes are usually neighbors, with a 30° between them. Fig. 2.6c, g and h present these 3 model facets in a 2D form, and the differences of the atom arrangements between them are clearly shown. Considering bilayers of atomic planes which contain pairs of group III and group V planes, the structure can be explained

better as in the stacking sequence of ABCABC… for Zb whereas it is ABAB… for Wz. Thus, the different stacking sequence results in atomic chains with about 35.4° angle to the $[\bar{1}\bar{1}\bar{1}]$ growth direction in the Zb{110}-type facet. In the Wz $\{11\bar{2}0\}$-

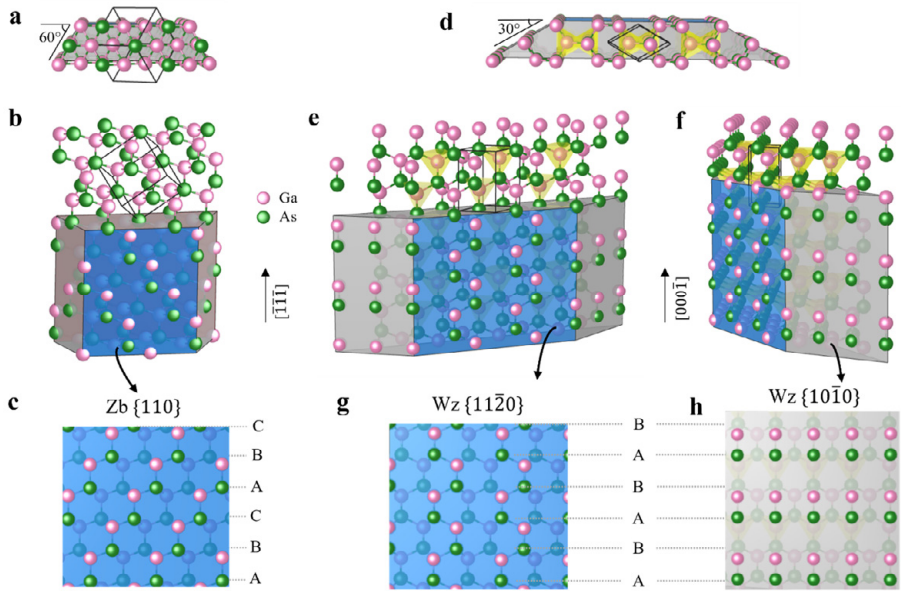

Figure 2.6 The model of (a-c) zinc blende structure and (d-h) wurtzite structure of a GaAs nanowire. (a) and (d) shows the cross section viewing along growth direction. (b), (e), and (f) show the side view while (c), (g) and (h) show the top-most 2 bilayers of GaAs {110}, $\{11\bar{2}0\}$ and $\{10\bar{1}0\}$ plane, respectively. (b), (e), and (f) only present the top-most 3 atomic bilayers of GaAs for a better visualization.

type facet, in contrast, the zig-zag atomic chain, some people also call it armchair chain, is along growth direction $[000\bar{1}]$. In $\{10\bar{1}0\}$-type facets, the zig-zag atom structure still exists, but we can only see half of the atoms on the topmost surface, thus the observed compact atomic chains are perpendicular to growth direction $[000\bar{1}]$. To have a more comprehensive understanding, readers can refer to the figures in reference [21].

Terrace edges

In reality, the crystalline surface is full of atomic steps, as well as terraces in nanometer to micrometer size. I shortly mention the special terrace edges on Wz facets because they play an important role in triggering Bi incorporation, as shown in Paper **I**. For the $\{11\bar{2}0\}$-type facet, terraces favor sharp edges elongated along or perpendicular to the growth direction $[000\bar{1}]$, thus, forming many right-angle corners on the terrace. The steps perpendicular to the growth direction are special, they are one of the positions where nucleation of new layers often starts[79]. These steps are also the first

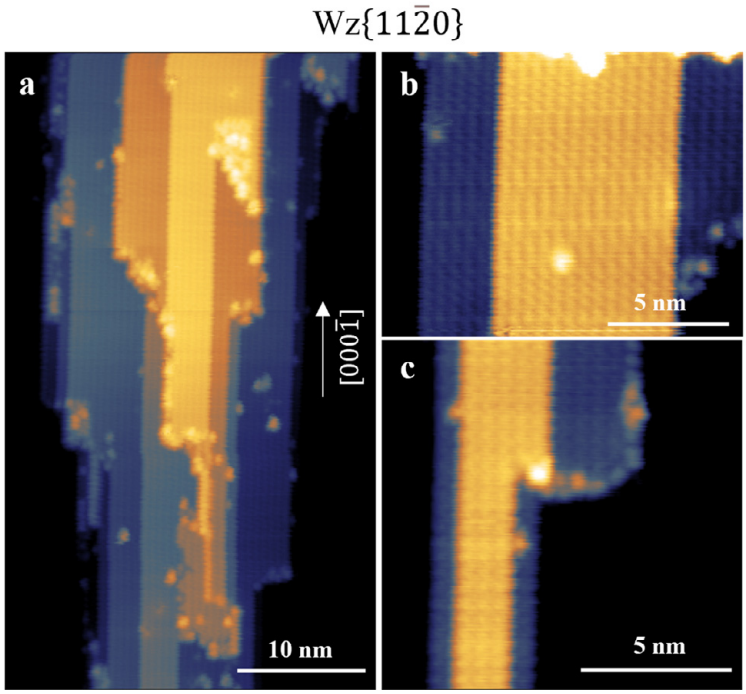

Figure 2.7 The comparison of different terrace size of {11$\bar{2}$0}- type facets and their terrace edges on the same NW surface. (a) Overview STM image. The terrace edges are mostly elongated along [000$\bar{1}$] direction and some are perpendicular to it. Comparison between relatively big (b) and small (c) terraces of {11$\bar{2}$0}- type facets on the same NW, imaged at different position along the nanowire. The brighter atoms (dots) in all STM images are from the incorporated/deposited Bi atoms. V_T = -4.5V.

incorporation sites for Bi on GaAs NW facets (see Paper **I**), indicating they are favorite positions for settling absorbent atoms and even triggering a chemical reaction.

The terrace size can be determined by the growth parameters and the diameter of the NW, varying from a few nm to a few tens of nm, or even up to one hundred nm. In reality, nanowires often deviate from this perfect structure towards a more round cross section. The rounder the cross section of a NW is, the smaller the size of terraces on the sidewalls are. Thus, to have a more comprehensive characterization on the surface of a NW, it can help to move along a NW to look for a flat terrace with target size. An example of the comparison between different terrace sizes in the same GaAs NW is shown in Fig. 2.7.

Wz/Zb interface

As discussed, we know that {11$\bar{2}$0}/{110}-type facets only differ in the stacking orders of Ga/As bilayers. Under a well-controlled growth, the interface between them

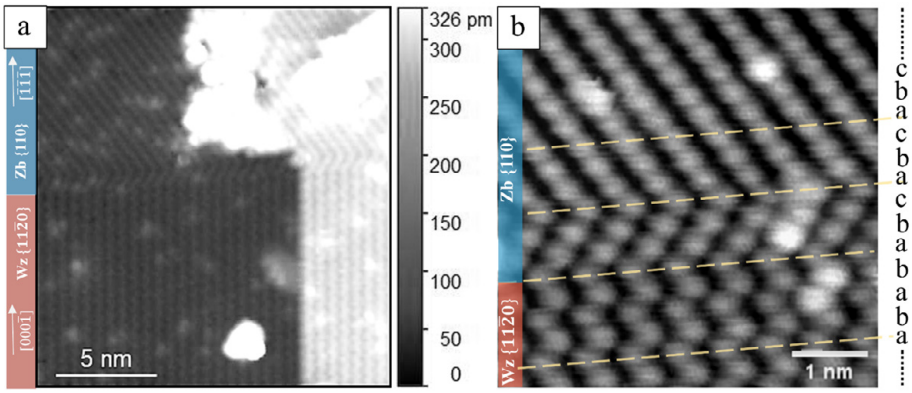

Figure 2.8 Atomic-scale STM images of the interface of Wz {11$\bar{2}$0}- and Zb {110}-type facet. (a) An overview STM image. The bright terrace is one monolayer higher than the darker terrace. Contrast scale bar is on the right. (b) A zoom-in STM image of the Wz/Zb interface. The yellow dashed line corresponds to some "a" in the stacking orders marked in the right. All STM images are filled state images, showing the group-V atoms. Figures adapted and modified from Paper **I**.

can be atomically sharp and smooth. An overview and a zoom-in STM image of a {11$\bar{2}$0} and a {110}-type facet with an atomically sharp Wz/Zb interface are shown in Fig. 2.8a and b, respectively. Terraces with monolayer high surface steps were found on all facets, showing unreconstructed morphology which has the same patterns as expected from oxide-free pure GaAs NWs[19,20]. Some of the stacking orders abab…. and abcabc…. are indicated on the right of Fig. 2.8b. For detailed information about the growth of sharp crystal structure interfaces in III–V NW systems, see reference[57].

2.4 Bandgap of Semiconductors

So far, we have mostly focused on the crystal structure and its different exposed facets, i.e., the surface topography. However, the most important feature of semiconductors, which distinguish them from other materials such as metals and insulators, is the existence of a small bandgap. It is important to introduce this concept, in order to understand the STS studies in Chapter 4, as well as why we need to use higher bias in STM when scanning on semiconductor surfaces.

Compared to insulators and metals, semiconductors have a not too big, finite bandgap, bandgap refers to the energy gap between conduction band (CB) and valence band (VB). Note that the bandgap varies with temperature, and more often, the doping level of semiconductors determines their conductivity. The diagram of

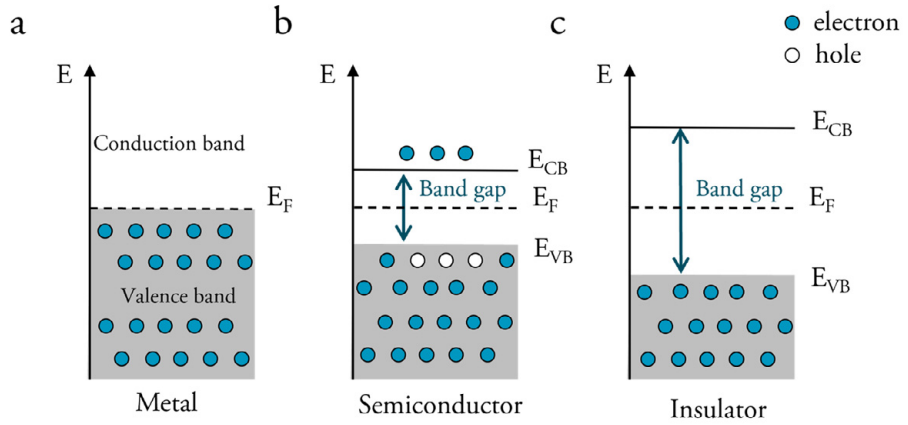

Figure 2.9 Schematic illustration of the band structure of (a) a metal, (b) a semiconductor and (c) an insulator. The Fermi level is denoted as E_F and the band gap is indicated by red arrows. The position of the conduction band (CB) and the valence band (VB) are also indicated in each case.

different band structures between a metal, a semiconductor and an insulator are shown in Fig. 2.9. Conductivity, which is a very important electronic property, is quantified by the density of free charge carriers, it can be either electrons or holes.

In semiconductors, the carriers are not as free as in metals. Electrons are localized in filled states within the VB. However, if the bandgap is small enough, some electrons can be excited into the CB with some outer energy input, such as light, electric fields, or simply being heated up, and of course, only temporarily. One common way to modify the amount of free charge carriers and thus the conductivity of the material is to introduce impurities in a controllable way. This process is called doping, which is a versatile and useful tool in electronics engineering.

III-V semiconductors have a great potential in providing materials of different band gaps, with a high carrier mobility and different charge carrier densities due to different doping[80]. Judging from the type of excessive carriers, there are two major categories of doping, n-type (negative-type) and p-type (positive-type). The former has excessive electrons and the latter excessive holes. Group II atoms (e.g. Zn) are often used for p-doping and group VI atoms (e.g. Sn) are often used for n-doping of III-V semiconductors, sometimes group IV atoms (e.g. Si) are also used. I mostly use the heavily n-doped (Si) GaAs in my research. All the doping elements, Zn, Sn and Si are called dopants. Depending on the amount of doping, the doped materials are classified as lightly doped to heavily doped, with the quantification factor carrier density.

It is interesting to think how doping can influence the Fermi level. For a metal, the Fermi level is defined as the highest energy to which available states are filled with

electrons at 0 K, and only empty states exist above the Fermi level. For an undoped semiconductor at 0 K, the Fermi level is found close to the middle of the band gap. When n-doped, the Fermi level will move towards the CB; Vice versa, for a p-doped semiconductor, the Fermi level will move towards the VB. The Fermi level shifting is the result from the equilibrium of lowest effective mass of electrons (or holes), thus, the Fermi level is not always in the middle of the semiconductor band gap.

3 Scanning Tunneling Microscopy

In this chapter, one of the most important characterization techniques in my research, STM, will be introduced. I will start with the theory behind the tunneling current, and then continue to the basic setup for a functional STM (section **3.1**), the STM tip preparations will be quickly discussed as well. Later, section **3.2** will focus on low temperature scanning tunneling microscopy (LT-STM), with the example of the instrument I operated often, which is a world-leading LT-STM with closed-loop He compressed gas cooling system. After that, I will show you how STM characterization on semiconductors differ from that on metal surface (section **3.3**), some examples of STM images from my research will be presented. In the end, some brief introduction of how to locate NWs/devices on a substrate with a STM probe in a more efficient way will be shown in section **3.4**.

3.1 Introduction

We can start with considering how to characterize a surface with very high spatial resolution. The most straightforward answer would be that we need a characterization interaction which is very sensitive to the topographical changes of a surface in vertical directions. An ideal method would be utilizing tunneling current, which decays exponentially with the distance between the surface and a metallic probe. If we move this probe across the whole surface, then we will have the topography information of the whole surface and form a 2D image. That is the idea behind all scanning probe microscopy (SPM) techniques. Now, let us go back to history where the whole new story began.

In 1981, Binnig and Rohrer invented the STM[81], marking the beginning of a new aera for surface science. Since then, imaging surfaces in atomic scale has become possible. Soon in 1986, Binnig and Rohrer were awarded the Nobel Prize in physics for their development of the technique. Quantum mechanical tunneling is the foundation of STM measurements.

3.1.1 Basic theory of STM

In classical physics a particle is not allowed to cross a barrier which is higher than its own energy. In quantum mechanics, particles have both particle-like and wave-like properties, which implies that the particle can, with some probability, tunnel through the barrier. When an STM tip is brought close enough to a sample surface, which is usually a few nm, the only barrier between them is a thin vacuum gap, which can also be considered as an energy barrier. The thinner the energy barrier is, the higher the chance is for the tunneling. The solution of a time-independent Schrödinger equation describes a plane oscillatory wave which experiences exponential decay in the barrier as:

$$\psi(x) = \psi(0) \cdot e^{\frac{x}{\hbar}\cdot\sqrt{2m(\Phi-E)}} \tag{3.1}$$

where x is the position within the barrier, m is the electron mass, Φ the height of the potential barrier, and E the energy of the electron wave function. For a finite barrier of width d, the probability of tunneling intensity is defined as:

$$T = \frac{|\psi(d)|^2}{|\psi(0)|^2} = e^{\frac{-2d}{\hbar}\cdot\sqrt{2m(\Phi-E)}} \approx e^{\frac{-2d}{\hbar}\cdot\sqrt{2m\Phi}} \tag{3.2}$$

the approximation made in the end of the equation is based on the assumption that V_0 is much larger than E. Indeed, the tunneling probability is exponentially dependent on d, that is the reason for the extraordinary resolution of the STM.

Fermi's golden rule describes the transition rate from one energy eigenstate ε of a quantum system to another as a result of a weak perturbation[82]. This applies also to the tip-sample interaction system in STM, where the electron transition probability from the sample to the tip is:

$$R_{s\to t} = \frac{2\pi}{\hbar}|M|^2\delta\left(\varepsilon_{\psi_s} - \varepsilon_{\psi_t}\right) \tag{3.3}$$

where M is the tunneling matrix, $\hbar$ is the reduced Planck's constant, and δ function means only elastic tunneling is considered. The net tunneling current is obtained by considering all possible energy eigenstates, that is[83,84]:

$$I_{tot} = \frac{4\pi}{\hbar}\int_{-\infty}^{\infty}\rho_s(\varepsilon + eV)\, f_s(\varepsilon + eV)|M|^2\rho_t(\varepsilon)[1 - f_t(\varepsilon)]d\varepsilon \tag{3.4}$$

in the formula, ρ_t and ρ_s are the density of states of the STM tip and the sample, respectively, and f is the Fermi distribution, defined as:

$$f(\varepsilon) = \frac{1}{1+e^{(\varepsilon - E_F)/kT}} \tag{3.5}$$

Density of state (DOS) is also an important concept, which means the number of states at a particular energy level, i.e., the distribution of states over energy. According to the Bardeen formalism[84], the tunneling matrix M can be expressed as:

$$M = \frac{\hbar^2}{2m}\int_S \psi_s^* \boldsymbol{\nabla}\psi_t - \psi_s \boldsymbol{\nabla}\psi_t^* \; d\boldsymbol{S} \tag{3.6}$$

where ψ_t and ψ_s are the wave functions of the tip and the sample, respectively, and the integral is calculated over the surface $S_{tip/sample}$ of separation between the sample and the tip.

To even simplify this formula more, we use Tersoff and Hamann's approximations[83], which includes that the STM tip has an s-type wavefunction with a constant density of states (DOS), thus, ρ_t becomes constant. Also, in M, it can be expanded in Bloch surface waves. The approximation also considers the tip with a circular apex.

Together with the assumption that at low temperature the Fermi distribution becomes a step function, i.e. f is 1 for all status at energy below fermi level E_F, and is 0 when energy is higher than E_F. Then we have:

$$I_{tot} = \frac{4\pi}{\hbar}\rho_t \int_{E_F - eV}^{E_F} |M|^2 \rho_s(\varepsilon + eV) d\varepsilon \tag{3.7}$$

Now the tunneling current is already much simpler!

In the case of scanning on metals, small tunneling voltages are sufficient and the integral over the energy eV can be approximated by a linear voltage dependence V: It can be shown that then the current is approximately proportional to the applied voltage and the local density of states (LDOS) of the sample at the Fermi energy E_F:

$$I_{tot} \propto V \cdot \rho_s(E_F) \cdot \rho_t(E_F) \cdot e^{\frac{-2d}{\hbar}\sqrt{2m\Phi}} \tag{3.8}$$

By simple calculations we know when d decreases by 1 Å, I_{tot} will increase by a factor of 10. At a fixed location z of the STM tip on the surface, the tip-sample distance d is fixed. Assuming the tip is well conductive and has a constant ρ_t, then this equation can be understood such as the tunneling current is proportional to the product of bias V and the $LDOS$ of the sample evaluated at the position where the tip is:

$$I_{tot} \propto V \cdot \rho_s(E_F, z) \tag{3.9}$$

When scanning on semiconductors, the approximation of a small voltage is no longer valid, and instead we have:

$$I \propto \rho_t \int_0^{eV} \rho_{s,loc}(z, E_F + \varepsilon)\, d\varepsilon \tag{3.10}$$

That means, the tunneling current is proportional to the LDOS of the sample integrated over the energy interval defined by the tunneling voltage. Tersoff and Hamann's approximation has clearly shown the direct correlation between the STM tunneling current and energy integrated LDOS.

It is worth pointing out that the actual shape and electronic state of the tip is not included in the Tersoff-Haman approximation, which instead requires that the tip is constant and isotropic[85]. Thus, the main contribution to the tunneling current arises from an s-type orbital. The contrast observed in the STM images can highly depend on the state of the tip and it is very critical to use a well-conditioned sharp conducting tip, to avoid extra complexity in interpretating STM images. More details about tip preparations and tip-induced effects can be seen in section **3.1.3**.

Also, other assumptions of the Tersoff-Haman approximation are not always easy to satisfy (that is why it is called an approximation!), for example, tip and sample are at low temperature. We can at least work on the low temperature, more about LT-STM will be explained in section **3.3**.

3.1.2 STM Setup

The ultimate goal of the whole STM setup is to bring the sharp tip to a very small distance to sample surface (in nm scale) in a controlled way and scan the tip over the surface with a high precision in position. There are three group of instruments to realize it, the coarse motors, piezo motors, and feedback system. Unlike to the schematic diagram shown in Fig. 3.1[86], most STMs have the sample facing downwards, while the tip is pointing upwards.

Piezoelectric material is widely used in moving material precisely. Coarse piezo motors are used to roughly position the tip on the desired position on the sample. This is accomplished by adjusting the sample-tip relative positions in x, y, z directions with piezo motors. In some models, coarse motors are integrated with the tip-piezo tube part. However, some exceptions can be found, for example, the closed loop He cooling LT-STM has x and y coarse motors connected to the sample stage, and the z coarse motor to the tip. More details will be presented in section **3.3**. A typical distance of a coarse step in z direction is 1-2 μm, and for x and y, it can be a few hundreds of nm.

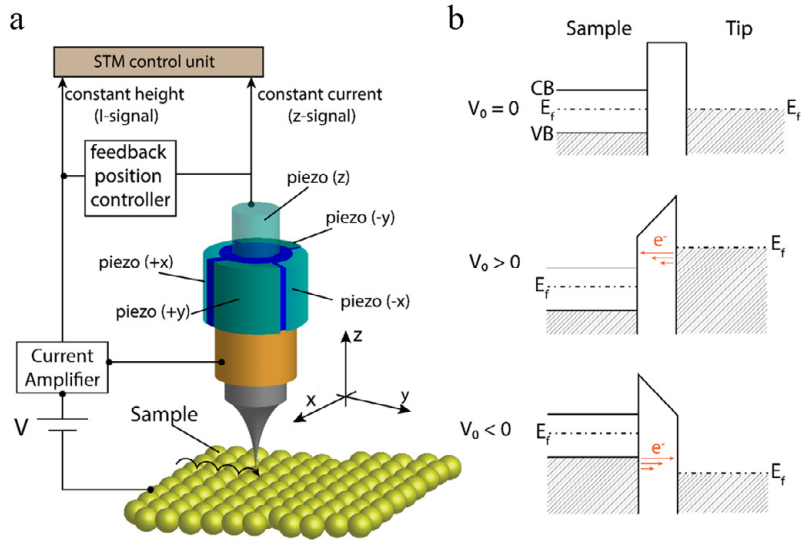

Figure 3.1 a) STM setup: the tip is scanned on the sample surface in the x and y directions with the corresponding piezo motors and the tunneling current is recorded. The STM can work in constant height or in constant current mode, in the latter case a feedback loop is present to reposition the tip with the piezo motor (z). b) An STM metallic tip can probe filled ($V_0<0$) or empty states ($V_0>0$) of a semiconductor sample. The filled states are indicated as dashed area. On the top no net tunneling current is present since the system is at equilibrium. (Adapted from reference [86])

After manually approaching the tip, the auto approach procedure is done by the feedback loop and its software. The auto approaching will stop when it reaches the desired value of tunneling current under the applied bias between the tip and sample, which is usually in the range between a few nA and about 100 pA. At this stage, the tip is very close to the sample surface, usually less than 1 nm. During scanning, a piezo tube scanner (see Fig. 3.1a) is used to control the tip position in x, y and z direction with sub-Ångström precision, thus, resulting in a very high spatial resolution in STM images, under the condition of a very sharp tip.

More specifically, the feedback detects the measured tunneling current and compares it to a pre-set value. By moving the z-piezo as a response, the real time tunneling current can be kept as nearly constant. In this way, the movement of the tip piezo in z direction is picturing us the topographical information of the surface. This mode is called constant-current mode. The other scanning mode is called constant-height mode which is not so commonly used. The feedback loop is kept inactive and z is constant during scanning, while the tunneling current variation is being measured. This mode has disadvantages such as a higher risk of crashing the tip into the sample surface.

The tip-sample distance and its dynamics during scanning are mainly controlled by tunneling bias and current as well as the loop gain. The latter is basically a value deciding how fast the feedback loop should respond on the height changes of the tip. Functionally, the loops consist of derivative, proportional, and integral gain in the calculations in the feedback loop. A higher loop gain means quicker reactions but may induce unwanted signal oscillations, while a too low gain can result in lower topographical precision and in worse case the tip may crash into high obstacles because of too slow reaction. Thus, a high loop gain is very useful when scanning a rough (still in nm scale) surface, and lower gain should be used in the case of super flat (a few nm or Å scale) surface and when pursing atomic scale. During STM measurement, the distance between the tip and the sample can be adjusted by the bias and tunneling current. According to Eqn. 3.8, we know that if we want to keep the tip far away from the sample, low tunneling current and high bias should be chosen, and vice versa.

Ultrahigh vacuum

STM is usually conducted in an ultrahigh vacuum (UHV) environment, which means a vacuum of 10^{-7}–10^{-12} mbar. It takes some effort to reach and maintain the UHV environment for STM measurements. Sometimes people might wonder, is it really necessary to have UHV?

There are a few reasons for that. The main reason is to avoid surface modification, for example oxidation of the surface or contamination by a water film that would happen rather fast if under ambient conditions. Surface molecular condensation is even more obvious for LT-STM, since the whole cooled down part, including the sample, is acting like a cryopump which condenses rest gas molecules to the pump surface, thus keeping good vacuum. We can understand this with some simple calculations. Even at the pressure of 1×10^{-6} mbar, according to the kinetic theory of gases $Nk_BT = pV$, where p is the pressure, V the volume, T the temperature, k_B the Boltzmann constant, and N the number of molecules, each molecule on the sample surface is on average hit by a residual gas molecule once per second. For atomic resolution, UHV with less than 10^{-6} mbar is necessary, mostly because it is needed to keep the surface clean and stable.

3.1.3 STM tip

The quality of STM images depends heavily on the tip quality. A conductive and well-shaped tip is the first step for successful STM measurements. To image surfaces with a high aspect ratio, such as high density of terrace steps or nanowires, a sharp tip

becomes very important. Here I introduce STM tip preparations as well as give some examples from tip effects.

Tip preparation

I mostly use tungsten (W) wire to make an STM tip, with the most common method of electrochemical etching (Fig. 3.2). W is a stable, cheap, and easy-to-handle material.

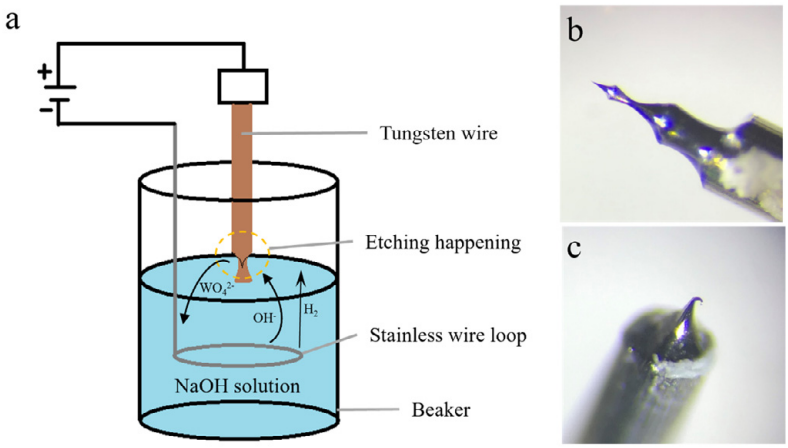

Figure 3.2 a) Schematic diagram showing the chemical etching process of the tip. b) An interesting etched tip with several etching steps, but in the end the apex of the tip is sharp and in a nice shape. c) A bent tip taken out from the STM chamber. When I saw it I understood why I couldn't get nice STM images for days.

Fig. 3.2a schematically shows the commercially available setup (Omicron) for DC electrochemical tip etching. I mostly use a 0.3 mm diameter polycrystalline W wire, which acts as the anode. The ring of stainless-steel acts as the cathode in the solution of sodium hydroxide (NaOH, 2 mol/liter). A voltage around 4-9 V is applied and W atoms are oxidized with OH^- and become WO_4^{2-} which gets resolved into the solution, while H_2 produced at the cathode is released into the air.

The W wire, which is etched at the electrolyte/air interface, gets thinner and thinner, as indicated by the yellow ring in Fig. 3.2a. Finally, the bottom part will be cut off and drop. Immediately after etching, the tip should be rinsed with distilled water and ethanol to reduce the amount of etchant residue. Some interesting photos of STM tips are shown in Fig. 3.2b and c. The tip in Fig. 3.2b is a result of unsmooth tip etching process, but still with sharp tip apex. The bent tip shown in Fig. 3.2c presents the shape that a tip should not have.

The freshly etched tip still has a thin layer of oxide, residues, and surface contaminations on the tip surface. There are several ways to remove them after inserting the tip into vacuum. One way is to sputter the tip with argon (Ar+) for 20 minutes at a pressure of 2×10^{-5} mbar, usually I use the acceleration voltage for the argon gun 3 kV and the emission current is set to 20 mA. Electron bombardment works in a similar way, just Ar+ is replaced with accelerated electrons. The other way is called direct current annealing. The setup encloses the tip into an electric circuit, so that the tip is heated up when there is high current passing through it. When the temperature reaches around 1075K[87,88], WO_2 will sublimate, thus a clean metallic tungsten surface is left behind[87,89,90]. Normally I use the glowing color of the tip to estimate the temperature, when the color is changing from red to orange it is roughly 1100K. WO_2 sublimation is quick, staying at 1100K for a few seconds would be enough. For a 0.3 mm diameter W tip, the heating current would be no more than 18 A. Keep an eye on the pressure, it may increase dramatically with such a high temperature object. One advantage of this annealing process is that it can also remove the crystallographic defects generated by the electrochemical etching and make the tip surface smoother[91-93], if you don't overheat it. I would also keep the tip at the current of 9A for a few minutes before completely cooling down.

Double tip effect

Here I give an example of how double tip effects in an STM image look like (Fig. 3.3), which is a result of more than one apex of the tip, and they are in a detectable distance between each other. From the mathematic deduction (Eqn. 3.4) in previous sections, it is clear that the intensity of STM images is always a convolution of the tip shape and the actual surface structure. In an STM image the

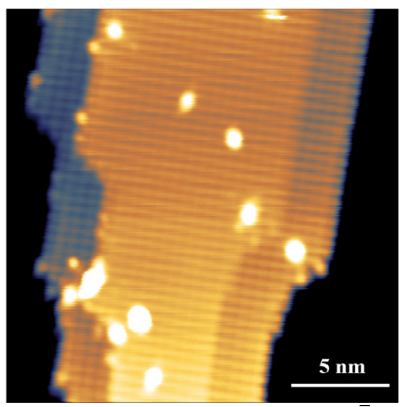

Figure 3.3 Double (multiple) tip effect in an STM image on a $\{10\bar{1}0\}$ facet of a GaAs NW surface. There are at least 3 sharp apexes on this tip, being about 3 nm away from each other.

double tip effect is shown as the repetition of the same surface structures several times, and with an overlapped contrast if the distance between double tips is close enough.

Sudden change of the tip

Although a tip may be in perfect condition in the beginning, it is still very common that it encounters a sudden change during scanning. An example of the suddenly changing tip during one STM image is shown in Fig. 3.4, which is taken on a Bi-induced honeycomb structure on GaAs(111)B. With the same tip and surface structures, very different contrast in STM images can be observed. The white dashed rectangular shapes mark the same structures so that the comparison is clearer. Based on simulations and surface states calculations, the two Bi atoms within the rectangular should have an identical density of states. Thus, we attribute the non-even contrast between neighboring Bi atoms (as highlighted by the rectangles) in the bottom part of Fig. 3.4 to the asymmetric shape or electrical polarity of the tip.

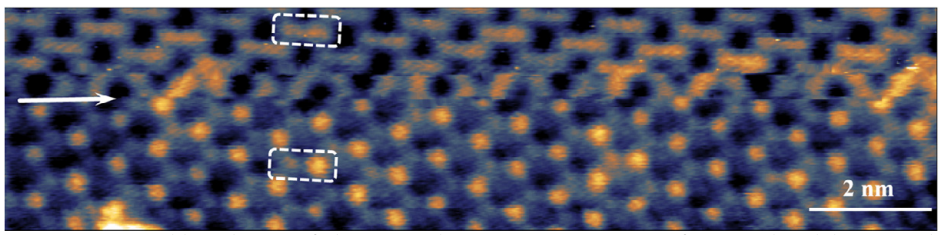

Figure 3.4 A sudden change of the tip is shown in STM images of a Bi-induced honeycomb structure on GaAs(111)B. The scanning line where the tip changed is marked with a white arrow, the apparent features above and below this line looks very different. The white dash rectangular shapes mark the same structures but shown as different contrast.

3.2 Low temperature STM

STM can be operated under different temperature. So far, the world leading low temperature (LT-) STM is operated at 10 mK[94], which has a ^{3}He-^{4}He gas handling system. Variable temperature (VT-) or high temperature STM which is integrated with a heating mechanism is more often used for *in-situ* STM measurements during e.g. surface treatment, catalysis, or chemical reactions.

In this section, I will introduce the difference between LT-STM and room temperature STM, with a focus on semiconductor surfaces. Later the special closed

cycle compressed He gas cooling STM which has been used often in my research will be presented.

3.2.1 LT-STM on semiconductors

At low temperature, the diffusion ability and mobility of atoms are reduced, this gives the opportunity to image a more stable surface topography. Room temperature experiments sometimes suffer from temperature variations (e.g. when a sample was heated) and the resulting thermal drift.

Thermal drift can be a real problem when it comes to atomic resolution imaging, since the images are distorted and the relative position between the tip and the sample is constantly changing. In LT-STM, the cooling system offers a more thermal stable environment, thus, thermal drift is a much less severe problem, compared to room temperature STM. In typical room temperature STM setups, a temperature change of 1 degree Celsius can change the relative tip-sample position by tens of nm. Typical drift velocities at room temperature are up to several nm/min, while at low temperatures, drift rates as small as a few Å/hr are obtained[95], with our instrument we have even observed less than 1 Å/hr.

In STM the scanning piezo materials give fixed transformation between voltage and physical dimensions under stable temperature. However, after continuously changing its size for long, a piezo tube will experience thermal expansion due to the generated heat. In this way, the piezo tube may not be able to bring the tip to the desired location. This happens since the polarization of the domains in the piezo material is not obtained instantly when the voltage is changed, but some of the domains, and with this the entire piezo, need time until they reach their final length corresponding to the applied voltage. This phenomenon is most often observed in the start of a scanning process right after tip approach on the sample surface. Usually in less than a few tens of minutes the strong creep should be gone.

Another advantage of LT-STM is that a condensed 2D electron gas (2DEG) can be observed more easily. Confined electrons on surfaces were firstly observed on metals, as a 2D nearly-free electron gas[96]. The direct visualization of the wave pattern of surface states was by LT-STM at 4K by Crommie et al on Cu(111)[97] in 1993. According to Crommie, the confined electron states can only be observed at up to 77K. The inability to image standing waves in the LDOS of Cu at room temperature may be due to the destruction of quantum phase coherence from inelastic scattering, or to instrumental limitations. Nevertheless, this wavelike pattern of electron gas is an extremely good examples in proving the wavelike nature of electrons.

However, no free electrons exist in an intrinsic bulk semiconductor, instead, they are electrons in covalent bonds, but the wavelike nature of electrons does not change.

However, as mentioned in Chapter 2, the broken dangling bonds of the atoms on III-V surfaces can cause electron accumulation and result in surface states, which can create a surface 2DEG. It is known that there exists a confined 2DEG in the surface accumulation layer of InAs(111)[79,98] and GaAs(111). One example of a 2DEG on InAs (111)B is shown in Fig. 3.9c. It is worth pointing out that even though a 2DEG brings more contrast in STM images, the topography may be still atomically flat.

Moreover, at low temperature, one of Tersoff and Hamann's approximations – the Fermi distribution function as a step-like distribution- is finally realized. In theory it is more correct to announce that the tunneling current is proportional to the LDOS of the sample at the position where the tip is located at the Fermi energy E_F (see Eqn.3.10).

The importance of low temperature is even more stressed and clearer when it comes to STS because of the better energy resolution, which will be introduced in Chapter 4.

However, one drawback of low temperature is that the extension range of the piezo materials is shortened, thus the size of scanning area shrinks in LT-STM. The scanning range of the piezo in x, y direction is typically around 1 μm for LT-STM (around 2 μm in the model that I used), while around 10-20 μm for a STM at around 300K. Note that a distance recalibration will be needed when changing the operation temperature. The scanning speed is normally lower at low temperature as well. In conclusion, if one is looking randomly for an object or a certain surface feature with LT-STM, it may take longer time. Thus, playing with LT-STM is requiring patience.

3.2.2 Closed-cycle cooling

To cool down an STM to 4-10K, Helium (He) is the most commonly used cooling media since liquid He has a rather low sublimation temperature. The most common model of LT-STM in market is liquid He (LHe) bath cryostat STMs, and now the third generation is available. Its working mechanism is to cover the whole STM head in the middle of a LHe Dewar cylinder which is surrounded by a layer s of liquid nitrogen (LN) cylinder to slow down the heat transmission. This model can hold the system at stable low temperature for around 65 hours (for Omicron model) before LHe needs to be refilled again. However, the system is generally bulky and filling LHe may take a while, and mostly two people need to be present. The main drawbacks are that measurements have to be interrupted when filling up LHe, and the He prices, which have increased dramatically recently. Another cooling mode is called flow mode, where the STM is mounted directly onto a continuous flow LHe

cryostat which allows cooling the tip and the sample to about 5-7 K. This model is more compact, but the minimum helium consumption is about 1 liter/hour.

For my experiments, I used two types of LT-STM. One is the LHe bath cryostat STM at 4K provided by ScientaOmicron, some of the STM images have been published in Paper **I**.

The other type is equipped with closed-cycle compressed He gas and the LT-STM can be cooled down to around 8K. For example, RHK technology offers this type of closed-cycle LT-STM. The LT-STM that I have operated is the first instrument of this type provided by Sigma Surface Science (now part of ScientaOmicron), which has been installed when I started my Ph.D. Being one of the first few users of this LT-STM, quite some time has been spent on studying the operations and the mechanism of it (that is also why I put quite some weight on it in this thesis). The Closed Cycle Pulse Tube Cooler system has several advantages over the traditional LT-STM, for example, very low He consumption and continuous operation without need for He refilling. The schematic diagram of the LT-STM and its cooling connections is shown in Fig. 3.5. It contains three parts, the compressor, the cooler, and the STM.

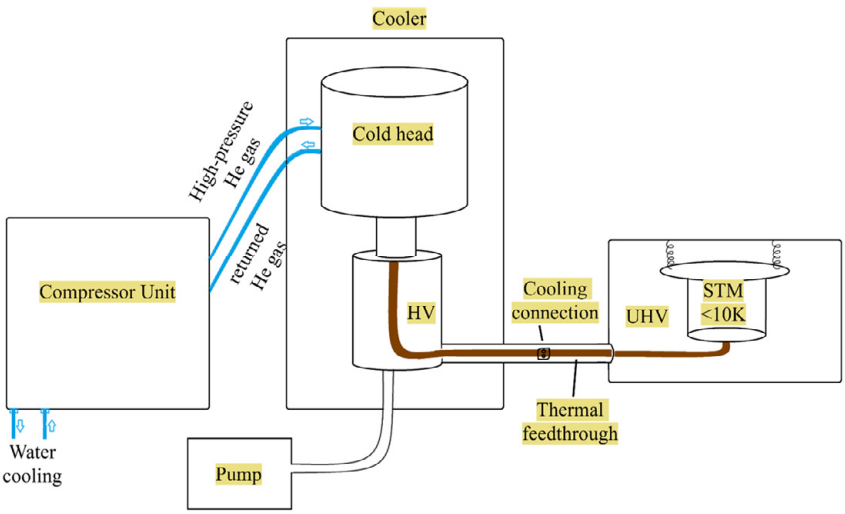

Figure 3.5 Schematic diagram of the low-temperature STM cooling system cooled with compressed He gas.

The function of the compressor unit is to supply high pressure He gas to the cold head and re-compress the He gas returned from the cold head. The compressor unit contains several parts, however, here we do not discuss the detailed function of each part since it is out of the scope of this thesis. In general, the compressor receives the low pressure He gas discharged from the cold head to the compressor unit. After

passing through a storage tank and a filter, the low pressure He gas will be compressed and pressurized in the compressor capsule and in the end, the high pressure He gas (about 1.70 MPa) will be supplied to the cold head. In the compressor, cooling water is needed to absorb the heat from the compressed He gas.

The cooler mainly contains two parts: the cold head unit and pulse pump. After receiving the high-pressure He gas, the cooling process takes effect, where the compressed He gas is released through a valve and thus the gas is cooled down. After that, the evaporated low-pressure He is returned to the compressor unit. It is important to keep a good insulation vacuum as the residual gas/molecule condensation on the cold surface can seriously influence the cooling efficiency. There is a thermal connection between the cooler and the STM head, which transfers the heat away from the STM scanning unit. The thermal connection is the heart of the closed-cycle STM: It has to provide very good thermal connection, with very low mechanical coupling, since the strong mechanical vibrations from the cooling unit must not reach the STM. Note that the thermal feedthrough does not break any vacuum so that UHV can be maintained well in STM.

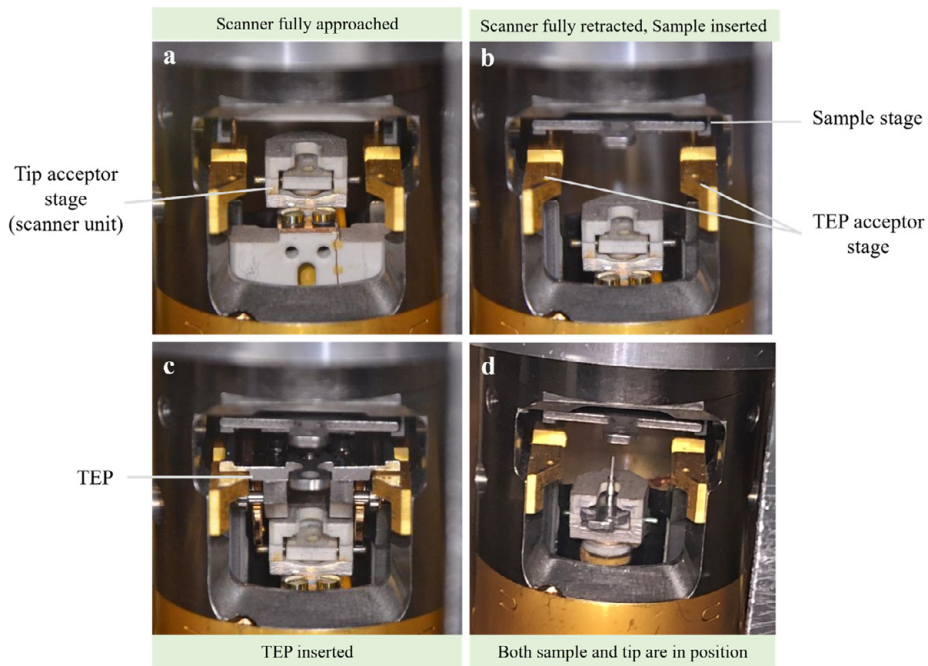

Figure 3.6 a) Scanner (tip and the piezo tube) fully approached position b) Sample inserted c) Tip exchange plate (TEP) inserted; a tip can be introduced now. d) Tip inserted, ready for approach and scanning.

The cooling down process roughly takes 35-40 hours. Once the minimum temperature is reached, the valve of the HV vacuum chamber can be closed since now the vacuum is sustained by the Pulse Tube cooler only, which has a cold surface and acts like a cryo-pump. The maintenance is much simpler compared to non-closed loop cooling as well. One just needs to change the cold head and the He gas filter every 20,000-30,000 hours.

Another feature of this closed loop cooling STM is that it has independent tip and sample exchange mechanism, i.e., the sample can remain in the scanning position when inserting or exchanging tip. This is especially useful when investigating semiconductor nanostructures, where the tip needs to be replaced far more often than in studies on flat metallic surface. The tip and sample inserting process is indicated in Fig. 3.6 a-d.

From Fig. 3.6, we see that the SPM head consists of two main parts. The upper part contains the sample acceptor stage including lateral coarse motors for the sample movement. The lower building block contains the tip acceptor stage, the piezo tube scanner (for fine positioning and scanning) and the vertical coarse motor. Tip and its piezo tube are always located in the middle between the two brackets that hold the TEP. Instead, the sample can move in the 2D coarse movement powered by electronic motors. Nevertheless, when it comes to the scanning mode, the scanning area where the tip locates is controlled precisely by the tip piezo, down to sub Å.

As the tip carrier is held by a central spring within the tip acceptor stage, one needs to first release this spring in order to loosen the tip carrier. For this, a dedicated tip exchange plate (TEP) (Fig. 3.6c) has been designed that needs to be introduced into the STM head before a tip can be taken out or put into the SPM head. The TEP has two springs on left and right side which need to be calibrated for different STM setup (Fig.3.7), in the end, each TEP can be inserted smoothly and open the tip clamping spring with the right amount of force. At the same time, the TEP can lock the tip

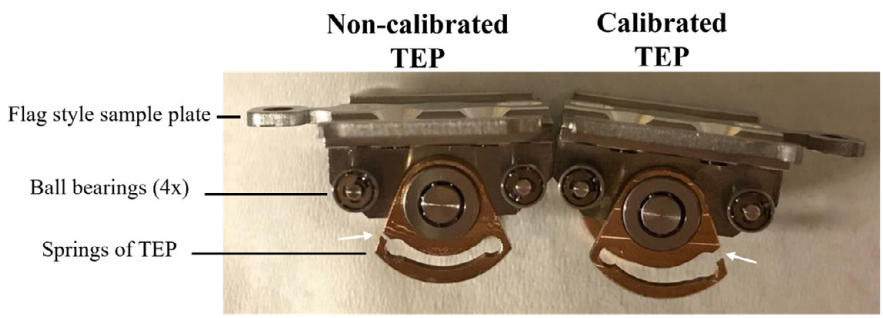

Figure 3.7 Non-calibrated Tip Exchange Plate (TEP) on the left, and calibrated TEP on the right.

acceptor stage/scanner unit against vertical and lateral movement, protecting the scanner when operating with the wobble stick and the tip acceptor stage. Because of this dedicated design, one needs to pay extra attention when operating and avoid applying too much force that could break the scanner unit. Be aware that the repair can take a few months.

Lastly, the STM sample holder is equipped with ten electrical contacts, which can be used to measure small devices at low temperature, for example, a single NW based device.

3.3 STM imaging on semiconductor NWs

In section 2.4 I introduced the bandgap of semiconductors, and later on in section 3.1 the theory of STM tunneling current has been presented. Now we can combine these two parts and see a few examples of STM imaging on semiconductor NWs. Challenges of locating the tip at the NW site facet are discussed in section 3.4, and once on that facet, it locally behaves comparably to a large, flat surface.

The major difference between STM scanning on a metal and a semiconductor surface is that there exists a bandgap for the latter case. Thus, much higher bias should be used, which is normally in the range of a few volts. Moreover, the chemical bonding is in the form of covalent or ionic bonds instead of a delocalized electron gas as in metals.

As we know, STM maps the density of electronic states of a sample surface[99], and it

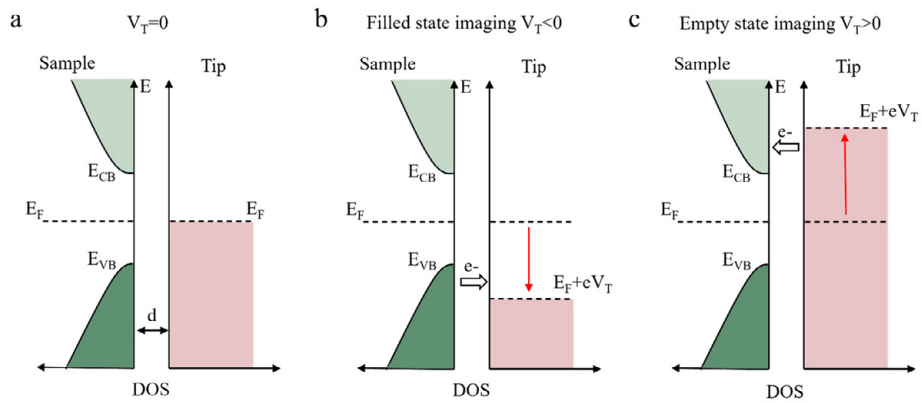

Figure 3.8 Energy diagrams of a metal tip and semiconductor surface under bias with different signs in STM scanning. a) No bias. b) Negative bias. c) Positive bias. Note that in all cases, the bias is applied to the sample, and the tip is grounded.

can probe empty or filled states depending on sign and magnitude of the bias. This is even more crucial in case of III-V semiconductors, because the group-III and group-V atoms have different electronic polarities. In general, group-V atoms are more electronegative, while group-III atoms are less electronegative. For a III-V semiconducting sample the electron orbitals corresponding to filled and empty states are reported to be localized around one element each[100]. The empty states are found around the group III atoms and the filled states are found around the dangling bonds of the group V atoms, giving an elemental specific image contrast.

Fig. 3.8 shows the energy diagrams depicting a metallic tip and a semiconducting sample under three different cases, (a) no bias, (b) a negative bias applied to the sample and (c) a positive bias. In Fig. 3.8a, the Fermi levels of the tip and the sample are aligned without a bias, and thus no net tunneling current exists. Since in Fig. 3.8b the tunneling bias V_T is negative, the relative Fermi level between the tip and the sample has an energy difference of eV_T. Then electrons will tunnel from filled states in the sample to empty states above the Fermi level of the metallic tip. While in Fig. 3.8c, where V_T is positive, electrons will tunnel from filled states below the Fermi level of the metallic tip into the empty states in the conduction band of the semiconducting sample. Note that the bias is applied to the sample, and the tip is grounded in all cases mentioned in this thesis.

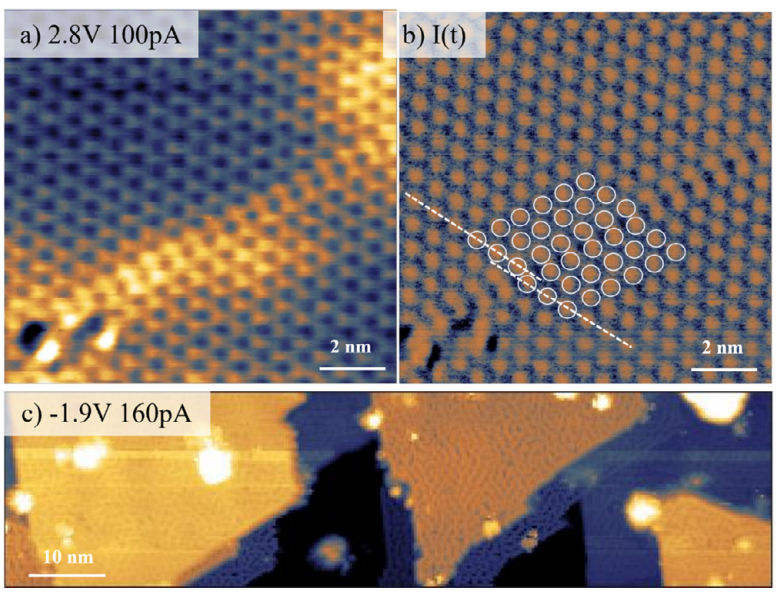

Figure 3.9 a) LT-STM image of clean InAs(111)B under positive bias (a) and its tunneling current map (b), and (c) the STM image under negative bias.

If the bias magnitude is so small that V_T falls within the band gap, of course there would still be no tunneling current. This can be dangerous during STM scanning because the feedback loop would try to decrease d in order to reach the current set-point, which can cause a tip crash into the sample.

As an example, Fig. 3.9 presents STM images of a clean InAs(111)B surface under different negative and positive bias. We can see that the empty states STM image (Fig. 3.9a) and filled states image (Fig. 3.9c) present different tomographs. Fig. 3.9b is the tunneling current image which is recorded simultaneously with Fig. 3.9a, here each bright dot indicates the dark hole surrounded by three atoms in Fig. 3.9a. Though in principle tunneling current should be constant, there still exists a delay for the feedback loop reaction. So, we can in some sense understand the current map as the derivative of the topography map, and sometimes the contrast is clearer.

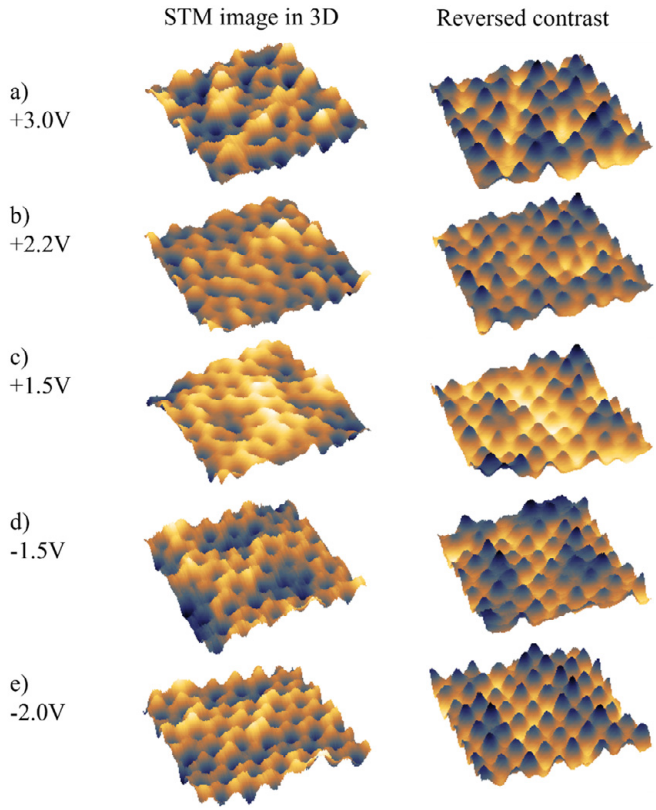

Figure 3.10 a) to e), STM images and their reversed contrast images in 3D of a Bi-induced honeycomb structure on the GaAs(111)B surface under a series of bias. Although the contrast can be fluctuating, all STM images show the same honeycomb structure, and the locations of the bright dots corresponding to individual atoms are constant throughout the bias set. This can be more easily observed in the reversed contrast images on the right.

In the empty states image, well-ordered individual atoms (in this case, we are seeing In atoms) are located in the (111) lattice plane. An atomic-scale defect (a stacking fault leading to lattice misalignment) is more obvious in Fig. 3.9b, indicated by white dashed lines. In the filled states image of Fig. 3.9c, which is taken at another position on the surface, in contrast, an unordered pattern at the atomic scale can be seen on the flat terraces, which are interrupted by surface steps. Note that all STM images were taken at around 10K. This unordered structure is highly likely related to a 2D condensed electron gas on the InAs(111)B surface at low temperature. In Paper **II**, a similar irregular atomic-scale pattern on GaAs(111)B at 10K is observed as well.

From another point of view, changing the sign of the bias is a quick way to check both polarities on the sample surface. What is more, the magnitude of V_T is also a practical and quick way to distinguish electronic structure contrast from topographical contrast in an STM image, since the former one is strongly dependent on the value of V_T. If the contrast in STM images does not change much under different bias, we can attribute the contrast mainly to the topography.

Another example is given in Fig. 3.10, where a Bi-induced honeycomb structure on the GaAs(111)B surface is imaged by STM under a series of bias, from positive to negative. By carefully comparing the images, we see that the primary contrast skeleton- the honeycomb structure- doesn't change, but only the contrast evenness. Considering that neither Ga or As atoms can be observed on both polarity bias, this result implies that the honeycomb structure is made up of only Bi atoms. More details can be found in Paper **II**.

3.4 Navigating the STM tip to the nanostructure of interest

It can be challenging to locate a NW with diameter of a few tens of nm over the entire sample in the size of a few square millimeter. That is why we need to use some markers to help us locate specific NWs and NW devices more efficiently, in the case of a low density of randomly distributed NWs, and even more for the special design of processed NW devices (Fig. 3.11a). The most common way is to utilize metal markers which are usually done by photolithography processes.

STM measurement scans line by line, and it is sensitive to the height change. So, a smart way is to use straight metal lines with different widths and (or) heights as markers to indicate more information. An example from Paper **IV** is shown in Fig. 3.11, where metal markers have been used to help navigate to the lateral NWs. The metal lines between two arrows in Fig. 3.11a have different width, and the thinnest

metal is extended pointing to the lateral NWs (Fig. 3.11b and c). If the sample is aligned well with the scanning directions, and the coarse movement step in x, y direction is calibrated (usually it is 200-500 nm), we can also do several coarse movement steps at once when moving along the metal markers.

As a general rule, when scanning on large scale (a few hundred nm to μm) in STM, it is safer to use low tunneling current setting and a bias with high magnitude, so that the tip can keep a relatively large distance to the sample surface and avoid unexpected crash. The scanning speed is usually no larger than 200-300 nm/second.

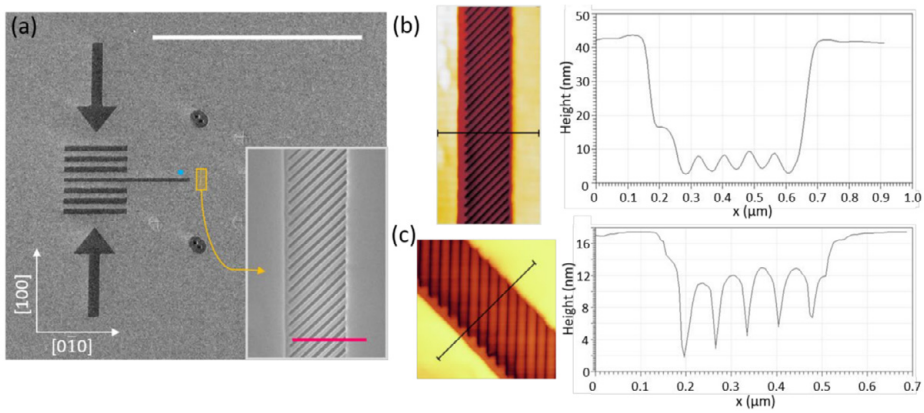

Figure 3.11 (a) SEM image of the sample with navigation marker patterns. The length of the white scale bar is 200 μm. The inset shows the zoomed in image from the yellow rectangle, where the NWs are grown. The length of the pink scale bar is 500 nm. (b) AFM image and its scan profile of the whole device. (c) STM image and its scan profile of the same area with a 40° rotation. (Adapted from the supplementary information of Paper **IV**)

4 Scanning Tunneling Spectroscopy

Scanning Tunneling Spectroscopy (STS) probes the LDOS at varying bias voltage on the surface, with down to sub Å spatial resolution[101,102]. Combining STS and STM, one can obtain topographic and electronic information simultaneously, making it a powerful tool for characterizing surface electronic properties of nanostructures, such as bandgaps[20,103,104], surface defects[105,106] and quantum phenomena[97,107,108] on semiconductor materials. In my experiments, STS is mostly used in determining the surface bandgap and the newly introduced surface states.
This chapter introduces the basic theory of STS and then the data treatment, later the common tip-induced band bending (TIBB) phenomenon will be discussed. In the end, the advantage of STS at low temperature will be reviewed.

4.1 Principles of STS

From Chapter 3, we have obtained the formula of tunneling current in STM with the tip at position $\vec{R}$ as:

$$I \propto \rho_t \int_0^{eV} \rho_{s,loc}\left(\vec{R}, E_F + \varepsilon\right) d\varepsilon \tag{4.1}$$

Practically, current spectroscopy ($I-V$) is done when the tip is kept in a fixed position above the sample surface with feedback loop open, and the tunneling current is recorded as a function of the bias. The tip-sample separation is decided by the pre-set bias and tunneling current. In an ideal STS experiment the tip DOS should be negligible, although this seems not always to be the case. But we assume that the tip condition does not change during the process, which means ρ_t is constant. Thus, the tunneling current is a function of only one variable - bias V. The tunneling current is proportional to the integrated sample surface LDOS from Fermi level to eV, while the LDOS can attribute to either filled or empty states depending on whether the bias is negative or positive. To get the LDOS at a specific energy, which is often more important in studying surface properties, $I-V$ needs to be differentiated, thus we obtain the $dI/dV-V$ spectrum[109].

$$\frac{dI}{dV} \propto \rho_{s,loc}\left(\vec{R}, E_F + \varepsilon\right) \tag{4.2}$$

If the I-V signal is differentiated numerically, it often suffers from high noise levels and thus giving unreliable LDOS spectrum. That is why the dI/dV signal should directly be measured, which can be done experimentally by using a lock-in amplifier and modulating the tunneling bias V .

A lock-in amplifier generates a small sinusoidal modulation dV, superimposed onto the DC tip-sample sweeping voltage, and the tunneling current dI with the same oscillation frequency is detected. The oscillation frequency and amplitude can be set manually, common parameters are 700-1200 Hz for frequency, and 5-100 meV for amplitude depending on the desired signal intensity and resolution. The modulation frequency should be larger than the bandwidth of the STM system to avoid feedback response. Other parameters include the integration time T_c, which needs to be high enough to allow for several cycles of the modulation signal to be included in the integration because more cycles will reduce noise, and the raster time T_{raster} (time measured at each point in the spectra), which needs to be 2–3 times the time constant of the lock-in. In this way, with careful tuning these parameters, a smooth $dI/dV - V$ spectrum with low noise level can be obtained[110].

However, the tunneling current drops significantly to below noise level when approaching the bandgap. To probe the LDOS at the band edge more precisely, the

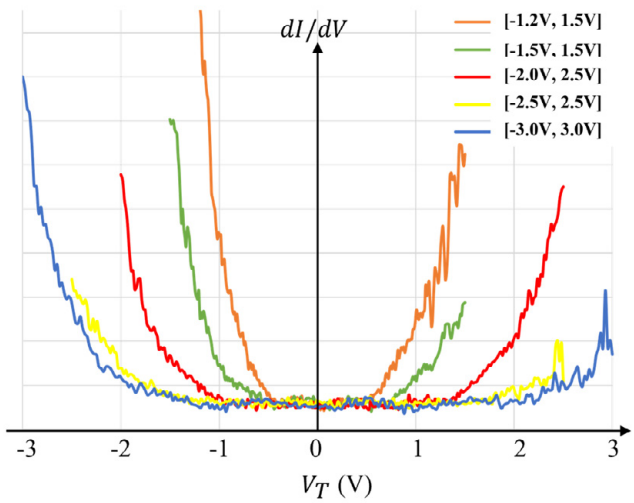

Figure 4.1 STS of Bi-induced honeycomb nanostructures on GaAs (111)B. It is a demonstration of apparent increase in bandgap size when using larger set point voltage (absolute value). The feedback is turned off during the sweep.

tip needs to be brought closer to the sample surface in order to be more sensitive for small LDOS values. Fig. 4.1 shows how different tip-sample distance affects the apparent bandgap detected on the surface. For the pre settings for STS in Fig. 4.1, we use the same I_{set} for all STS, and V_{set} is the most negative bias in the sweeping range. These settings determine the tip-sample distance for each spectrum: Since the tunneling current drops exponentially when the distance increases, to achieve the same I_{set} at a smaller V_{set} (here it means the absolute value of bias), before the feedback loop gets turned off, would require that the tip-sample distance is shorter. From Fig. 4.1 we can see that the bandgap size appears to increase a lot for larger setpoint voltages as the tip is further away from the surface and thus insensitive for the very small LDOS values close to the band onsets.

A commonly used variable gap mode for STS of semiconductors (also known as Feenstra mode) is thus very useful. In this mode, the tip-sample distance changes linearly while sweeping the bias. The distance decreases for lower voltage values, reaching the smallest at zero bias. Typical values of the displacement factor are 1-2 Å/V. The changing distance would bring higher measured LDOS intensity, but the relative intensity ratio at low voltage compared to high voltage also changes. To calibrate the intensity ratio, dI/dV should be normalized by the absolute conductance I/V, since both have the same distance related factor $e^{\frac{-2d}{\hbar}\cdot\sqrt{2m\Phi}}$. However, the conductance I/V is zero within the bandgap for semiconductors, and the normalized value $(dI/dV)/(I/V)$ diverges, thus the conductivity must be broadened as $(dI/dV)/\overline{(I/V)}$, which represents the normalized sample LDOS and is fully independent of the tip-sample distance. The calculation for broadened total conductance $\overline{(I/V)}$ can refer to references[30,79,110,111]. In my experiments, I rarely use Feenstra mode in practise, but the normalization method also applies for STS in constant height mode.

4.2 Surface band bending

Typically, a major aim in STS on semiconductors is to determine the position of the band edges. The LDOS changes linearly close to the band edge, so the most straightforward way is to fit the near edge LDOS curve with a line and extend the line till it reaches zero LDOS, the energy at the cross point is the edge of the bandgap[112]. Some people also use more sophisticated simulations[113]. In my research, however, it is less crucial. So the interested reader can read more in the reference above.

The process of determining the band gap can get more complicated due to band bending effects. The fundamental reason for surface band bending is that the position

of the Fermi level at the surface is different to that in the bulk so that the semiconductor bands need to bend to align the Fermi Level and to reach surface neutrality again[114]. How far the surface band bending can extend into the sample varies a lot with doping level: in highly doped semiconductors it's only a few Å, while in low doped semiconductors it can be 40 nm or more, more examples can be seen in reference[115]. The different Fermi level on the surface can be induced by many factors. Here, we more focus on the Fermi level shift because of additionally available states localized at the surface, for example due to surface reconstructions, defects[116], or the interface to oxides. For example, significant surface DOS has been observed on InAs NWs investigated at 5 K where n-type defects dominated the surface conductivity[112].

Similar band bending happens at semiconductor-metal and semiconductor-insulator interfaces. For the former case, the band bending comes from the charge exchange between the metal and the semiconductor, so that a spatial charge is formed at equilibrium to level up the respective Fermi levels. This is well known as Schottky barrier. It is noteworthy that this concept describes the ideal Schottky barrier, which depends only on intrinsic properties of the two separated systems.

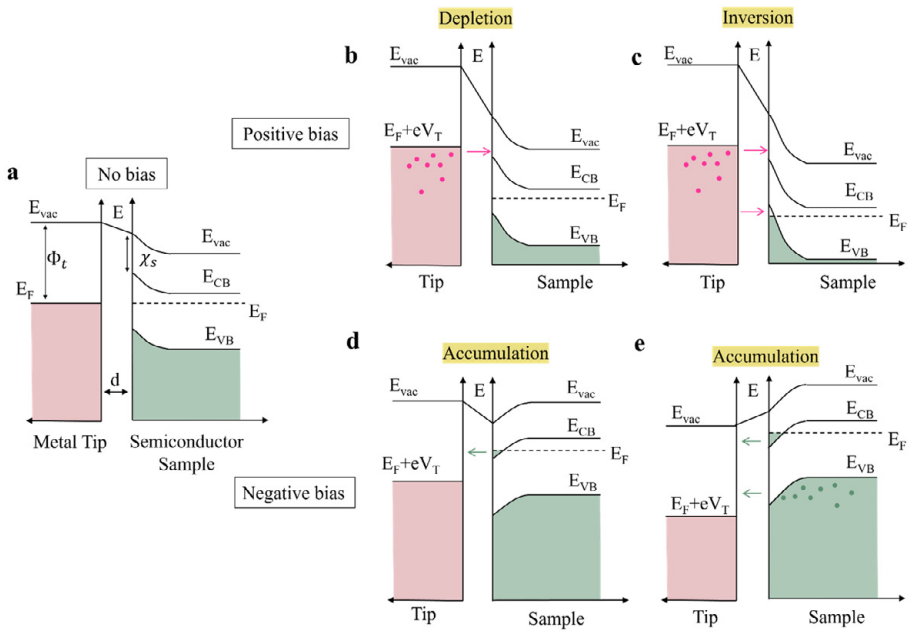

Figure 4.2 Energy diagram for a metallic tip and a n-doped semiconductor illustrating the effect of tip induced band bending on the measured band gap. a) No bias applied. b) The bands in the sample are bent slightly upward at positive bias. (c) Band inversion can happen if the TIBB effect is large. d-e) The bands in the sample are bent slightly downward at negative bias, and electron accumulation happens. In the end, the apparent (measured) band gap would be larger than the actual band gap. Pink and green dots implicit electrons from the tip or the sample, respectively.

In STS, another external factor needs to be considered – the biased metal tip which locates very close to the sample surface and creates a strong electric field which can induce band bending in the sample, known as tip-induced band bending (TIBB). TIBB can sometimes dominate the STS measurement and this effect is always integrated in STS spectra performed with a metal tip on a semiconductor surface. TIBB results in an increase of the apparent band gap of semiconductors.

We can think of TIBB as a metal-insulator-semiconductor (MIS) junction, the energy diagram of scanning on a n-doped semiconductor is shown in Fig. 4.2. The band bending is determined by a lot of factors in this system, such as Fermi energies, metal work function Φ_t, semiconductor electron affinity χ_s[117], semiconductor band gap and its doping level and so on. As we can see in Fig. 4.2a, when no bias is applied, the Fermi level of both the sample and tip are aligned. The small surface band bending on the sample surface is determined by intrinsic surface states out of broken surface dangling bonds and by the doping level. Semiconductors are dielectric by nature and an applied electric field will cause the semiconductor to polarize. When a bias is applied, it will induce band bending in the semiconductor towards the Fermi level of the tip. Thus, the surface of the semiconductor can experience charge carrier depletion or even inversion under positive bias (Fig. 4.2b-c), and charge carrier accumulation at negative bias (Fig. 4.2d-e) in the near surface region. The apparent, or measured, band gap will appear bigger due to the band bending (Fig. 4.3). Calibrations need to be done to correct the TIBB effect, the interested reader can read more in references[112,118], where a flat-band alignment was found between Wz and Zb in InAs[22] and GaAs[19,112] NWs.

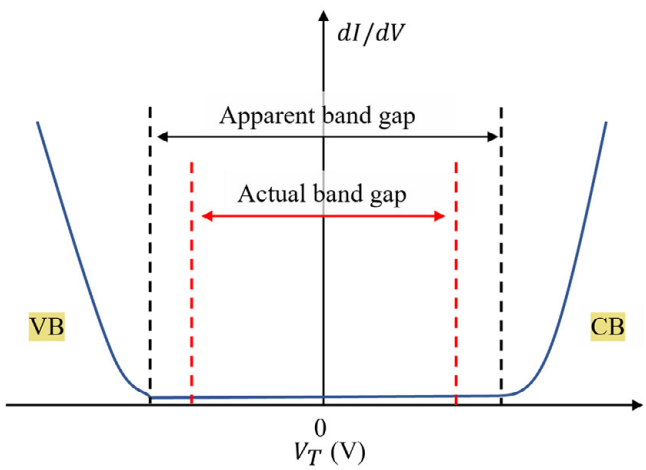

Figure 4.3 STS diagram showing how TIBB influences the determination of the bandgap.

If downward band bending is sufficiently strong and narrow, a quantum well at the surface will be created, and electrons trapped in that well will display quantized discrete states. It is the same for TIBB-induced quantum dots, where the band bending induces confined states[119,120].

In addition, one needs to be aware of quantization effects in small nanowires. NWs with sufficiently large diameters would present no radial quantization effects[121,122]. To realize this, NWs with diameters larger than 40 nm should be used when trying to determine bandgaps, since 40 nm should be significantly larger than the de Broglie wavelength (40 nm for InAs and 24 nm for GaAs[66]) of any charge carriers within the NW. For the NWs with smaller diameters, the measured band gap, including quantization effects, is larger than the bulk band gap of the same material.

4.3 Low temperature STS

All STS data in my experiments are measured at low temperature, at 4K or 10K. For example, with LT-STS along laterally grown InxGa1-xAs NW devices, described in Paper IV, a varying bandgap was observed which is related to variations of the Ga/In concentration. STS at low temperature is in several aspects different to room temperature STS. First, let us talk about the advantages.

LT-STS can offer higher accuracy in the band structure measurement. Temperature influences the energy resolution of STS because there exists more severe thermal broadening of all electronic states at higher temperature. Thus, finer individual states can be detected better at low temperature. Band broadening also depends on the temperature, the broadening is in the range of ca 30 meV at room temperature and drops to 3 meV at around 5 K, according to Gaussian broadening[103,110]. As a result, many exciting phenomena require low temperatures to be studied, such as charge density waves[123,124], QD states[120], as well as Kondo effects and magnetism[125,126]. While in some cases, such as for superconductors, the phenomena only exist at low temperatures[105,127].

Another advantage of LT-STS, which is more practical, is the lower drift at low temperature. We have discussed about it in section 3.3 when introducing LT-STM, and it has the same principle here. STS on a single point usually just takes a few minutes, but when it comes to line STS or 2D grid STS imaging (which will be introduced soon in this section), the measurement time is expected to be a few hours or even days, depending on the pixels and time constant. A big drift would make a quantitative characterization of the spectra difficult, especially when atomic precision is required in location. In a worse case, the tip can crash into the sample surface

because on one hand lateral drift can happen during long STS measurements, on the other hand, feedback loop is kept open during a single spectrum. As a result, it is always suggested to take STS and the STM image simultaneously, so that we can directly observe the drift level. If the used STM software does not have this function, it is advised to obtain an STM image of the area of interest before and after the STS session.

One drawback of low temperature is the possible dopant freeze-out and the resulting low conductivity of the semiconductor, which happens mainly for low-doped semiconductors. In this case, TIBB will be more serious, and a much larger apparent bandgap will be observed. For example, a large tunnel bias had to be used in the STM images due to this effect in Paper **I**. It also can happen that carrier inversion does not even take place, resulting in an "infinite" observed bandgap[128]. Thus, it is recommended to use highly doped semiconductors for LT-STM/S.

Low temperatures can also give rise to other effects such as more easily observed surface states because their standing wave patterns can only be imaged at low temperature, this has been discussed in section 3.2. The atomic pattern of the 2D electron gas on the InAs(111)B surface at temperatures around 10 K is shown in Fig. 3.9c.

Except for point STS, some STM/S software are equipped with the functionality of line STS and(or) 2D STS imaging. Line STS is basically a collection of single STS

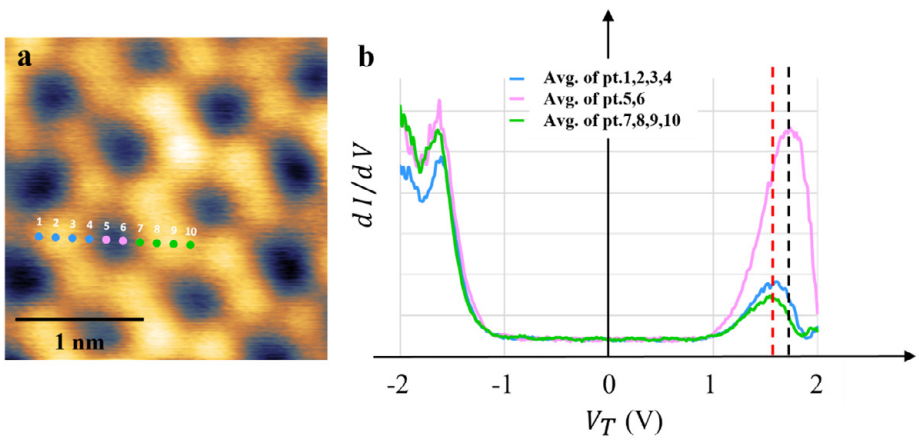

Figure 4.4 LT-STS on a Bi-induced honeycomb structure on GaAs(111)B at 10K (a) LT-STS point spectra are obtained along a line through a honeycomb unit, the individual points 1-10 where STS spectra are acquired are marked in this STM image. (b) shows the comparison between the average STS spectra of points 1,2,3,4 (blue), points 5,6 (pink), and points 7,8,9,10 (green).

points along a line. The position and distance of these point can be determined and STS with the same setting parameters would repeat itself at each point. The advantage of line STS is that the whole set of STS measurement is processed automatically, and no other operation needed. With these evenly distributed STS points, it is easier to compare the change of DOS along the line. One example of LT-STS points through a line is shown in Fig. 4.4.

If we extend the STS points from 1D line to a 2D image, then we can perform 2D STS imaging which shows the DOS in a series of 2D images with varying bias. An ideal 2D STS image needs minimal drift because it usually takes a few hours to days.

5 X-ray Photoelectron Spectroscopy

Studying the semiconductor surface needs comprehensive tools. Although STM/S is powerful for obtaining topographical and local electronical information, this is still not sufficient. A good complimentary technique is X-ray photoelectron spectroscopy (XPS), which is a widely used tool with high surface sensitivity and offers information about the chemical bonding configuration of the topmost few surface atomic layers. XPS has played an important role and has been performed often in my research, especially in studying the Bi incorporation into III-V surfaces in Papers **II** and **III**.
In this chapter I will give an introduction to the theoretical background of XPS, especially synchrotron-based XPS, and illustrate its applications on semiconductor surfaces, using the example of the GaAs:Bi and InAs:Bi system. Methods for XPS data analysis and fitting will be discussed. In the end, an overview of the XPS measurements of those elemental core-levels that are most relevant for my thesis (Ga, As, Bi) will be presented.

5.1 Basic XPS theory

X-rays were firstly discovered by Wilhelm Röntgen in 1895 at the university of Würzburg, Germany, and then the first medical X-ray image of his wife Anna Bertha Ludwig's hand got published, marking a great breakthrough in material studying[129]. Based on this extraordinary discovery, the very first Nobel prize in Physics was granted to Wilhelm Röntgen in 1901. Since then, several more Nobel prizes were awarded to scientist for their significant discoveries related to X-rays, for example, to Charles G. Barkla for the discovery of the characteristic X-rays of elements in 1917, to Max von Laue for the discovery of X-ray diffraction in 1914, and in the next year 1915 to William Henry and William Lawrence Bragg for the famous Bragg's law in crystal structure characterization with X-rays. However, the technique XPS was not realized until Kai Siegbahn, who developed it with monochromatic waves of light and detecting the kinetic energy (K.E.) of the excited electrons. And of course, he was also awarded the Nobel Prize for it in 1981.

The term "X-rays" refers to electromagnetic waves within a certain range of the wavelength spectrum, which is usually from around 0.1 Å to 100 Å, corresponding to photon energies of around 100 eV to 100 keV. In my experiments, I mostly use soft X-rays (roughly between 100 and 1500 eV) as the probe in the interaction with the sample surface, since it is more surface sensitive due the short penetration depth of electrons with kinetic energy in this range. Hard X-rays, on the other hand, are more useful for studying buried interfaces because electrons with higher kinetic energy have longer probing depth.

The photoelectric effect forms the base for XPS, it was described by Albert Einstein in 1905[130], for which the Nobel Prize in physics was granted to him in 1921. The photoelectric effect is a phenomenon of the emission of electrons when electromagnetic radiation with sufficient energy, such as UV light, hits a material. X-ray photoemission is the photoelectric effect phenomenon caused by X-rays. Electrons emitted from the sample in this manner are called photoelectrons.

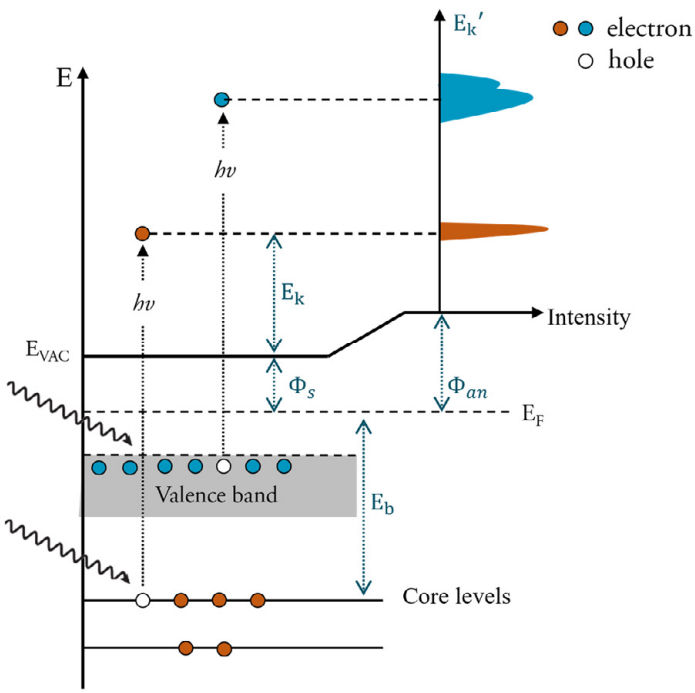

Figure 5.1 Energy diagram in XPS: an electron of a generic core level (orange) with binding energy (E_b) is photoemitted by a photon of energy $h\nu$. The kinetic energy of the photoelectron is E_k, whereas E'_k is the kinetic energy measured by the analyser (right part of the graph). The difference is due to the different work functions of sample (Φ_s) and analyser (Φ_{an}). A photoelectron emitted from the valence band is shown in blue.

XPS is performed by analysing the kinetic energy E_k distribution of the emitted photoelectrons. With the known photon energy of the light hv, the binding energy (B.E.) E_b of the core level electrons can be obtained following the equation:

$$E_b = hv - E_k - \Phi_s \tag{5.1}$$

where h is the Planck constant, v the photon frequency of the X-ray, and Φ_s is the sample work function. Fig. 5.1 shows the energy diagram of the photoelectron process. An X-ray photon with energy hv is absorbed by a core level electron, which overcomes the B.E. E_b and work function Φ_s and gets excited into vacuum, with remaining K.E. E_k. The electrons from the valence band (green area) will get excited as well if the photon energy is higher than the B.E. Since only the valence electrons interact with electrons of neighboring atoms in the periodic lattice, valence electrons have energy bands and the core levels discrete energy states.

The core level B.E. has a characteristic value for a specific core level of a specific element[131]. However, the B.E. of core level photoelectrons is also affected by the particular chemical environment of the element. Thus, XPS offers the information on chemical surface composition and elemental species, as well as their chemical surroundings. Several examples will be given in section 5.4.

Probing depth of XPS

The inelastic mean free path (IMFP) indicates the distance that an electron can move freely without inelastic scattering events. Electron-electron scattering in a solid sample has a high cross section and inelastic scattering between electrons happens often along the way electrons move. Therefore, electrons generally have a very short IMFP and with that a short escape depth from materials. The IMFP of electrons in all materials is mainly related to the K.E. of the electrons. As we can see in Fig. 5.2[132], the minimum IMFP corresponds to a K.E. in the range of 20-100 eV[133], with the minimum IMFP around 5 Å. The escape depth of an electron is roughly around 3 times the IMFP value. This means that electrons cannot escape the sample surface and get detected (at least not without inelastic scattering) except for those emitted from the top few atomic layers of the sample[134,135]. In practise for XPS surface studies, it is suggested to use a suitable photon energy according to the target core level B.E. so that the photoelectrons are in the energy range of a low IMFP. The short IMFP is a strong proof that XPS is a very surface sensitive technique. Moreover, depth profiling can be done by using different K.E. for analyzing electrons from different probing depths.

Therefore, it is understandable why an UHV environment is important for XPS. Just similar to other surface sensitive techniques, for example, STM introduced in

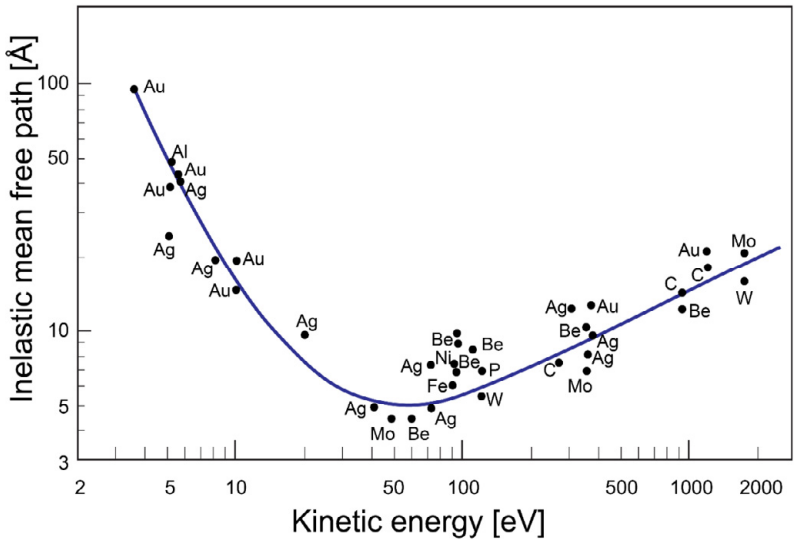

Figure 5.2 IMFP as a function of the kinetic energy, with data points for a number of elements. The behavior is similar for all materials. Adapted from reference [132].

Chapter 3, only UHV can avoid contaminants on the sample surface, such as adsorbates and native oxides which can occur in atmospheric conditions. Another reason is that the detection of photoelectrons becomes difficult in a non-UHV environment, most photoelectron detectors can only operate in UHV range of 10^{-8} mbar or lower.

5.2 Synchrotron radiation X-ray sources

Traditionally, X-rays are provided by an X-ray tube in which electrons are accelerated onto an anode (typically consisting of Al), where they excite X-ray photons with a characteristic energy, often that of the Al Kα emission line at 1486.7 eV. However, this source also has an undesired continuous bremsstrahlung. What is more, the photon flux (or intensity) is very limited, which could lead to a high noise level and thus the measurement is more time consuming. The unchangeable photon energy also limits the flexibility of measuring different core level electrons for different elements while keeping high surface sensitivity.

These limitations can be overcome by using X-rays from synchrotron radiation sources. Synchrotron radiation is produced by electrons in storage rings where electrons are accelerated to a K.E. of a few GeV (3/1.5 GeV for Max IV). Then these high-speed electrons travel through periodic arrays of magnets, which impose regular deviations to the electrons from their trajectory. The radiation released by these oscillations acts as X-rays source. After being properly monochromatized and focused by the beamline optics, a high intensity beam of X-rays with stable energy and focused size is thus obtained. Synchrotron X-ray radiation gives the privilege of higher brilliance[136] as compared to lab sources, which results in a lower noise-to-signal ratio, and of possible tunability of the photon energy, which is very useful to perform surface sensitive analysis with differently targeted core level electrons.

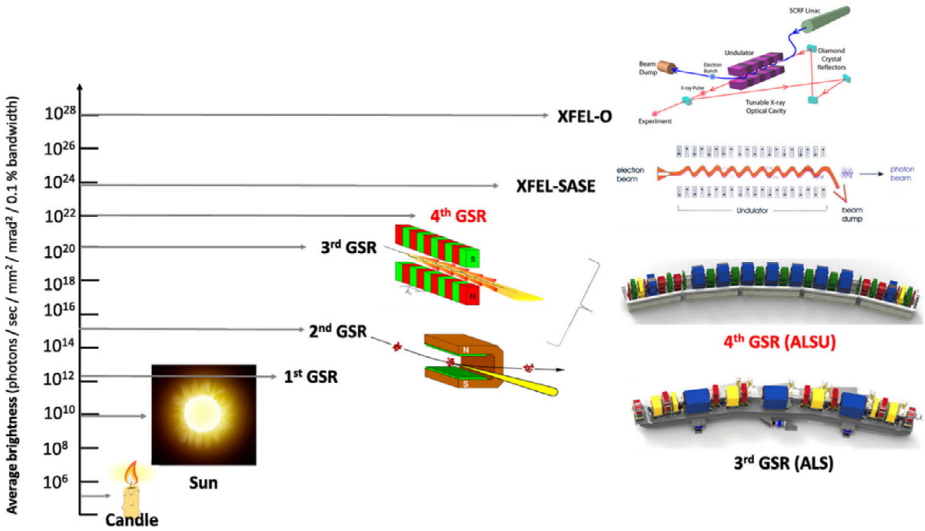

Figure 5.3 The progress of average brightness from candle to the 4th generation synchrotron. Figure adapted from reference [137].

The first synchrotron radiation produced by an accelerator was realized at the Synchrotron Radiation Source (SRS) at Wisconsin, USA, in 1968. That was the first of so-called 1st generation synchrotron sources, equipped with bending magnets for coupling out electromagnetic radiation. After a few decades of development, nowadays the most modern synchrotrons are 4th generation synchrotrons, which adopt undulators and replace simple dipole bending magnets by multibend achromats, enjoying a much higher brilliance and flux[136], as well as better wavelength and beam size tunability[137,138]. The comparison between different synchrotron generations is shown in Fig. 5.3[137]. For more information about synchrotrons, interested readers can refer to references[136,137,139]. In 2016, the MAX IV Laboratory

was inaugurated in Lund, Sweden, as the first 4th generation synchrotron. The MAX IV Laboratory is also the place, among various synchrotron facilities in Europe, where I have performed most of my XPS experiments.

While the synchrotron source provides the X-rays needed for an XPS experiment, the other important component is an electron energy analyser (EEA), to study the intensity distribution of the photoexcited electrons. The EEA is designed to filter the electrons depending on their K.E. As shown by the schematic diagram in Fig 5.4[140], the emitted photoelectrons are collected and focused by an electrostatic lense before they can pass through the entrance slit for the hemispherical EEA. By applying a certain magnetic field, only photoelectrons with the proper K.E. range can travel through the EEA and reach the exit slit. There the photoelectrons are multiplied within a micro channel plate (MCP) and finally recorded by a detector. The EEA detects electrons at a selected energy Epass with an uncertainty ΔE, resulting in the energy range Epass $\pm\Delta E$. The energy uncertainty determines the energy resolution of the XPS spectra. The value of ΔE is proportional to the value of pass energy and it further depends on the acceptance angle and on the width of the entrance and exit slits, while the pass energy depends on the radius of the hemisphere and the applied electric field. A typical resolution of EEA is around 100 meV.

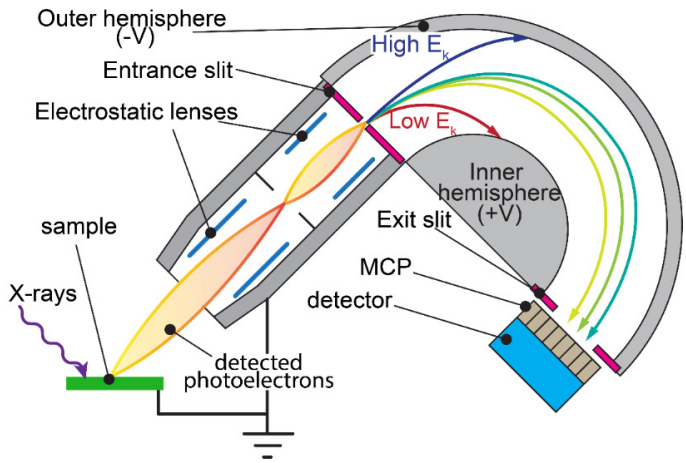

Figure 5.4 Schematic diagram of XPS electron energy analyser (EEA). Adapted from reference [140]

Synchrotron-based XPS studies on III-V semiconductors can be found in several of my papers. The experiments investigating the GaAs NW (Supplementary Information in paper **I**) were conducted at the beamline EscaMicroscopy of the

Elettra synchrotron in Triest, Italy. Here, the sample was scanned through an X-ray beam spot of only 120 nm diameter, at a photon energy of 650 eV. The experiments with GaAs(111)B substrates (paper **II**) were performed at the MatLine beamline of the ASTRID2 synchrotron facility at the Department of Physics and Astronomy at the University of Aarhus. With the help of a multipole wiggler, here the usable photon energy range is from 20 eV to 700 eV. The experiments performed on the InAs substrates (paper **III**) were conducted at several different synchrotrons including the two beamlines mentioned above as well as the MaxPEEM and FlexPES beamlines at MAX IV, Lund, Sweden. The MaxPEEM is supplied with soft X-ray, while X-rays in the energy range of 40-1500 eV are used for FlexPES.

5.3 XPS analysis and spectra fitting

Before I go through the XPS data analysis, let me give a brief overview of the electron configurations in an atom in the context relevant to XPS. These two types of electrons are located at the nuclei and are in their ground state – there can also exist excited electrons in the conduction band, or free electrons.

Core electrons are located in the inner shells and are closely bound to the atom nucleus, while valence electrons are in the outermost shell and are more loosely bound. The B.E. of valence electrons is in the range of a few eV, and they are often used to identify the valence band structure.

Although not participating in chemical bonds, the B.E. of the core level electrons is still affected by the chemical surrounding and the overall charge of the atom. The change in B.E. generated in this way is called chemical shift. Therefore, an electron from an As-O bond has a different B.E. than an electron from an As-Ga bond. Due to this effect we can, for example, determine if the surface oxide has been removed from our GaAs surface or not. More examples will be given in section 5.4.

Now let us look how we name the photoelectrons from different core levels. Core electrons fill up the atomic orbitals in a certain order (Fig. 5.5), and each core electron can be described by a set of quantum numbers: Energy core level number n, angular momentum l, orbital number m and the total angular momentum j. n, l and m are all integers, where l has a range from 0 to $n-1$ and m from $-l$ to l. The first few quantum numbers of l are historically described as s, p, d, f. When considering the spin of electrons, the magnetic field arising from the electron spin will couple into the angular momentum l. Since electrons can only either spin up or spin down, the total angular momentum j is defined as $j = |l \pm s|$, where $s = \pm 1/2$. Thus, when $l > 0$,

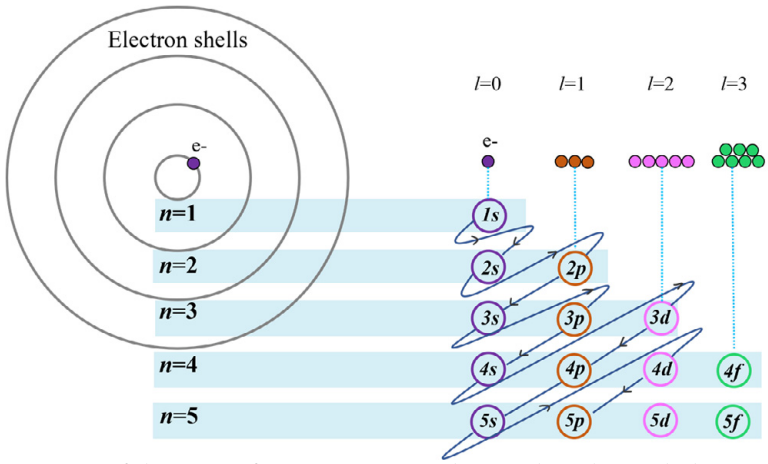

Figure 5.5 Diagram of electron configuration sequence, showing the order in which atomic orbitals are filled. Each circle represents one orbital, *n* is the core shell orbital number, *l* is the orbital angular momentum. Each *s* orbital can contain a maximum of 2 electrons (one spin up, one spin down), while 6 for *p*, 10 for *d*, and 14 for *f*.

the energy level will be split into two different energy levels, that is the so-called *spin-orbit splitting*. What is more, the two split core level electrons will have different B.E. We usually call this kind of two peaks in XPS as *doublets* and note that the split energy between the two peaks is fixed for a specific doublet.

For example, Bi $5d_{3/2}$ and Bi $5d_{5/2}$ mean two types of core photoelectrons coming from 5th energy core level, with angular momentum of 2, but with 2 different total angular momentum 3/2 or 5/2 depending on the spin orientation.

To analyse XPS data, I usually perform a two steps processes. First, Fermi level calibration. This step is usually done by determining the work function Φ with a known core level. Secondly, XPS decomposition and fitting of different core level spectra, so that we can determine the chemical shifts of core levels as well as compare their intensity changes.

From equation 5.1, we know that the function Φ is a value which needs to be determined before we can obtain the absolute B.E. The work function Φ is defined as the amount of energy it takes to excite an electron from the Fermi level E_F to the level E_{vac}. However, the work function of both the analyser and the sample are not known precisely. For a metal sample, the clear Fermi edge, which shows a sharp cut of photoelectron intensity, can be used as reference point. However, for a semiconductor, the Fermi level is located within the bandgap. In this case, we measure the binding energy of a well-known core-level from a different material, such as Au *4f*, and use its literature value for calibration.

For the data analyse in my research, much more effort has been put in determining the relative shift of binding energies of the same core level but different chemical states. In order to distinguish the overlapping contribution from different components, careful peak fitting needs to be performed. Often the peaks are assumed to be a convolution of a Gaussian part and a Lorentzian part, commonly known as a Voigt function. XPS fitting contains a series of data fitting processes, here I list a few important parameters:

Background subtraction. The background photoelectrons mostly come from secondary electrons. Usually, I use a polynomial function of different order or linear subtraction.

Peak intensity is important because it is strongly dependent on the amount of material at the surface, so that the relative concentration of interested species can be obtained. Note that the intensity also depends on the scattering cross section and losses due to inelastic scattering, that means the photoelectrons from materials at deeper position have smaller intensity, compared to the surface materials.

Lorentzian width, representing a core hole lifetime. It should be same for the same core level, regardless of the chemical environment.

Gaussian width, representing the instrumental resolution or uncertainties, as well as lattice vibrations, can vary on individual components of the same core level. Usually, it is smaller for higher quality crystalline material, and larger for amorphous materials.

Spin orbit splitting energy is a fixed value for photoelectrons from a known core level. It presents the energy difference of photoelectrons from the same core level orbital, but with different total angular momentum.

Spin orbit split peak weight ratio. It is also a fixed number, indicating the intensity ratio of core level doublets at the same core level orbital but with different total angular momentum. For example, theoretically the ratio is 0.5 for *2p*, 0.66667 for *3d* and 0.75 for *4f*. In practise, the value can change within a reasonable range, due to the influence of background or neighboring core level peaks.

Sweep numbers. All spectra should be normalized by the number of sweeps. Multiple sweeps can lower the noise level of spectra.

Since the XPS fitting is not the main content of this thesis, not all details will be discussed here. Interested readers can refer to another thesis in our division[141].

5.4 XPS of selected elements

Here, I give a few examples on the XPS study of several important elements in my research, with a focus on how the chemical shifts are introduced from different bonding configurations.

5.4.1 XPS of Ga and As

A GaAs(111)B substrate that has been exposed to air is covered with a thin layer of native oxide on the surface, where a component with Ga-O bonding configurations exists. The comparison of the Ga 3d core level before and after oxides removal (with the aid of atomic hydrogen, which will be introduced in Chapter 6) is shown in Fig. 5.6a. Since XPS is very surface sensitive, with the thin oxide layer, Ga-O bonds dominate the intensity of the XPS spectrum and core level electrons from Ga-As bonds can hardly be observed. On the oxide-free surface, on the other hand, the Ga-As peak is much more pronounced. Fig. 5.6b demonstrates an even minor chemical shift (within 0.1 eV) of Ga-As bonds, which are influenced by the surface modification by Bi atoms. For example, the black curve shifts to lower B.E. when Bi atoms get incorporated and react with As atoms forming Bi-As bonds, and later on the purple curve shifts to higher B.E. when more Bi atoms are deposited, forming metallic Bi with Bi-Bi bonds. This is due to the change of the chemical environment

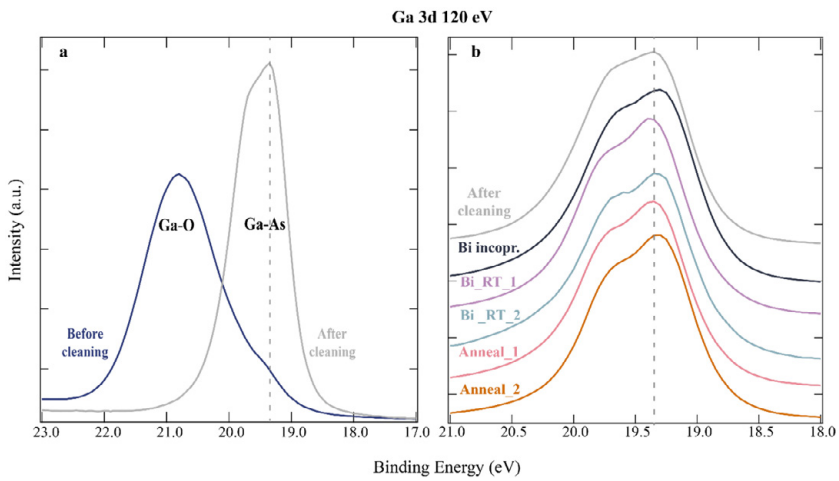

Figure 5.6 XPS Ga 3d core level spectra on GaAs(111)B: (a) The comparison of before and after H* cleaning. This is an example of the successful removal of Ga oxides. (b) Chemical shifts have been observed for Ga 3d during surface treatment with Bi atoms. This figure is adapted from the supplementary information of Paper **II**. Photon energy is 120 eV for all XPS spectra.

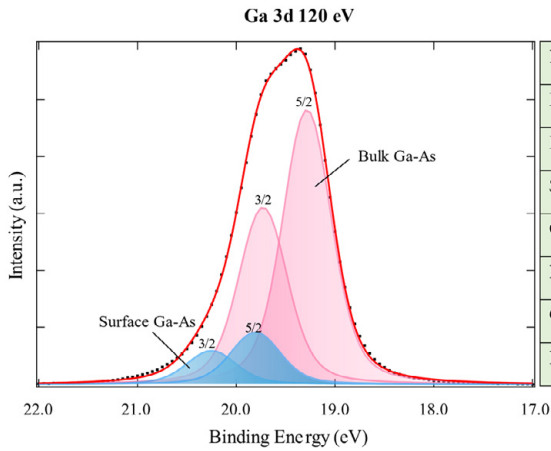

Background	4th order polynomial
Lorentzian (eV)	0.18±0
Ratio	0.64±0.02
Spin-orbit splitting (eV)	0.451±0.005
Gaussian_bulk (eV)	0.46±0.01
Position_bulk (eV)	19.268±0.007
Gaussian_surface (eV)	0.60±0.08
Position_surface (eV)	19.72±0.06

Figure 5.7 XPS Ga *3d* core level spectrum on an oxide free GaAs(111)B surface, the component decomposition and curve fitting of the spectra are indicated as pink (bulk Ga-As) and blue (surface Ga-As). 3/2 and 5/2 are the total angular momentum numbers for the corresponding XPS peak. Photon energy is 120 eV for all XPS spectra. Fitting parameters are shown in the table.

of the Ga atoms, or the change of the ratio between different components (like the surface and bulk components). For more details one can refer to Paper **II**.

XPS decomposition and curve fitting of Ga *3d* is shown in Fig. 5.7. Pink and blue curves present the doublets of Ga $3d_{3/2}$ and Ga $3d_{5/2}$ peaks from the GaAs bulk and GaAs surface, respectively, which has a difference of 0.45 eV in B.E. due to a surface reconstruction consisting of mainly As atoms, which influences the bonding environment even of the Ga atoms. All XPS fittings in this thesis are processed with the IGOR Pro software.

The situation is similar for As *3d*, where core electrons from As-O and As-Ga are of different B.E. (Fig. 5.8a), and a small chemical shift also exists for As *3d* under different surface treatment with Bi atoms (Fig. 5.8b). Component fitting for As 3d is not shown here, nevertheless, the As $3d_{3/2}$ and As $3d_{5/2}$ peaks are marked in the spectra. The surface component of As *3d* should however have a lower B.E. compared to the bulk component.

Analyzing the chemical states of Ga and As is a very helpful way in determining surface cleanliness (existence or absence of oxides residuals), and the formation of new chemical bonds with Ga or As atoms.

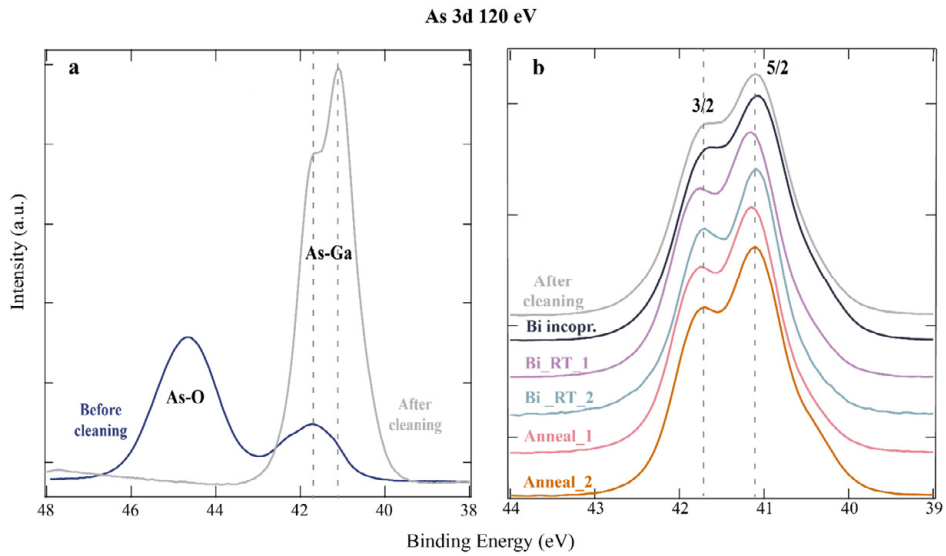

Figure 5.8 XPS As *3d* core level spectra on GaAs(111)B: (a) The comparison of before and after H* cleaning. (b) Chemical shifts have been observed for As *3d* during surface treatment with Bi atoms. This figure is adapted from the supplementary information of Paper **II**. Photon energy is 120 eV for all XPS spectra.

5.4.2 XPS of Bi

Investigating the bonding configuration and chemical state of Bi atoms on III-V surfaces is one of the main tasks in my research. For example, Paper **II** and Paper **III** have a major focus on it, with the analysis of Bi *4f* or Bi *5d* core level electrons. The B.E. of Bi atoms will vary slightly depending on their bonding partners. In my study, I mostly focus on possible III-Bi, V-Bi, and metallic Bi-Bi bonds, and sometimes there exists more than one type of Bi compounds on the surface.

In the Bi 5d core level spectrum shown in Fig. 5.9, three components can be seen. Bi-Bi bonds come from the metallic Bi and Bi-As bonds are formed after Bi deposition onto GaAs(111)B substrates. There is around 0.7 eV difference in the B.E. of the electrons from these two bonds. The component Bi-As interf. indicates the special chemical states of the Bi atoms at the interfaces between the substrate and metallic Bi layer. Fitting specifications are shown in the table on the right of Fig. 5.9.

The XPS spectrum of Bi 5d shown here is one of a set of XPS measurements obtained during the Bi deposition and other subsequent treatment on a GaAs(111)B surface, and a nicely ordered honeycomb structure is formed in this process. More

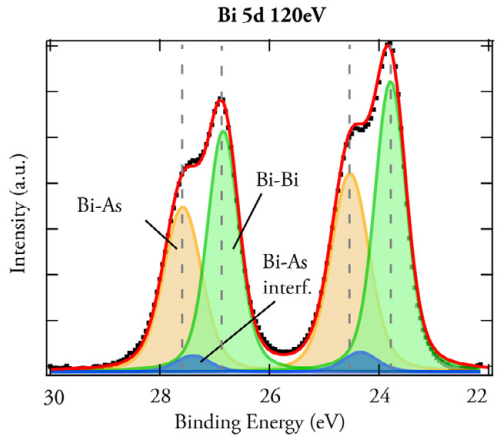

Background	4th order polynomial
Lorentzian (eV)	0.22±0
Ratio	0.83
Spin-orbit splitting (eV)	3.05
Gaussian (Bi-As) (eV)	0.70
Position_Bi-As (eV)	24.53
Gaussian (Bi-Bi) (eV)	0.55
Position_Bi-Bi (eV)	23.79
Gaussian (Bi-As interf.) (eV)	0.60
Position_Bi-As interf.(eV)	24.34

Figure 5.9 Bi *5d* core level XPS spectra of GaAs(111)B surface after Bi deposition, including the component decomposition and curve fitting of the spectra. Fitting parameters are shown in the table on the right ride. Photon energy is 120 eV.

STM images of the honeycomb structure can be found In Fig. 3.4 and Fig. 3.10. For the full set of XPS spectra and more detailed discussion, I refer to Chapter 6.

5.4.3 Valence band

Strictly speaking, the electronic valence band structure is not directly determined by any specific elements, but a result of the overall bonding environment and surface conditions. By examining the valence band structure, one can obtain important information about how the surface conductivity and surface band gap vary during different surface treatments. This is realized by monitoring the photoelectron density near the Fermi level in XPS spectra, an important criterium is the B.E. at which we can see the onset of the XPS signal, as this energy marks the valence band edge and its distance to the Fermi level, which is located at 0 eV B.E.. An XPS spectrum of the valence band region of the GaAs(111)B surface is shown in Fig. 5.10. Bi deposition and other surface treatment steps are shown in the legend. We can see that after step "Bi_RT_2" the valence band intensity slightly decreases but the valence band covers the entire energy region from 0 to at least 3 eV B.E., indicating a metallic surface. On the other hand, after step "Anneal_2", the valence band edge shifts to higher B.E. and the XPS curve almost follows the same trace as for the clean GaAs(111)B surface, showing an offset between the valence band edge and the Fermi level. By this, we can conclude that the metallic surface states mostly come from metallic Bi, instead of

incorporated Bi atoms which bond to As. For a more detailed explanation, I again refer to Chapter 6 as well as paper **II**.

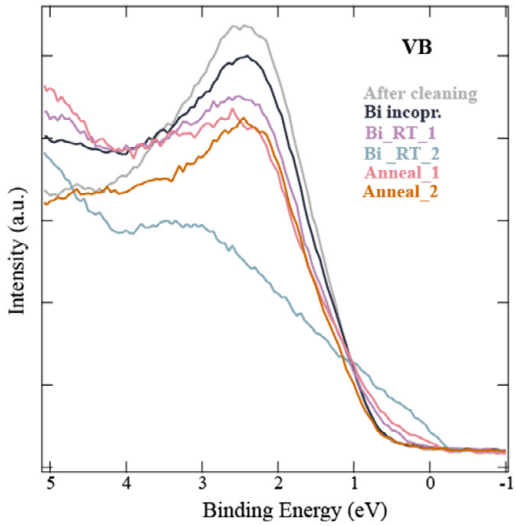

Figure 5.10 Valence band region in XPS spectrum on GaAs(111)B surface upon different Bi deposition and surface treatments. Figure adapted from the supplementary information of Paper **II**.

5.5 Scanning Photoelectron Microscopy

XPS shows the average photoelectron intensity from the surface area illuminated by the incident X-rays. If one wants to add spatial resolution to XPS studies, one has to make the spot size small and add functionality for scanning the sample, then a 2D photoelectron image can be obtained with the probe of X-rays. Usually this is achieved by a special sample stage which is able to scan the sample in a 2D plane and in a controllable manner. Such a technique is called Scanning Photoelectron Microscopy (SPEM), which has been demonstrated to be a cutting-edge X-ray technique[142,143].

The small beam size and high lateral resolution (down to a few tens of nm) in SPEM is especially helpful when studying nanostructures if one would like to distinguish between individual NWs, image along NW heterostructures, or just want to have signal from the NW and not from the substrate. Moreover, high photon flux is necessary in order to gain enough photoelectron intensity. So far, SPEM can only be found in synchrotrons due to its specific requirement on X-ray intensity and brilliance. SPEM offers spatial resolution at the hundred nm scale together with as

high energy resolution, this means that one can take maps sensitive to a specific element.

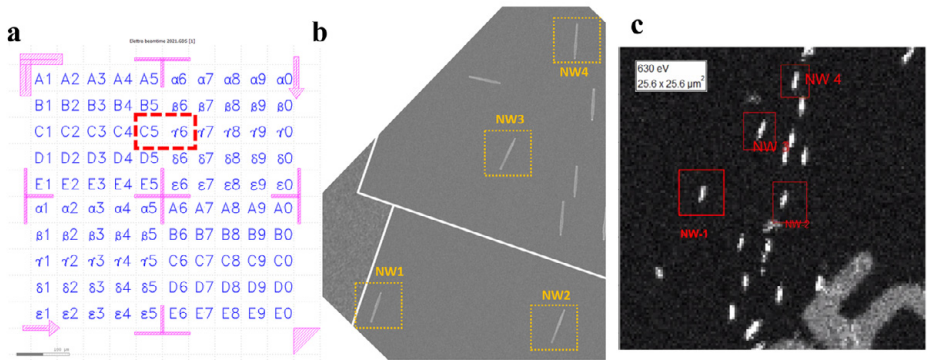

Figure 5.11 (a) The pattern of a chip with metal markers which are designed for navigating between individual NWs. (b) SEM map, stitched together from 3 SEM images of NWs lying near the C5-γ6 region as marked in (a). (c) A 2D SPEM image of the deposited NWs in the same area as (b). NWs are marked with rectangles. The marker "C5" can be recognized at the bottom of the SPEM image. Photon energy is 650 eV and kinetic energy is set to be 630 eV.

The SPEM setup at the ESCAmicroscopy beamline of the Elettra synchrotron[144], which was used in my work for the NW studies of paper **I**, has a beam spot down to 120 nm. To better navigate to the target NWs, we usually utilize a chip with metal markers (Fig. 5.11a), and deposit mechanically transferred NWs on it. With pre-recorded SEM images (Fig. 5.11b) as navigation, NWs can be found rather efficiently. A 2D SPEM image of the deposited NWs is shown in Fig. 5.11c. By comparing the position of the marked NW1- NW4, the distribution of NWs matches well between the SPEM image and the SEM image. We can easily move to the next targeted NW to investigate.

With the superior small spot size, SPEM can be used to image one single NW (Fig. 5.11). 2D SPEM maps of Bi *4f* and Ga *3d* core-levels are shown in Fig. 5.11c and 5.11d, respectively. The color scale corresponds to the distribution of the Bi and Ga signal in 2D. In both images, the distribution of the Bi and Ga signal is in good agreement with the shape of the NW in the SEM image of Fig.5.12a.

The SPEM image of Bi *4f* indicates that the Bi atoms are rather evenly distributed over the entire NW, and that the Bi *4f* signal comes almost completely from the NW instead of the Si substrate. One explanation is that the Bi atoms that have been evaporated onto the Si substrate simultaneously have desorbed again. For the SPEM image of Ga *3d*, the intensity seems to be a bit stronger on the top part of the NW.

This can be due to the slightly larger diameter of the NW at the top (closer to the Au particle).

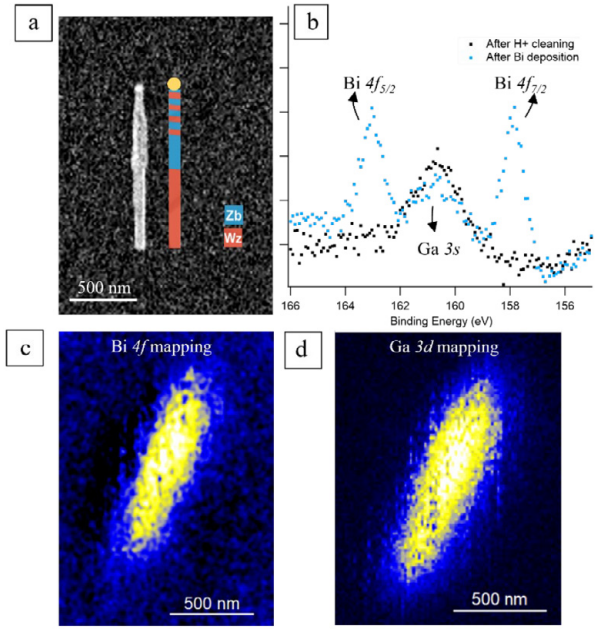

Figure 5.12 X-ray photoelectron spectroscopy (XPS) study of a single NW. (a) shows an SEM image of a typical GaAs NW. (b) presents XPS Bi *4f* core level spectra before and after Bi incorporation, measured in the middle of the same NW as shown in a. (c) and (d) show 2D SPEM images of the same NW studied in (a) and (b), illustrating the distribution of (c) Bi 4f and (d) Ga 3d signals. Photon energy is 650eV for (b-d). Figure adapted from the supplementary information of Paper **I**.

6 Nanostructure surface modification

This chapter mainly deals with the modification of nanostructure surfaces on III-V semiconductors that is involved in my study. From now on, we need to switch the thinking from ideal, perfect crystal surfaces to non-perfect (or more realistic) surfaces that are observed in experiments. Real crystal facets contain many interesting features, such as atomic steps, defects, surface reconstructions, and incorporation of foreign atom species. The versatile possibilities make surface modification very complex, but very interesting as well.

Just like how my experiment usually starts, this chapter starts with the removal of native oxides from III-V semiconductor surfaces (section 6.1). Later on, surface modifications without foreign species will be introduced (section 6.2), where atomic rearrangements on the surface are the result of surface energy minimization. Lastly, the surface incorporation of foreign species (Bi atoms) will be discussed (section 6.3), with a focus on different crystal planes of GaAs. Crystal facets on both GaAs wafers and GaAs NWs will be discussed. Novel and ordered surface nanostructures found in the GaAs:Bi system will be presented. The mechanisms of nanostructure modifications will be discussed as well.

6.1 Removal of native oxides

Native oxides are formed on the surface of III-V semiconductors when these are exposed to ambient air. The oxides consist of both group III- and V-oxides, resulting in an amorphous oxide layer. Nearly all my experiments start with native oxides removal, so that the clean surfaces of III-V semiconductors and the formation and modification of nanostructures on these surfaces can be investigated at the atomic scale.

Among several options for surface oxides removal, such as wet chemistry treatments[145] (e.g. HF etching), ion sputtering[146-148], and H-plasma or atomic hydrogen[146,149,150], the atomic hydrogen treatment is the most suitable method in my study and has been used in all my papers listed in this thesis. Atomic hydrogen

treatment is preferred because it includes a mild, but efficient cleaning process and causes least surface defects on III-V substrate (e.g. GaAs)[19,21,43]. Other methods, such as ion sputtering, are more often applied on metals or when a thick oxide layer needs to be removed, and usually a following thermal annealing is necessary in order to decrease the surface roughness and the number of defects which, however, does not work well for III-V surfaces. For oxides removal on III-V semiconductors, simple annealing of the sample does not work, because this would require temperatures which are above the thermal dissociation of III-V alloys.

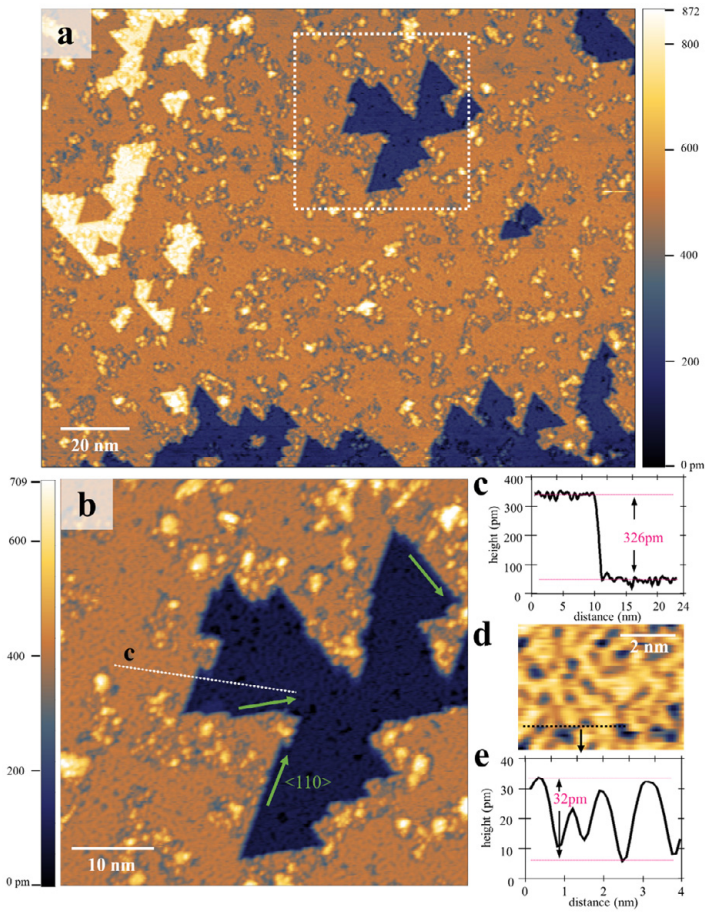

Figure 6.1 LT-STM images of an oxide-free GaAs(111)B substrate, after cleaning with atomic hydrogen. (a) Overview STM image. (b) zooms into the rectangular area marked with white dashed lines in (a). The green arrows show that the terrace edges are along <110> directions. The height profile crossing a terrace edge is shown in (c), marked as the white dashed line in (b). (d) shows the irregular atomic pattern on the GaAs(111)B substrate at around 10K. (e) presents the height profile along the black dashed line marked in (d). Figure adapted from the supplementary information of Paper **II**.

Surface native oxides removal by atomic hydrogen treatment is done in UHV environment by annealing the substrate under a flux of atomic hydrogen (chamber pressure at around 2×10^{-6} mbar). Atomic hydrogen (also known as hydrogen radicals) is produced through thermal cracking of hydrogen molecules by a tungsten filament heated to ca. 1700 °C. The hydrogen radicals are extremely reactive with the native oxides on the surface, resulting in volatile products which can desorb at lower temperature[149]. The interaction between the sample and the hydrogen is limited to the sample surface because the hydrogen radicals have a very low K.E. The oxides removal efficiency is influenced by the temperature of the hydrogen cracker, usually longer processing time is needed if the hydrogen cracker is at lower temperature (due to the lower cracking efficiency).

Normally, the annealing temperature upon atomic hydrogen treatment is ca. 500 °C for GaAs and ca. 400 °C for InAs. After cleaning, it is suggested to keep the sample at high temperature for a few minutes to desorb any redundant hydrogen and surface contaminates. Conventionally, we often describe the cleaning process as "hydrogen cleaning" process. Concluded from experimental results, it takes at least 40 mins until the native oxide on GaAs substrate is completely removed, with the condition that the sample is about 20 cm away from the hydrogen flux source. While for InAs substrate, the oxide is easier to be removed and it usually takes around 30 mins.

LT-STM (at ca. 10K) images of an oxide-free GaAs(111)B substrate after cleaning with atomic hydrogen, exposing the As-terminated surface, are shown in Fig. 6.1. The terrace edges, as indicated in Fig. 6.1b by green arrows, follow <110> directions, since natural cleavage planes of Zincblende crystals are {110} planes. These edges and the resulting triangular-like shaped terraces are strong indications that the surface is clean (or oxide-free). Most of the terrace edges are one atomic monolayer high, a height profile is shown in Fig. 6.1c, presenting terraces with monolayer height of around 326 pm. Note that one monolayer contains a layer of Ga atoms and a layer of As atoms. Similar to the LT-STM image of InAs(111)B in Fig. 3.9c, the GaAs(111)B surface also presents atomic-scale irregular patterns (a corresponding STM image is shown in Fig. 6.1d) due to a 2DEG on the surface at low temperature.

XPS is very useful for verifying the absence of oxides and other surface contamination and it is very often utilized in my experiments. More information about XPS can be found in Chapter 5.

6.2 Ideal surfaces vs. defects and reconstructions

In Chapter 2 we have discussed different types of crystal planes which have ideally ordered atomic patterns. However, crystal surfaces are usually non-perfect. Atomic defects, vacancies, adatoms, and even reconstructions can often be observed on crystal surfaces.

Cleaving a bulk crystal in vacuum along certain orientation can generate a flat crystal plane surface, this approach also ensures that no contaminants from the atmosphere will be introduced. However, most often the crystal cleaves along the energetically preferred cleavage planes, such as the non-polar {110} planes, while surfaces in other crystal plane orientations tend to undergo surface reconstructions.

Commercial III-V semiconductor wafers are usually formed by the Czochralski method followed by several steps of polishing processes. In this way, an atomically flat crystalline surface can be produced, known as "epi-ready" surface. Nevertheless, the native oxides cannot be avoided due to the exposure to the ambient. After oxides removal, the surface roughness is usually at a scale of a few nanometers, where the varying topography mostly comes from terrace steps at monolayer height. For example, the unreconstructed (1×1) InAs(111) surface at atomic scale is presented in Fig. 6.2. The terrace edges are along <110> directions. The small defects in triangular shape, which consist of only a few missing atoms, follow the same orientation as the terrace edges.

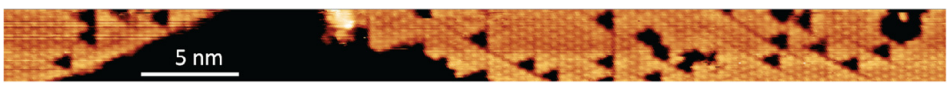

Figure 6.2 STM image of an oxide-free InAs(111)B substrate at room temperature. Each single dot in this filled state image depicts one As atom. The non-reconstructed surface shows the ordered (111) plane, with a distance of 4.5 Å between two nearest As atoms. Image courtesy of Sandra Benter.

However, due to the broken chemical bonds on a surface, the crystal atomic structure on the surface is usually less stable than that in bulk form due to the higher surface energy. The surface energy can be understood as positively correlated to the density of dangling bonds (broken bonds) on the surface, i.e., more closely packed surfaces which have fewer dangling bonds tend to have lower surface energies. To lower down the surface energy, atoms on surfaces often undergo certain surface rearrangements, such as relaxation, surface reconstruction, segregation, and adsorption of foreign species (if available) onto the surface. The new surface arrangements can either happen instantaneously (in a self-driven fashion), or when

the surface receives the activation energy necessary for a rearrangement, e.g. through thermal annealing.

Often the rearrangement of surface atoms ends up in a new equilibrium state with another type of periodic pattern on the surface, known as surface reconstruction. For the definition of the Woods Notation for naming surface reconstructions I refer readers to reference[151]. Some well-known examples of surface reconstructions are the Si(111)-(7×7) dimer-adatom-stacking fault reconstruction[152,153] and the herringbone structure on the Au(111) surface[154]. For GaAs, a (2x2) surface reconstruction has often been observed on GaAs(111)A[155] and GaAs(111)B[156], with either a Ga-vacancy structure or As trimers adsorbed on the outmost As layer, respectively. The non-polar GaAs Zb {110} (or Wz $\{11\bar{2}0\}$) surface, which is parallel to the natural cleavage plane, usually presents an unreconstructed surface, even though this surface undergoes relaxation of the outermost atoms. Finally, for GaAs(001), (2×4) or c(2×8) reconstructions on the As-rich surface[157] are two of the most often observed surface reconstructions. More examples of surface reconstructions can be found in reference[151].

Still, more complex (or unexpected) surface reconstructions can happen. In my study, some ringlike patterns with a diameter of around 1 nm (Fig. 6.3) were observed by STM on a GaAs(111)B surface after a few hours of thermal annealing followed by hydrogen cleaning. These atomic rings are likely to be the $\sqrt{19}\times\sqrt{19}$ R23.4° ("R" means rotation) reconstruction which has been observed on a Ga-rich GaAs(111)B surface. The atomic model and more information about this type of reconstruction can be found in references [158,159].

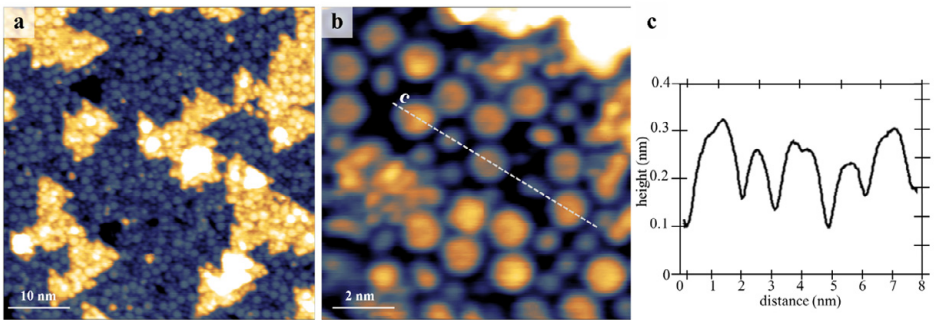

Figure 6.3 STM images of ringlike nanostructures on GaAs(111)B. (a) overview and (b) zoomed-in atomic-scale STM images. (c) A height profile along the white dashed line shown in (b). For (a) V_T = -6 V, I_T = 50 pA, (b) V_T = -5.5 V, I_T = 100 pA

All the surface morphologies we discuss in this section do not consider the case of surface physisorption, i.e. atoms with only weak bonds (such as Van der Waals) to the

surface. Instead, we are more interested in atoms that form chemical (covalent, metallic, ionic) bonds with the surface atoms. This kind of surface chemisorption is more stable and usually is a more important factor in altering surface band structure and the electronic properties. To distinguish physisorbed atoms from chemisorbed atoms that have formed chemical bonds to atoms in the substrate, the XPS technique is often adopted.

6.3 Bi incorporation in III-V surfaces

Bi incorporation in III-V surfaces is an important part of my PhD study, including the modification of Bi-induced nanostructures, the determination of chemical bonding configurations between Bi and conventional III-V materials (including Al, Ga, and In as group-III and P, As, and Sb as group-V elements), and the electronic properties of surfaces in the III-V:Bi material. In this section, I aim to summarize a few key results of my studies on GaAs:Bi surfaces. In the end, some related studies of InAs:Bi that I have been involved in will be shortly discussed.

6.3.1 Introduction

Bi-containing III-V semiconductor compounds have gained a lot of attention recently because of their exceptional electronic properties, for example, the strong spin-orbit coupling[34,36] and predicted non-trivial topological behavior[38]. Band inversion is also predicted for III-V:Bi materials, however, only for high Bi content[39]. All these novel properties can be used in many applications, such as bandgap engineering[35,37] and quantum information technology. For now, the main challenge lies in the synthesis process and well-controlled growth[160] due to the high lattice mismatch between III-V and III-Bi materials.

Instead of heavily doping Bi into III-V material during growth, an alternative way is to deposit Bi on the clean III-V semiconductor surface. So far, most of the reported Bi deposited III-V semiconductors surfaces have overlayers of pure Bi[161], or Bi-terminated reconstructions, for example, on InAs[162,163] and GaAs[164-169]. Nevertheless, these Bi-induced surface structures have not yet shown the clear novel electronic properties mentioned above. Moreover, the Bi-terminated reconstructions are often not largely ordered structures, but only limited to local areas. The mechanism of how Bi atoms interact with a III-As surface is very interesting to me, this includes how the topography changes, and which chemical reactions occur when depositing Bi on the surface, as well as how to achieve high Bi content on the surface of III-V:Bi materials.

The chemical interaction between Bi atoms and III-V surfaces has been investigated as well. Bi atoms are found to be able to form chemical bonds with either group-III or group-V atoms, or both at the same time, as for example observed by McGinley et al. for the Ga-terminated (111)A[168] and the As-terminated (111)B[170] surfaces. Among these bonding configurations, Ga-Bi is probably the most interesting bond, since GaBi has been predicted to show band inversion and topological behavior[39,40]. However, GaBi has been considered as thermodynamically unstable[35,171,172].

In section 6.3.2, I will show the obtained stable, large-scale well-ordered GaAs:Bi structure involving the unique Bi-introduced electronic states on GaAs(111)B, and later in section 6.3.3, I will present the observed GaBi islands on the {11$\bar{2}$0} surfaces of wurtzite GaAs.

6.3.2 Bi incorporation in GaAs(111)B surfaces

Depositing Bi on the polar GaAs(111)B surface does not necessarily result in a nicely ordered surface. For example, when depositing at room temperature, only metallic Bi

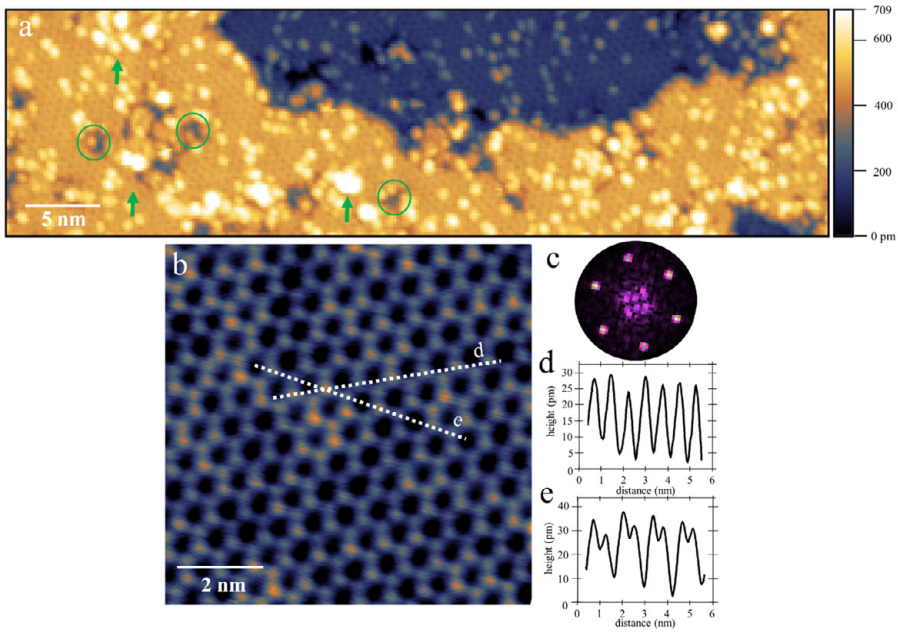

Figure 6.4 Honeycomb structure upon Bi deposition on GaAs(111)B at 250°C (a) Overview STM image and (b) atomically-resolved STM image of the honeycomb structure. (c) Fast Fourier transform (FFT) image of image (b). (d) and (e) Height profiles of line scans across the honeycomb structure as indicated in (b) by white lines. in (b). Adapted from paper **II**.

clusters will be resulting. In my experiments, the as-cleaned GaAs(111)B substrate is heated up to 250°C during Bi deposition, and the Bi coverage is controlled to be less than one monolayer.

The resulting full layer of uniform honeycomb-like networks is shown in Fig. 6.4. In the overview STM image (Fig. 6.4a), we can still see some Bi clusters or oxide residuals, or even big defects (marked with green arrows and circles), nevertheless, the ordered honeycomb network is extending to a full monolayer. In the atomically resolved STM images of the honeycomb structure (6.4b), we clearly see the six-fold

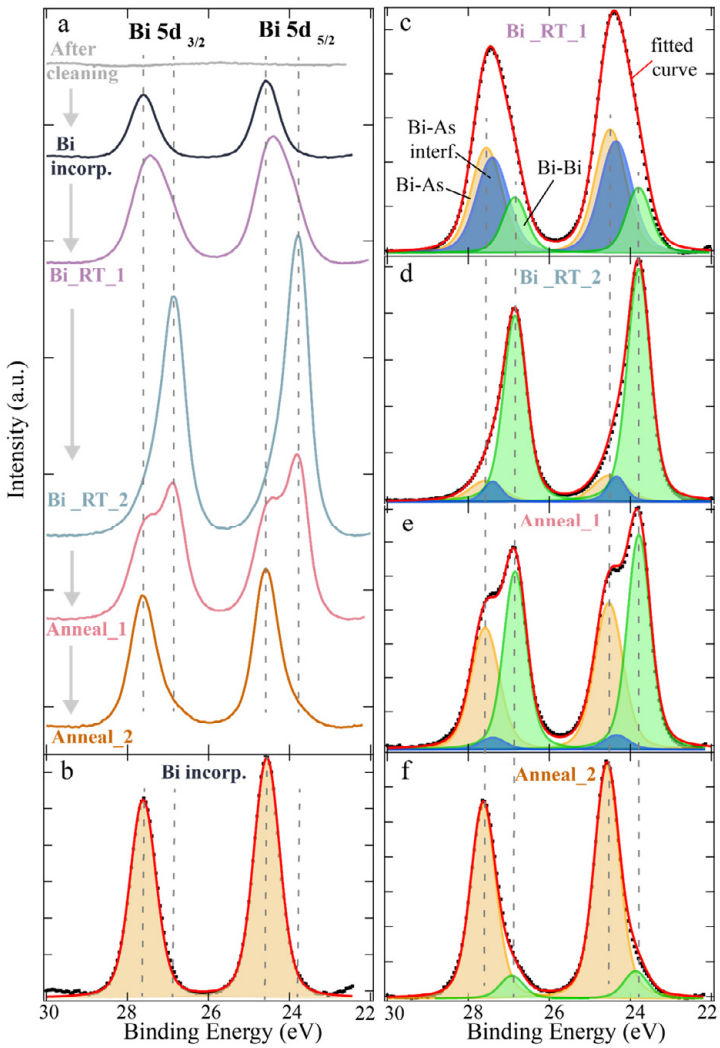

Figure 6.5 (a) Overview XPS spectra of Bi *5d* core level along the sample processing timeline. (b)-(f) Component decomposition and curve fitting of the spectra shown in (a). Photon energy is 120 eV for all spectra. Figure adapted from Paper **II**.

symmetry of the honeycomb structure which is also confirmed by fast Fourier transformation (FFT) patterns (Fig. 6.4c). The height profiles in Fig. 6.4d and 6.4e also demonstrate that it is a homogenous flat structure with a surface corrugation of less than 30 pm.

The chemical configurations of Bi atoms have been investigated by a comprehensive XPS study with a series of Bi deposition and surface treatments steps. Fig. 6.5 shows Bi *5d* spectra along the sample processing timeline. Among all steps, "Bi incorp." refers to the optimized Bi incorporation process for my experiments: Bi atoms are deposited onto clean GaAs(111)B at a temperature of 250°C, followed by 10 minutes annealing to 400°C. "Bi_RT_1/2" refers to Bi deposition on the sample surface at room temperature, with different amount. Finally, two subsequent thermal annealing steps at 250°C and 400°C are referred to as "Anneal_1" and "Anneal_2". We can see that for most XPS Bi *5d* spectra, photoelectrons from more than one component are involved. More specifically, Bi-As is the main and only component after Bi incorporation, it remains on the surface through all steps. In contrast, the Bi-Bi component only shows up after Bi deposition at room temperature and vanishes fast upon thermal annealing. This is valuable evidence in supporting our idea that the Bi-induced honeycomb structure consists of incorporated Bi atoms bonded with surface As atoms, instead of pure metallic Bi atoms.

Together with DFT calculations (performed by the group of Olle Eirksson at Uppsala University), an atomic model of the Bi-induced honeycomb structure on GaAs(111)B is established (Fig. 6.6), which presents the most energetically favored position for Bi incorporation. In this model, Bi atoms are located on top of the As

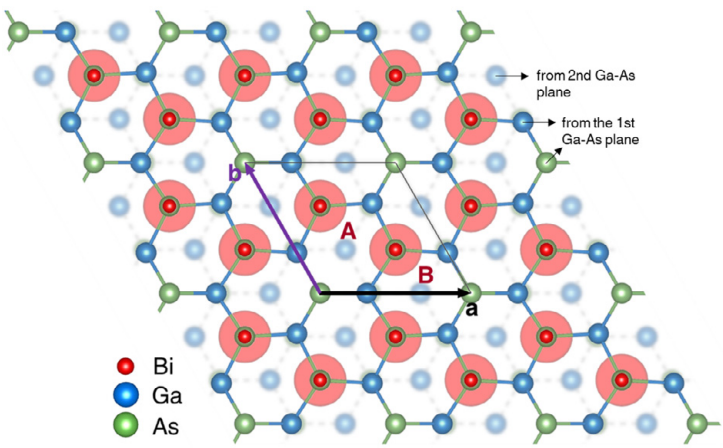

Figure 6.6 Atomic model of the honeycomb structure upon Bi deposition on GaAs(111)B. Figure adapted from Paper **II**.

sites, forming Bi-As bonds, and there is a vacancy of one Bi atom in the middle of a honeycomb structure. Since the model is in top view, we can see both top and second layer of Ga atoms.

The Bi-induced surface states have been shown in Fig. 4.4. More information on the study of Bi incorporation on GaAs(111)B can be found in Paper **II**.

6.3.3 Bi incorporation on surfaces of GaAs NWs

Bi incorporation has also been investigated on the side facets of crystal phase engineered III-V semiconductor NWs[61], after mechanical transfer of the NWs from the growth sample onto a suitable substrate[19]. Importantly, the various surface facets of both Zb and Wz crystal phase[21,22,43,61] of III-V semiconductor NWs offer an extra degree of freedom for surface-related growth phenomena. Furthermore, here they act as templates for site-selected overgrowth.

STM images which reveal the group-V atoms in the topmost surface layer after Bi incorporation are shown in Fig. 6.7. In both Zb {110}- and Wz{11$\bar{2}$0}-type surface

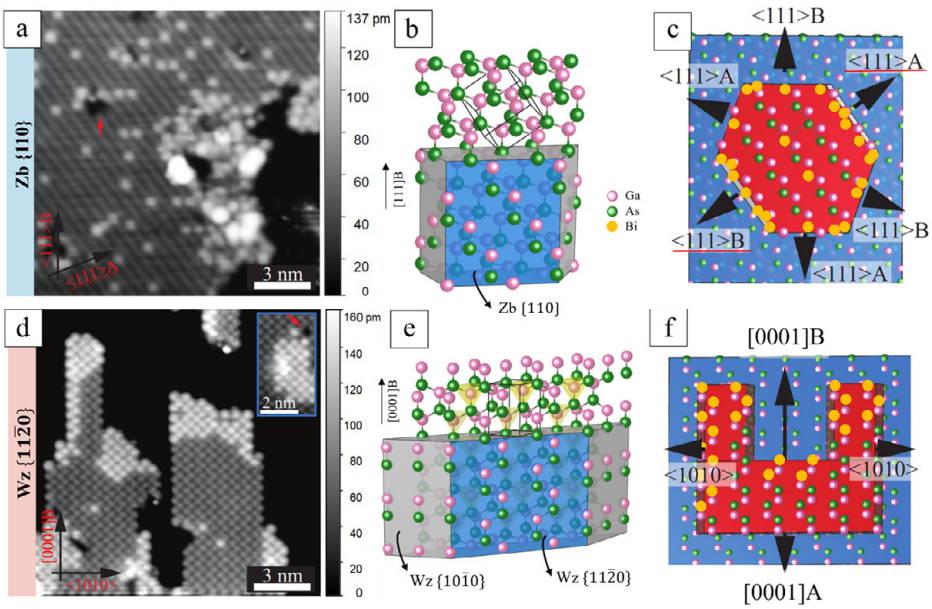

Figure 6.7 Bi incorporates into the surface layer of GaAs NWs. (a) and (d) show STM images of the Zb {110}-type surface and of the {11$\bar{2}$0}-type surface. (b) and (e) illustrate the GaAs 3D crystal structure for (b) Zb and (e) Wz phase. (c) and (f) show 2D models corresponding to the surfaces seen in (a) and (d). The red and blue areas represent the top terrace and the second atomic layer, respectively, of the NW surface, separated by surface steps. Figure adapted from paper **I**.

(Fig. 6.7a and b), Bi atoms are found to be incorporated into As sites by a Bi-for-As exchange reaction, forming a protrusion of about 40 - 50 pm. In this way, local Ga-Bi bonds are obtained.

However, the distribution of Bi atoms on Zb {110}- and {11$\bar{2}$0}-type surfaces is very different. On the Zb {110} facet, Bi atoms are randomly distributed, while small 1D chains or 2D islands of local GaBi structures consisting of a few tens of atoms are found on the Wz{11$\bar{2}$0} facet.

In the study of how Bi atoms incorporate into the GaAs surfaces, we found out that it appears to be favorable for the incorporated Bi atoms to be positioned next to each other in the nearest neighbor sites on the Wz {11$\bar{2}$0} facet, and there are a few crystal orientations along which Bi atoms tend to diffuse faster than along other orientations. For analysing the geometries and locations of these 1D chains and 2D islands of GaBi, it is illustrated that the self-selected diffusion paths and incorporation sites for Bi atoms are determined by the surface energy and the next nearest neighbor geometry. On the facets on GaAs NWs, a high density of step edges facing [0001]A/B directions is found essential to trigger the controlled Bi incorporation.

Thus, by carefully tailoring Wz/Zb heterostructure NWs, unique 2D and 1D nanostructures of pure GaBi, which are fully confined to one atomic layer, can be achieved, growing self-selectively on the NW {11$\bar{2}$0} facets. The crystal phase and surface step engineering of NW facets is inspiring for realization of well positioned nanostructures and QDs down to atomic scale.

For now, the mostly used method for yielding nanostructures in industry is by complex processing recipes using lithography and etching steps[80]. However, the lateral positioning is limited by the spatial resolution of the lithographic processes. Atom manipulation is another mean to achieve artificial nanostructures, where individual atoms are placed or re-positioned on a clean semiconductor surface using an STM probe tip. In this way, nanostructures with full control over the spatial position can be realized, e.g. single atom transistors based on P doping atoms in Si have been demonstrated[173,174], and QDs formed of chains of In atoms on an InAs surface have been studied[175]. While these approaches give fascinating insight into quantum processes, they are not suitable for large-scale industrial device processing, and demanding to implement even for scientific purposes. These two approaches are out of the scope of this thesis, thus, interested readers are suggested to read the mentioned references above.

Here, the self-selective formation of surface nanostructures offers an alternative approach down to the atomic level. More information on the study of Bi incorporation on GaAs NWs can be found in Paper **I.**

6.3.4 Bi incorporation on InAs

The approach of studying Bi incorporation in InAs surfaces is similar to that on GaAs. We investigated the incorporation mechanism of Bi adatoms into different types of InAs surfaces, such as bulk Zb InAs with a {110} surface and nanoplatelets with a Wz $\{11\bar{2}0\}$ facet. A dependency for the formation of As-Bi and In-Bi bonds on sample temperature and crystal facet was found. The bond formation on the Zb and Wz facets was similar for deposition at elevated temperatures, but showed distinct differences when the sample was left at room temperature. We found that the InAs Wz $\{11\bar{2}0\}$ surface supports the formation of a well-defined metal-semiconductor interface layer, in contrast to Zb (110) substrates.

Although I was strongly involved in the work, the study of Bi incorporation in InAs is not the main focus of this thesis. Thus, interested readers are welcome to find more details about this topic in Paper **III**.

7 Conclusion and outlook

The work presented in this dissertation is devoted to formation and modification of nanostructures to the atomic scale on III-V semiconductor surfaces. It focuses on the surface characterization of III-V surfaces upon Bi incorporation with the techniques of STM/S and XPS. The studies can be concluded in three categories: characterization of Bi surface incorporation, controlled formation of Bi-induced nanostructures, and their potential applications.

Characterization of Bi surface incorporation. Studies have been performed on various III-V nanowire and substrate surfaces, especially GaAs and InAs. Atomically resolved STM images, as shown in Paper **II**, demonstrate a Bi-induced 2D honeycomb structure on GaAs(111)B for the first time, illustrating a stable, well-ordered Bi-terminated semiconductor surface with Bi-induced states within the GaAs bandgap. This result is a successful example for Bi-induced low-dimensional structures with new electronic states in III-V semiconductor systems. Upon the more challenging task of STM imaging on Bi-incorporated NWs, discussed in Paper **I**, high resolution STM images have been successfully obtained on the unique facets on GaAs NW side walls, showing the first proof of Ga-Bi bonds with Bi in group-V lattice sites. The different nanostructures of GaBi on the various facets of NWs are also discovered by STM.

Paper **III** focuses on the chemical analysis of InAs:Bi surfaces under different process conditions. The XPS and STM study of temperature-controlled Bi incorporation on the Wz $\{11\bar{2}0\}$ surface of 2D InAs nanoplates shows that Bi substitutional integration happens on the surface followed by a Bi metal layer formation. Both As-Bi and In-Bi bond configurations have been observed by XPS, however, highly depending on the sample preparation process and material crystal phase. The results also show the versatility of the Bi incorporation approach of surface modification on several III-V surfaces and compounds.

Controlled formation of Bi-induced nanostructures. A new path has been explored in utilizing the unique facets of NW (and nanoplatelet) side walls as template for the synthesis of exotic materials in a site-selective incorporation fashion. By this approach, local 1D GaBi chains and 2D GaBi islands have been observed after Bi incorporation on Wz $\{11\bar{2}0\}$ facets of GaAs NWs (Paper **I**). Position-controlled

growth of few atoms small nanostructures has been realized. This leads to several interesting ideas: One can try to increase the GaBi coverage on wurtzite segments higher, even to a complete monolayer; The same approach can be investigated for Wz segments of various width (thus using the template for determining the width of 2D GaBi structures); Finally, radial overgrowth of the 2D GaBi structures on GaAs NWs is desired in order to embed the GaBi nanostructures.

In my studies, the mechanism of self-selective formation on Wz segments has been further investigated, and it proves that the terrace edges facing $[000\bar{1}]$ play an important role in triggering Bi incorporation. This study also illustrates a promising approach towards yielding exotic electronic phases of matter by utilizing the tunability of the tailored NW-based templates. This nanostructured growth template strategy can be applied to the formation of a range of monolayer thin nanostructures of exotic materials with variable width and atomically sharp borders at atomic-scale precision. The study in Paper **III** also illustrates that the 2D InAs platelets with their highly perfect morphology and particular crystal structure are well suited to control the interface with Bi for future use in quantum technology components.

The large-scale 2D Bi honeycomb structure on GaAs(111)B has a similar honeycomb structure as bismuthene, but with a larger lattice constant. More importantly, on the GaAs(111)B surface, every Bi atom has a covalent bond to an As atom underneath (in contrast to the bismuthene structure with a planar bonding geometry), but still, the observed honeycomb structure is a large-scale, fully 2D nanostructure/ heterostructure. Based on STS results and DFT simulations, the ordered Bi-induced 2D layer with a high Bi content of up to 67% surface coverage, covalently bonded to the GaAs substrate, is a great step towards realizing III-V semiconductor heterostructures with high Bi content that make use of the large spin-orbit coupling of Bi for enabling novel electronic properties.

Potential applications have been explored. For example, local alternation of the GaAs band gap has been observed through Bi surface incorporation, inducing a GaAs:Bi honeycomb structure (as shown in Paper **II**), and through a combination of strain and alloying with InAs in the case of laterally grown $In_xGa_{1-x}As$ NWs (see Paper **IV**). Since GaAs is well-known and used for semiconductor electronics, the Bi-induced bandgap decrease shows potential of being used in surface bandgap engineering. The changing Ga/In ratio in III-As NWs also gives an insight into how controlled band gap engineering can be realized in a single NW device. Moreover, the controlled, local formation of GaBi nanostructures, such as shown in Paper **I**, is highly promising for application in quantum information, making it an important step towards Bi-based III-V nanostructures with novel topologic and electronic properties.

In this fascinating field, more efforts should be put in several promising research directions. First, Bi deposition and alloying with different III-V compounds can be investigated with a similar approach. This can include Bi incorporation in III-Sb surfaces, since it should even be easier to integrate Bi with antimonides as compared to arsenides due to the larger size of Sb, which results in less lattice offset between antimonides and bismides as compared to GaAs/GaBi. Also, Sb has a relatively large spin-orbit splitting as well. Second, more tailored and sophisticated nanostructure templates can be made for site-selective Bi incorporation, aiming for higher Bi coverage, the desired GaBi nanostructures, or heterostructures with areas of different Bi incorporation. Third, overgrowth of GaBi or other Bi-containing surface structures would be a next challenge, on the way to creating III-V:Bi-based devices. Bi incorporated NW/nanostructure-based devices can be manufactured and electrically measured at low temperature in the combined STM/device measurement system for exploring further applications. Finally, non-trivial topological behavior on the surface of the III-V:Bi material can be studied in a more comprehensive way with complementary techniques, such as by simulations based on DFT, or by angle resolved photoemission spectroscopy (ARPES) to monitor the band structure of the Bi-induced surface.

References

1 www.youtube.com/watch?v=oSCX78-8-q0.

2 Wallentin, J. *et al.* High-performance single nanowire tunnel diodes. *Nano Lett* **10**, 974-979 (2010).

3 Doornbos, G. *et al.* High-performance InAs gate-all-around nanowire MOSFETs on 300 mm Si substrates. *IEEE Journal of the Electron Devices Society* **4**, 253-259 (2016).

4 Dey, A. W. *et al.* High-performance inas nanowire mosfets. *IEEE Electron Device Letters* **33**, 791-793 (2012).

5 Egard, M. *et al.* Vertical InAs nanowire wrap gate transistors with ft> 7 GHz and f max> 20 GHz. *Nano Lett* **10**, 809-812 (2010).

6 Larsen, T. W. *et al.* Semiconductor-nanowire-based superconducting qubit. *Physical review letters* **115**, 127001 (2015).

7 Thelander, C. *et al.* Nanowire-based one-dimensional electronics. *Materials today* **9**, 28-35 (2006).

8 Kim, S.-K. *et al.* Tuning light absorption in core/shell silicon nanowire photovoltaic devices through morphological design. *Nano Lett* **12**, 4971-4976 (2012).

9 Hochbaum, A. I. & Yang, P. Semiconductor nanowires for energy conversion. *Chemical reviews* **110**, 527-546 (2010).

10 Saxena, D. *et al.* Optically pumped room-temperature GaAs nanowire lasers. *Nature photonics* **7**, 963-968 (2013).

11 Yan, R., Gargas, D. & Yang, P. Nanowire photonics. *Nature photonics* **3**, 569-576 (2009).

12 Wallentin, J. *et al.* InP nanowire array solar cells achieving 13.8% efficiency by exceeding the ray optics limit. *Science* **339**, 1057-1060 (2013).

13 Borgström, M. T. *et al.* Nanowires with promise for photovoltaics. *Ieee Journal of selected topics in quantum electronics* **17**, 1050-1061 (2010).

14 Palacio-Morales, A. *et al.* Atomic-scale interface engineering of Majorana edge modes in a 2D magnet-superconductor hybrid system. *Science Advances* **5**, eaav6600, doi:10.1126/sciadv.aav6600 (2019).

15 Dick, K. A., Thelander, C., Samuelson, L. & Caroff, P. Crystal Phase Engineering in Single InAs Nanowires. *Nano Lett* **10**, 3494-3499, doi:Doi 10.1021/Nl101632a (2010).

16 Liu, Y. *et al.* Self-selective formation of ordered 1D and 2D GaBi structures on wurtzite GaAs nanowire surfaces. *Nat Commun* **12**, 1-7 (2021).

17 Jiang, N. *et al.* Enhanced minority carrier lifetimes in GaAs/AlGaAs core–shell nanowires through shell growth optimization. *Nano Lett* **13**, 5135-5140 (2013).

18 Heiss, M. *et al.* Self-assembled quantum dots in a nanowire system for quantum photonics. *Nat Mater* **12**, 439-444, doi:10.1038/nmat3557 (2013).
19 Hjort, M. *et al.* Direct Imaging of Atomic Scale Structure and Electronic Properties of GaAs Wurtzite and Zinc Blende Nanowire Surfaces. *Nano Lett* **13**, 4492-4498, doi:10.1021/nl402424x (2013).
20 Capiod, P. *et al.* Band offsets at zincblende-wurtzite GaAs nanowire sidewall surfaces. *Applied Physics Letters* **103**, 122104, doi:doi.org/10.1063/1.4821293 (2013).
21 Knutsson, J. *et al.* Atomic scale surface structure and morphology of InAs nanowire crystal superlattices: the effect of epitaxial overgrowth. *ACS applied materials & interfaces* **7**, 5748-5755 (2015).
22 Hjort, M. *et al.* Electronic and Structural Differences between Wurtzite and Zinc Blende InAs Nanowire Surfaces: Experiment and Theory. *ACS Nano* **8**, 12346-12355, doi:10.1021/nn504795v (2014).
23 Xu, T. *et al.* Faceting, composition and crystal phase evolution in III–V antimonide nanowire heterostructures revealed by combining microscopy techniques. *Nanotechnology* **23**, 095702, doi:doi:10.1088/0957-4484/23/9/095702 (2012).
24 Lee, J. S. *et al.* Selective-area chemical beam epitaxy of in-plane InAs one-dimensional channels grown on InP (001), InP (111) B, and InP (011) surfaces. *Physical Review Materials* **3**, 084606 (2019).
25 Friedl, M. *et al.* Template-assisted scalable nanowire networks. *Nano Lett* **18**, 2666-2671 (2018).
26 Vaitiekėnas, S. *et al.* Selective-area-grown semiconductor-superconductor hybrids: A basis for topological networks. *Physical review letters* **121**, 147701 (2018).
27 Rokhinson, L. P., Liu, X. & Furdyna, J. K. The fractional ac Josephson effect in a semiconductor–superconductor nanowire as a signature of Majorana particles. *Nature Physics* **8**, 795-799 (2012).
28 Mourik, V. *et al.* Signatures of Majorana fermions in hybrid superconductor-semiconductor nanowire devices. *Science* **336**, 1003-1007 (2012).
29 Gül, Ö. *et al.* Ballistic Majorana nanowire devices. *Nature nanotechnology* **13**, 192-197 (2018).
30 Liu, Y.-P. *et al.* Low temperature scanning tunneling microscopy and spectroscopy on laterally grown InxGa1− xAs nanowire devices. *Applied Physics Letters* **117**, 163101 (2020).
31 Persson, O. *et al.* Vol. 15 3684-3691 (2015).
32 Webb, J. L. *et al.* Imaging Atomic Scale Dynamics on III–V Nanowire Surfaces During Electrical Operation. *Scientific Reports* **7**, doi:10.1038/s41598-017-13007-w (2017).
33 Webb, J. L. *et al.* High resolution scanning gate microscopy measurements on InAs/GaSb nanowire Esaki diode devices. *Nano Research* **7**, 877-887 (2014).
34 Polak, M. P., Scharoch, P. & Kudrawiec, R. Vol. 30 (2015).
35 Ferhat, M. & Zaoui, A. Structural and electronic properties of III-V bismuth compounds. *Physical Review B* **73**, 115107 (2006).
36 Fluegel, B. *et al.* Giant spin-orbit bowing in GaAs1-xBix. *Phys Rev Lett* **97**, doi:10.1103/PhysRevLett.97.067205 (2006).
37 Balanta, M. A. G. *et al.* Vol. 49 (2016).

38 Wang, S. & Lu, P. *Bismuth-containing Alloys and Nanostructures*. Vol. 285 (Springer, 2019).
39 Huang, H., Liu, J. & Duan, W. Nontrivial Z2 topology in bismuth-based III-V compounds. *Physical Review B* **90**, 195105, doi:10.1103/physrevb.90.195105 (2014).
40 Chuang, F.-C. *et al.* Prediction of Large-Gap Two-Dimensional Topological Insulators Consisting of Bilayers of Group III Elements with Bi. *Nano Lett* **14**, 2505-2508, doi:10.1021/nl500206u (2014).
41 Tait, C. R., Yan, L. & Millunchick, J. M. Droplet induced compositional inhomogeneities in GaAsBi. *Applied Physics Letters* **111**, 042105, doi:10.1063/1.4996537 (2017).
42 Lewis, R. B. *et al.* Self-Assembly of InAs Nanostructures on the Sidewalls of GaAs Nanowires Directed by a Bi Surfactant. *Nano Lett* **17**, 4255-4260, doi:10.1021/acs.nanolett.7b01185 (2017).
43 Hjort, M. *et al.* Crystal Structure Induced Preferential Surface Alloying of Sb on Wurtzite/Zinc Blende GaAs Nanowires. *Nano Lett* **17**, 3634-3640, doi:10.1021/acs.nanolett.7b00806 (2017).
44 Momma, K. & Izumi, F. VESTA 3 for three-dimensional visualization of crystal, volumetric and morphology data. *Journal of Applied Crystallography* **44**, 1272-1276, doi:doi:10.1107/S0021889811038970 (2011).
45 Lehmann, S., Jacobsson, D., Deppert, K. & Dick, K. A. High crystal quality wurtzite-zinc blende heterostructures in metal-organic vapor phase epitaxy-grown GaAs nanowires. *Nano Research* **5**, 470-476, doi:10.1007/s12274-012-0232-3 (2012).
46 Caroff, K., Dick, J. J. & ME, M. K. Deppert, and L. Samuelson. *Nat. Nanotechnol* **4**, 50 (2009).
47 Cho, A. Y. & Hayashi, I. Surface structures and photoluminescence of molecular beam epitaxial films of GaAs. *Solid-State Electronics* **14**, 125-132, doi:10.1016/0038-1101(71)90087-6 (1971).
48 Ludeke, R. & Esaki, L. Electron energy-loss spectroscopy of GaAs and Ge surfaces. *Physical Review Letters* **33**, 653 (1974).
49 Ranke, W. & Jacobi, K. Composition, structure, surface states, and O2 sticking coefficient for differently prepared GaAs (lTTl) As surfaces. *Surface Science* **63**, 33-44 (1977).
50 Davies, J. H. *The physics of low-dimensional semiconductors: an introduction*. (Cambridge university press, 1998).
51 Treuting, R. & Arnold, S. Orientation habits of metal whiskers. *Acta Metallurgica* **5**, 598 (1957).
52 Mårtensson, T. *et al.* Epitaxial III− V nanowires on silicon. *Nano Lett* **4**, 1987-1990 (2004).
53 Tomioka, K., Yoshimura, M. & Fukui, T. A III–V nanowire channel on silicon for high-performance vertical transistors. *Nature* **488**, 189-192 (2012).
54 Mandl, B. *et al.* Growth mechanism of self-catalyzed group III− V nanowires. *Nano Lett* **10**, 4443-4449 (2010).
55 Hiruma, K., Murakoshi, H., Yazawa, M. & Katsuyama, T. Self-organized growth of GaAsInAs heterostructure nanocylinders by organometallic vapor phase epitaxy. *Journal of Crystal Growth* **163**, 226-231 (1996).

56 Johansson, J. & Dick, K. A. Recent advances in semiconductor nanowire heterostructures. *CrystEngComm* **13**, 7175-7184 (2011).
57 Lehmann, S., Wallentin, J., Jacobsson, D., Deppert, K. & Dick, K. A. A General Approach for Sharp Crystal Phase Switching in InAs, GaAs, InP, and GaP Nanowires Using Only Group V Flow. *Nano Lett* **13**, 4099-4105, doi:10.1021/nl401554w (2013).
58 Wagner, a. R. & Ellis, s. W. Vapor ‐ liquid ‐ solid mechanism of single crystal growth. *Applied physics letters* **4**, 89-90 (1964).
59 Magnusson, M. H., Deppert, K., Malm, J.-O., Bovin, J.-O. & Samuelson, L. Size-selected gold nanoparticles by aerosol technology. *Nanostructured Materials* **12**, 45-48, doi:10.1016/s0965-9773(99)00063-x (1999).
60 Maliakkal, C. B. *et al.* Independent Control of Nucleation and Layer Growth in Nanowires. *ACS Nano* **14**, 3868-3875, doi:10.1021/acsnano.9b09816 (2020).
61 Jacobsson, D. *et al.* Interface dynamics and crystal phase switching in GaAs nanowires. *Nature* **531**, 317-322, doi:10.1038/nature17148 (2016).
62 Harmand, J.-C. *et al.* Atomic step flow on a nanofacet. *Physical review letters* **121**, 166101 (2018).
63 Bolinsson, J., Caroff, P., Mandl, B. & Dick, K. A. Wurtzite–zincblende superlattices in InAs nanowires using a supply interruption method. *Nanotechnology* **22**, 265606 (2011).
64 Caroff, P., Bolinsson, J. & Johansson, J. Crystal phases in III--V nanowires: from random toward engineered polytypism. *IEEE journal of selected topics in quantum electronics* **17**, 829-846 (2010).
65 Dick, K. A. A review of nanowire growth promoted by alloys and non-alloying elements with emphasis on Au-assisted III–V nanowires. *Progress in Crystal Growth and Characterization of Materials* **54**, 138-173 (2008).
66 http://www.ioffe.ru/SVA/NSM/Semicond/GaAs/basic.html.
67 Regolin, I. *et al.* Growth and characterisation of GaAs/InGaAs/GaAs nanowhiskers on (1 1 1) GaAs. *Journal of crystal growth* **298**, 607-611 (2007).
68 Borgström, M. T. *et al.* In situ etching for total control over axial and radial nanowire growth. *Nano Research* **3**, 264-270 (2010).
69 Cutaia, D. *et al.* in *2016 IEEE Symposium on VlSI Technology.* 1-2 (IEEE).
70 Mauthe, S. *et al.* in *2019 International Conference on Optical MEMS and Nanophotonics (OMN).* 32-33 (IEEE).
71 Zota, C. B., Roll, G., Wernersson, L.-E. & Lind, E. Radio-frequency characterization of selectively regrown InGaAs lateral nanowire MOSFETs. *IEEE Transactions on Electron Devices* **61**, 4078-4083 (2014).
72 Aseev, P. *et al.* Ballistic InSb nanowires and networks via metal-sown selective area growth. *Nano Lett* **19**, 9102-9111 (2019).
73 Aseev, P. *et al.* Selectivity map for molecular beam epitaxy of advanced III–V quantum nanowire networks. *Nano Lett* **19**, 218-227 (2018).
74 Zota, C., Lindelöw, F., Wernersson, L.-E. & Lind, E. High-frequency InGaAs tri-gate MOSFETs with f max of 400 GHz. *Electronics Letters* **52**, 1869-1871 (2016).
75 Zota, C. B., Lindgren, D., Wernersson, L.-E. & Lind, E. Quantized Conduction and High Mobility in Selectively Grown In x Ga1–x As Nanowires. *ACS nano* **9**, 9892-9897 (2015).

76 Pan, D. *et al.* Dimension engineering of high-quality InAs nanostructures on a wafer scale. *Nano Lett* **19**, 1632-1642 (2019).
77 Bao, J. *et al.* Optical properties of rotationally twinned InP nanowire heterostructures. *Nano Lett* **8**, 836-841 (2008).
78 Miller, W. H. *A treatise on crystallography*. (Deighton, 1839).
79 Knutsson, J. V. *Atomic scale characterization of III-V nanowire surfaces*. (Division of Synchrotron Radiation Research, Department of Physics, Lund University, 2017).
80 del Alamo, J. A. Nanometre-scale electronics with III–V compound semiconductors. *Nature* **479**, 317-323, doi:10.1038/nature10677 (2011).
81 Binnig, G., Rohrer, H., Gerber, C. & Weibel, E. Surface Studies by Scanning Tunneling Microscopy. *Physical Review Letters* **49**, 57-61, doi:10.1103/PhysRevLett.49.57 (1982).
82 Wacker, A. *Fermi's golden rule* (Lund University, 2016).
83 Tersoff, J. & Hamann, D. R. Theory of the scanning tunneling microscope. *Physical Review B* **31**, 805 (1985).
84 Bardeen, J. Tunnelling from a many-particle point of view. *Physical review letters* **6**, 57 (1961).
85 Yngman, S. *Semiconductor Nanowires: Characterization and surface modification*, Lund University, (2019).
86 Troian, A. *Synchrotron X-ray based characterization of technologically relevant III-V surfaces and nanostructures* Doctoral thesis, Doctoral Thesis, Lund University, (2019).
87 Chen, C. (USA, 1993).
88 Li, K.-c., Li, G. & Wang, C. *Tungsten: its history, geology, ore-dressing, metallurgy, chemistry, analysis, applications, and economics*. (Reinhold publishing corporation, 1955).
89 Ottaviano, L., Lozzi, L. & Santucci, S. Scanning Auger microscopy study of W tips for scanning tunneling microscopy. *Review of Scientific Instruments* **74**, 3368-3378 (2003).
90 Ekvall, I., Wahlström, E., Claesson, D., Olin, H. & Olsson, E. Preparation and characterization of electrochemically etched W tips for STM. *Measurement Science and Technology* **10**, 11 (1999).
91 Schirmeisen, A. *Metallic Adhesion and Tunneling at the Atomic Scale* PhD thesis thesis, McGill University, Canada, (1999).
92 Kim, H. *et al.* Oxygen processed field emission tips for microcolumn applications. *Journal of Vacuum Science & Technology B: Microelectronics and Nanometer Structures Processing, Measurement, and Phenomena* **11**, 2327-2331 (1993).
93 Binh, V. T., Piquet, A., Roux, H., Uzan, R. & Drechsler, M. Sharpening of metal tips by heat treatment in vacuum. *Journal of Physics E: Scientific Instruments* **9**, 377 (1976).
94 Song, Y. J. *et al.* Invited review article: A 10 mK scanning probe microscopy facility. *Review of Scientific Instruments* **81**, 121101 (2010).
95 Meyer, E., Hug, H. J. & Bennewitz, R. *Scanning probe microscopy*. Vol. 4 (Springer, 2003).
96 Zangwill, A. *Physics at surfaces*. (Cambridge university press, 1988).

97 Crommie, M., Lutz, C. P. & Eigler, D. Imaging standing waves in a two-dimensional electron gas. *Nature* **363**, 524-527 (1993).
98 Kanisawa, K., Butcher, M., Tokura, Y., Yamaguchi, H. & Hirayama, Y. Local density of states in zero-dimensional semiconductor structures. *Physical Review Letters* **87**, 196804 (2001).
99 Hawkes, P. W. & Spence, J. C. *Science of microscopy*. Vol. 1 (Springer, 2007).
100 Feenstra, R. M., Stroscio, J. A., Tersoff, J. & Fein, A. P. Atom-selective imaging of the GaAs(110) surface. *Physical Review Letters* **58**, 1192-1195 (1987).
101 Feenstra, R. M. Scanning tunneling spectroscopy. *Surface science* **299**, 965-979 (1994).
102 Chen, C. J. Theory of scanning tunneling spectroscopy. *Journal of Vacuum Science & Technology A: Vacuum, Surfaces, and Films* **6**, 319-322 (1988).
103 Feenstra, R. M., Lee, J., Kang, M., Meyer, G. & Rieder, K. Band gap of the Ge (111) c (2× 8) surface by scanning tunneling spectroscopy. *Physical review B* **73**, 035310 (2006).
104 Bera, A., Dey, S. & Pal, A. J. Band mapping across a pn-junction in a nanorod by scanning tunneling microscopy. *Nano Lett* **14**, 2000-2005 (2014).
105 Yazdani, A., Jones, B., Lutz, C., Crommie, M. & Eigler, D. Probing the local effects of magnetic impurities on superconductivity. *Science* **275**, 1767-1770 (1997).
106 Koenraad, P. M. & Flatté, M. E. Single dopants in semiconductors. *Nature materials* **10**, 91-100 (2011).
107 Timm, R. *et al.* Confined states of individual type-II GaSb/GaAs quantum rings studied by cross-sectional scanning tunneling spectroscopy. *Nano Lett* **10**, 3972-3977 (2010).
108 Rahnejat, K. *et al.* Charge density waves in the graphene sheets of the superconductor CaC6. *Nat Commun* **2**, 1-6 (2011).
109 Stroscio, J. A., Feenstra, R. & Fein, A. Electronic structure of the Si (111) 2× 1 surface by scanning-tunneling microscopy. *Physical review letters* **57**, 2579 (1986).
110 Feenstra, R. M. Tunneling spectroscopy of the (110) surface of direct-gap III-V semiconductors. *Physical Review B* **50**, 4561-4570, doi:10.1103/PhysRevB.50.4561 (1994).
111 Mårtensson, P. & Feenstra, R. Voltage‐dependent imaging of antimony on the GaAs (110) surface. *Journal of Microscopy* **152**, 761-769 (1988).
112 Knutsson, J. V. *et al.* Vol. 11 10519-10528 (2017).
113 Feenstra, R. M., Gaan, S., Meyer, G. & Rieder, K. Low-temperature tunneling spectroscopy of Ge (111) c (2× 8) surfaces. *Physical Review B* **71**, 125316 (2005).
114 Mönch, W. in *Semiconductor Surfaces and Interfaces* 54-60 (Springer, 1995).
115 Hjort, M. *et al.* Surface chemistry, structure, and electronic properties from microns to the atomic scale of axially doped semiconductor nanowires. *ACS nano* **6**, 9679-9689 (2012).
116 Lin, L. & Robertson, J. Defect states at III-V semiconductor oxide interfaces. *Applied Physics Letters* **98**, 082903 (2011).
117 Feenstra, R. M., Dong, Y., Semtsiv, M. & Masselink, W. Influence of tip-induced band bending on tunnelling spectra of semiconductor surfaces. *Nanotechnology* **18**, 044015 (2006).

118 Webb, J. L. *et al.* Electrical and Surface Properties of InAs/InSb Nanowires Cleaned by Atomic Hydrogen. *Nano Lett* **15**, 4865-4875, doi:10.1021/acs.nanolett.5b00282 (2015).
119 Dombrowski, R., Steinebach, C., Wittneven, C., Morgenstern, M. & Wiesendanger, R. Tip-induced band bending by scanning tunneling spectroscopy of the states of the tip-induced quantum dot on InAs (110). *Physical Review B* **59**, 8043 (1999).
120 Morgenstern, M. *et al.* Low temperature scanning tunneling spectroscopy on InAs (110). *Journal of Electron Spectroscopy and Related Phenomena* **109**, 127-145 (2000).
121 Sun, M. *et al.* Photoluminescence properties of InAs nanowires grown on GaAs and Si substrates. *Nanotechnology* **21**, 335705 (2010).
122 Ma, D., Lee, C., Au, F., Tong, S. & Lee, S. Small-diameter silicon nanowire surfaces. *Science* **299**, 1874-1877 (2003).
123 Weitering, H. H. *et al.* Defect-mediated condensation of a charge density wave. *Science* **285**, 2107-2110 (1999).
124 Sacks, W., Roditchev, D. & Klein, J. Voltage-dependent STM image of a charge density wave. *Physical Review B* **57**, 13118 (1998).
125 Bode, M. *et al.* Magnetization-direction-dependent local electronic structure probed by scanning tunneling spectroscopy. *Physical review letters* **89**, 237205 (2002).
126 Pietzsch, O., Kubetzka, A., Bode, M. & Wiesendanger, R. Observation of magnetic hysteresis at the nanometer scale by spin-polarized scanning tunneling spectroscopy. *Science* **292**, 2053-2056 (2001).
127 Jourdan, M., Huth, M. & Adrian, H. Superconductivity mediated by spin fluctuations in the heavy-fermion compound UPd2 Al3. *Nature* **398**, 47-49 (1999).
128 Jäger, N., Ebert, P., Urban, K., Krause-Rehberg, R. & Weber, E. Scanning tunneling microscopy and spectroscopy of semi-insulating GaAs. *Physical Review B* **65**, 195318 (2002).
129 https://www.nobelprize.org/prizes/physics/1901/rontgen/facts/.
130 Einstein, A. Generation and conversion of light with regard to a heuristic point of view. *Annalen Der Physik* **17**, 132-148 (1905).
131 Chastain, J. & King Jr, R. C. Handbook of X-ray photoelectron spectroscopy. *Perkin-Elmer, USA*, 261 (1992).
132 Niemantsverdriet, J. W. *Spectroscopy in catalysis: an introduction*. (John Wiley & Sons, 2007).
133 Seah, M. P. & Dench, W. Quantitative electron spectroscopy of surfaces: A standard data base for electron inelastic mean free paths in solids. *Surface and interface analysis* **1**, 2-11 (1979).
134 Jablonski, A. & Powell, C. Effective attenuation lengths for quantitative determination of surface composition by Auger-electron spectroscopy and X-ray photoelectron spectroscopy. *Journal of electron spectroscopy and related phenomena* **218**, 1-12 (2017).
135 Lindau, I. & Spicer, W. The probing depth in photoemission and Auger-electron spectroscopy. *Journal of Electron Spectroscopy and Related Phenomena* **3**, 409-413 (1974).

136 Willmott, P. *An introduction to synchrotron radiation: techniques and applications*. (John Wiley & Sons, 2019).
137 Shin, S. New era of synchrotron radiation: fourth-generation storage ring. *AAPPS Bulletin* **31**, 21, doi:10.1007/s43673-021-00021-4 (2021).
138 Woodruff, D. P. *Modern techniques of surface science*. (Cambridge university press, 2016).
139 Balerna, A. & Mobilio, S. in *Synchrotron Radiation: Basics, Methods and Applications* (eds Settimio Mobilio, Federico Boscherini, & Carlo Meneghini) 3-28 (Springer Berlin Heidelberg, 2015).
140 Shayesteh, P. *Atomic Layer Deposition and Immobilised Molecular Catalysts Studied by In and Ex Situ Electron Spectroscopy*, Faculty of Science, Department of Physics, Lund University, (2019).
141 Acunto, G. D. Reaction Mechanisms and Dynamics in the Early Stage of High-κ Oxide Atomic Layer Deposition: Investigations by In Situ and Operando X-ray Photoemission Spectroscopy. (2022).
142 Mimura, H. *et al.* Breaking the 10 nm barrier in hard-X-ray focusing. *Nature physics* **6**, 122-125 (2010).
143 Döring, F. *et al.* Sub-5 nm hard x-ray point focusing by a combined Kirkpatrick-Baez mirror and multilayer zone plate. *Optics Express* **21**, 19311-19323 (2013).
144 Casalis, L. *et al.* ESCA microscopy beamline at ELETTRA. *Review of scientific instruments* **66**, 4870-4875 (1995).
145 Oigawa, H., Fan, J.-F., Nannichi, Y., Sugahara, H. & Oshima, M. Universal passivation effect of (NH4) 2Sx treatment on the surface of III-V compound semiconductors. *Japanese journal of applied physics* **30**, L322 (1991).
146 Bell, G., Kaijaks, N., Dixon, R. & McConville, C. F. Atomic hydrogen cleaning of polar III–V semiconductor surfaces. *Surface Science* **401**, 125-137 (1998).
147 Martinelli, V., Siller, L., Betti, M. G., Mariani, C. & Del Pennino, U. Surface modification of InAs (110) surface by low energy ion sputtering. *Surface science* **391**, 73-80 (1997).
148 Tuominen, M. *et al.* Oxidized crystalline (3× 1)-O surface phases of InAs and InSb studied by high-resolution photoelectron spectroscopy. *Applied Physics Letters* **106**, 011606 (2015).
149 Hjort, M. *III-V Nanowire Surfaces*. (Division of Synchrotron Radiation Research, Department of Physics, Lund …, 2013).
150 Chellappan, R. K., Li, Z. & Hughes, G. Synchrotron radiation photoemission study of the thermal annealing and atomic hydrogen cleaning of native oxide covered InAs (1 0 0) surfaces. *Applied surface science* **276**, 609-612 (2013).
151 Hofmann, P. Surface Physics. *An Introduction* (2013).
152 Takayanagi, K., Tanishiro, Y., Takahashi, S. & Takahashi, M. Structure analysis of Si (111)-7× 7 reconstructed surface by transmission electron diffraction. *Surface science* **164**, 367-392 (1985).
153 Binnig, G., Rohrer, H., Gerber, C. & Weibel, E. 7× 7 reconstruction on Si (111) resolved in real space. *Physical review letters* **50**, 120 (1983).
154 Narasimhan, S. & Vanderbilt, D. Elastic stress domains and the herringbone reconstruction on Au (111). *Physical review letters* **69**, 1564 (1992).
155 Haberern, K. & Pashley, M. GaAs (111) A-(2× 2) reconstruction studied by scanning tunneling microscopy. *Physical Review B* **41**, 3226 (1990).

156 Ohtake, A. *et al.* Surface structures of GaAs {111} A, B-(2x2). *Physical Review. B, Condensed Matter and Materials Physics* **64** (2001).
157 Pashley, M., Haberern, K., Friday, W., Woodall, J. & Kirchner, P. Structure of GaAs (001)(2× 4)− c (2× 8) determined by scanning tunneling microscopy. *Physical review letters* **60**, 2176 (1988).
158 Farrell, H. H., Lu, J., Schultz, B. D., Denison, A. B. & Palmstrøm, C. J. GaAs(111)B(√ 19 × √ 19)R23.4 ° surface reconstruction. **19**, 1597, doi:10.1116/1.1387460 (2001).
159 Koga, H. Structure of GaAs (-1-1-1) under Ga-rich conditions: A 19 × 19 reconstruction model. **82**, doi:10.1103/physrevb.82.113301 (2010).
160 Wang, L. *et al.* Novel Dilute Bismide, Epitaxy, Physical Properties and Device Application. *Crystals* **7**, 63, doi:10.3390/cryst7030063 (2017).
161 Ahola-Tuomi, M. *et al.* Formation of an ordered pattern of Bi nanolines on InAs(100) by self-assembly. *Applied Physics Letters* **92**, 011926, doi:10.1063/1.2831691 (2008).
162 Nicolaï, L. *et al.* Bi ultra-thin crystalline films on InAs(1 1 1)A and B substrates: a combined core-level and valence-band angle-resolved and dichroic photoemission study. *New Journal of Physics* **21**, 123012, doi:10.1088/1367-2630/ab5c14 (2019).
163 Nakamura, T. *et al.* Giant Rashba splitting of quasi-one-dimensional surface states on Bi/InAs(110)-$(2\ifmmode\times\else\texttimes\fi{}1)$. *Physical Review B* **98**, 075431, doi:10.1103/PhysRevB.98.075431 (2018).
164 Ludeke, R., Taleb‐Ibrahimi, A., Feenstra, R. M. & McLean, A. B. Structural and electronic properties of Bi/GaAs(110). *Journal of Vacuum Science & Technology B: Microelectronics Processing and Phenomena* **7**, 936-944, doi:10.1116/1.584584 (1989).
165 Bastiman, F., Cullis, A. G., David, J. P. R. & Sweeney, S. J. Bi incorporation in GaAs(100)-2×1 and 4×3 reconstructions investigated by RHEED and STM. *Journal of Crystal Growth* **341**, 19-23, doi:10.1016/j.jcrysgro.2011.12.058 (2012).
166 Honolka, J. *et al.* Electronic properties of GaAsBi (001) alloys at low Bi content. *Physical Review Materials* **3**, 044601 (2019).
167 Cornille, C., Arnoult, A., Gravelier, Q. & Fontaine, C. Links between bismuth incorporation and surface reconstruction during GaAsBi growth probed by in situ measurements. *Journal of Applied Physics* **126**, 093106 (2019).
168 McGinley, C. *et al.* Core-level photoemission study of the Bi-GaAs(111)A interface. *Applied Surface Science* **158**, 292-300, doi:10.1016/S0169-4332(00)00012-X (2000).
169 Laukkanen, P. *et al.* Bismuth-containing c(4×4) surface structure of the GaAs(100) studied by synchrotron-radiation photoelectron spectroscopy and ab initio calculations. *Journal of Electron Spectroscopy and Related Phenomena* **193**, 34-38, doi:10.1016/j.elspec.2014.02.008 (2014).
170 McGinley, C., Cafolla, A., Murphy, B., Teehan, D. & Moriarty, P. The interaction of bismuth with the GaAs (111) B surface. *Applied surface science* **152**, 169-176 (1999).
171 Punkkinen, M. P. J. *et al.* Thermodynamics of the pseudobinary GaAs1-xBix ($0 \leqslant x \leqslant 1$) alloys studied by different exchange-correlation functionals, special

quasi-random structures and Monte Carlo simulations. *Computational Condensed Matter* **5**, 7-13, doi:10.1016/j.cocom.2015.09.002 (2015).

172 Francoeur, S. *et al.* Band gap of GaAs1−xBix, 0<x<3.6%. *Appl Phys Lett,* **82**, 3874, doi:10.1063/1.1581983 (2003).

173 Fuechsle, M. *et al.* A single-atom transistor. *Nature Nanotechnology* **7**, 242-246, doi:10.1038/nnano.2012.21 (2012).

174 He, Y. *et al.* A two-qubit gate between phosphorus donor electrons in silicon. *Nature* **571**, 371-375, doi:10.1038/s41586-019-1381-2 (2019).

175 Fölsch, S., Martínez-Blanco, J., Yang, J., Kanisawa, K. & Erwin, S. C. Quantum dots with single-atom precision. *Nature Nanotechnology* **9**, 505-508, doi:10.1038/nnano.2014.129 (2014).